arXiv:2506.11552v2 [quant-ph] 10 Apr 2026

Learning Encodings by Maximizing State Distinguishability: Variational Quantum Error Correction

Nico Meyer[1,2,*], Christopher Mutschler[1], Andreas Maier[2] and Daniel D. Scherer[1]

[1]Fraunhofer IIS, Fraunhofer Institute for Integrated Circuits IIS, Nuremberg, Germany
[2]Pattern Recognition Lab, Friedrich-Alexander-University Erlangen-Nuremberg, Erlangen, Germany
[*]Author to whom any correspondence should be addressed.

E-mail: nico.meyer@iis.fraunhofer.de

Keywords: quantum computing, machine learning, quantum error correction, variational quantum algorithm

Abstract
Quantum error correction is crucial for protecting quantum information against decoherence. Traditional codes like the surface code require substantial overhead, making them impractical for near-term, early fault-tolerant devices. We propose a novel objective function for tailoring error correction codes to specific noise structures by maximizing the distinguishability between quantum states after a noise channel, ensuring efficient recovery operations. We formalize this concept with the distinguishability loss function, serving as a machine learning objective to discover resource-efficient encoding circuits optimized for given noise characteristics. We implement this methodology using variational techniques, termed variational quantum error correction (VarQEC). Our approach yields codes with desirable theoretical and practical properties and outperforms standard codes in various scenarios. We also provide proof-of-concept demonstrations on IBM and IQM hardware devices, highlighting the practical relevance of our procedure.

1 Introduction

Quantum computing promises to solve complex problems intractable for classical computers, such as cryptographic analysis [94], simulation [29, 37], optimization [1], and machine learning [12, 72]. However, maintaining quantum state coherence amidst noise [104] is a significant challenge. Quantum error correction (QEC) is essential to protect quantum information from errors due to environmental interactions and imperfect quantum operations [92, 97].

Traditional QEC codes aim to detect and correct arbitrary quantum errors up to a certain weight, like e.g. the surface code [35]. Recent experiments demonstrate that noise suppression increases exponentially with code size [3], confirming theoretical predictions [93]. However, these codes require substantial overhead in additional qubits and complex recovery operations, posing a barrier for near-term devices and the upcoming early fault-tolerant quantum computing (eFTQC) era [53], where resources are limited and error rates are high.

Thus, reducing resource requirements is crucial, e.g., by tailoring codes to specific noise structures of hardware platforms [5, 102]. Alternatively, one can relax perfect correction conditions and use approximate QEC codes with less overhead [59, 90]. Recent advancements explore integrating artificial intelligence (AI) techniques into quantum computing and QEC [4]. While much literature focuses on machine learning (ML)-based decoders for error correction [8, 101], there is growing interest in leveraging AI to design better quantum codes and encoding strategies [34, 77].

Main Contributions of this Work. We claim and summarize the main contributions of our paper as follows:

I. We introduce the novel *distinguishability loss* function for learning approximate QEC codes. This loss aims to maximize the trace distance between pairs of quantum states after passing through a noise channel, ensuring effective recovery. We define worst-case and average-case variants and present a fast approximation using a two-design ensemble for efficient computation and optimization.

II. We derive theoretical properties of the distinguishability loss, specifically proving its relationship to the fidelity after recovery. This demonstrates that minimizing the distinguishability loss leads to improved error correction performance. Furthermore, we connect our method to established metrics in QEC like the code distance.

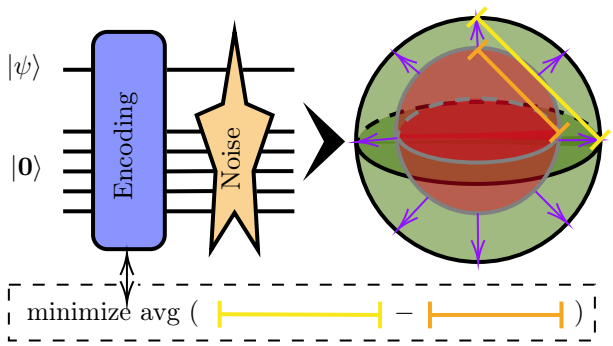

Figure 1. We propose a procedure that tailors quantum error correction encodings to arbitrary noise channels. In our setup, a pure state $|\psi\rangle$ is encoded into a larger ancilla system, and a noise channel then acts on the involved wires. We illustrate this with pairs of states $|\psi_0\rangle = |0\rangle$ and $|\psi_1\rangle = |+\rangle$, which in the noise-free case can be visualized on the top and right side of a unit sphere–the Bloch sphere in the single-qubit setup. Under noise, e.g., a combination of depolarizing and amplitude damping processes, the sphere shrinks and the states are drawn inwards. We quantify this by computing the trace distance between the original states (yellow line) and subtracting the trace distance between their noisy counterparts (orange line). To optimize the encoding for arbitrary states, we minimize the average distinguishability loss over pairs of states drawn from a two-design, thereby encouraging minimal sphere shrinkage (shown by blue arrows) and enabling high-fidelity recovery. For proof of principle, we implement this procedure as a variational quantum algorithm using a parameterized encoding ansatz, calling it variational quantum error correction (VarQEC).

III. We incorporate our approach into a variational quantum algorithm, termed variational quantum error correction. This also integrates elements from the QVECTOR approach [50] for learning recovery operations. We provide an end-to-end implementation to encourage reproducibility and future extensions.

IV. We conduct extensive empirical evaluations to demonstrate the efficiency and effectiveness of the variational quantum error correction (VarQEC) procedure across various noise models and system sizes. Our evaluations analyze the stability and noise resilience of the resulting codes. We show that our method outperforms traditional QEC codes in various scenarios, particularly under asymmetric noise conditions.

V. We deploy the learned encoding operations on actual IBM and IQM quantum hardware. These experiments demonstrate consistent improvements over purely physical realizations and provide empirical evidence of the practical applicability of VarQEC codes, highlighting their promising noise suppression capabilities as system size increases.

In summary, our work advances the field of quantum error correction by introducing a novel, adaptable approach for learning error-correcting codes tailored to specific noise channels. Leveraging the distinguishability loss within a variational framework, we reduce the overhead associated with traditional QEC codes. Our method is particularly well-suited for the era of eFTQC [53], where resource efficiency and adaptability to hardware constraints are critical.

The remainder of this paper is organized as follows: In section 2, we position our work within the literature on AI-enhanced QEC. Section 3 summarizes the background on noise channels, distance measures for quantum states, and QEC. In section 4, we formally introduce the distinguishability loss, formulate the VarQEC algorithm, and derive theoretical properties of the learned codes. The empirical results in section 5 demonstrate the effectiveness of the VarQEC codes compared to standard QEC codes. In section 6, we deploy code instances on IBM and IQM hardware systems to underline the practical relevance of our procedure. We identify current limitations of the VarQEC procedure and outline future improvements and extensions in section 7. Finally, in section 8, we provide an overview and discuss our results in the context of QEC and eFTQC.

2 Related Work

AI is drawing increasing interest in the domain of quantum computing in general [4], and QEC in particular [109]. Much of the existing literature is, however, focused on developing ML-based decoders [9, 101]. In the following, we briefly summarize the existing literature on AI for QEC beyond decoders, and highlight the connection to and delimitation from our work.

Classical Machine Learning for QEC. The integration of AI into QEC began around 2018 with the pioneering work of Fösel et al. [34], which employed reinforcement learning (RL). In this

approach, a reward function was constructed from several components, including the *recoverable quantum information*, *protection reward*, and *recovery reward*. This methodology was used to train encoding and recovery circuits on systems with up to four physical qubits and one logical qubit, primarily focusing on bit-flip noise. This notion of recoverable quantum information is related to our proposed distinguishability loss, both being based on the trace distance. However, we argue in section 4.1 that only the latter constitutes a loss function that is efficient to evaluate for complex noise structures. Furthermore, while the recoverable quantum information was restricted to stabilizer codes, our formulation extends to non-additive codes.

A modified RL routine for QEC has recently been proposed, formulating reward functions based on the Knill-Laflamme conditions [77, 78]. Aspects of fault tolerance have also been incorporated by learning flag gadgets [114]. RL has further been studied for modifying and combining existing codes [66, 75, 98, 112], autonomous QEC [80, 113, 116], and the discovery of gadgets for low-density parity-check (qLDPC) codes [33, 44]. Additionally, RL has been applied to the discovery of logical gates within specific experimental setups [48]. Other QEC scenarios have also been considered through the lens of techniques from supervised and unsupervised learning techniques [8, 64, 107, 115], evolutionary approaches [99, 110], as well as various other ML approaches [26, 41, 91].

Variational Techniques for QEC. Variational methods have gained attention in the context of QEC due to their flexibility and adaptability to quantum hardware. The first proposal to formulate QEC as a variational algorithm was proposed in 2017 by Johnson et al. [50], dubbed QVECTOR. In this approach, the fidelity after recovery is used as a loss function to simultaneously train the free parameters of encoding and recovery circuits. The authors demonstrate the effectiveness of the approach in low-probability amplitude and phase damping noise scenarios, using systems with up to five physical qubits and a single logical qubit. However, we observed that the concept of simultaneously learning encoding and recovery is limited to rather small code instances and simple low-probability noise structures, due to training not converging in more complex scenarios. A modification to the QVECTOR approach proposes to enhance trainability by employing a Wasserstein version of the fidelity [118]. However, in our evaluations, this improvement did not manifest. In contrast to QVECTOR, our proposed technique modularizes the training of the encoding and recovery operations, allowing for more flexibility and the consideration of complex noise structures.

Other works have investigated the use of convolutional quantum neural networks [27] and quantum autoencoders for QEC [61, 65, 86]. In some instances, these methods function more as denoising algorithms than as active QEC strategies. Different techniques aim to generate codes by formulating the task of QEC as finding the ground state of a Hamiltonian [19, 108, 111]. However, these approaches assume full direct access to the error operators and stabilizers. Additionally, preliminary work has been conducted on finding logical operations for given codes via variational techniques [24].

3 Background

As mentioned before, quantum systems are highly susceptible to errors due to decoherence and interactions with the environment [104]. To build reliable quantum computers, it is crucial to understand how quantum information is affected by noise and how to correct for the introduced errors. In this section, we introduce the underlying concepts on noise channels, distance measures for quantum states, and error correction that go into the VarQEC procedure we introduce in this paper. Supplementary details can be found in appendix A.

3.1 Quantum Noise Channels

Quantum noise channels are mathematical models that describe how quantum states evolve in the presence of noise and decoherence. A pure n-qubit quantum state is typically described using Dirac notation as $|\psi\rangle \in \mathcal{H}^{\otimes n}$, where $\mathcal{H}$ denotes the Hilbert space, and it holds $\langle\psi|\psi\rangle = 1$. Using the density matrix formalism, one can express the same state as $\rho = |\psi\rangle\langle\psi|$, which is of rank one for pure states. More general *mixed states* represent a statistical ensemble of pure states and can be described by a density matrix

$$\rho = \sum_i p_i |\psi_i\rangle\langle\psi_i| , \tag{1}$$

where $p \geq 0$ and $\sum_i p_i = 1$. In the case of mixed states, the rank of ρ is greater than one.

Quantum operations can either be of unitary or non-unitary nature. A unitary transformation U acts on a state as $U\rho U^\dagger$, preserving purity and ensuring reversibility of the operation. However, real-world quantum systems are open and therefore interact with the environment, leading to non-unitary processes that introduce noise and decoherence. These processes are described by completely positive trace preserving (CPTP) maps, which can be represented in the *operator sum* representation as

$$\mathcal{N}(\rho) = \sum_k E_k \rho E_k^\dagger, \tag{2}$$

where the E_k are Kraus operators satisfying $\sum_k E_k^\dagger E_k = I$, which ensures trace preservation. This description is also often referred to as *Kraus representation* [56].

A common example of a quantum noise channel is the *depolarizing channel*, which models a state deteriorating to a fully mixed state with a certain probability. Single-qubit depolarizing noise can be described as

$$\mathcal{N}(\rho) = (1-p)\rho + \frac{p}{3}X\rho X^\dagger + \frac{p}{3}Y\rho Y^\dagger + \frac{p}{3}Z\rho Z^\dagger, \tag{3}$$

where p is the depolarization probability and X, Y, and Z are the Pauli operators representing bit-flip, bit-flip and phase-flip, and phase-flip errors, respectively [76]. General single-qubit Pauli noise can be described as

$$\mathcal{N}(\rho) = (1-p)\rho + p_X X\rho X^\dagger + p_Y Y\rho Y^\dagger + p_Z Z\rho Z^\dagger, \tag{4}$$

with overall nosie strength $p = p_X + p_Y + p_Z$. Arbitrary quantum errors in multi-qubit systems can be expanded as linear combinations of tensor products of Pauli operators. Consequently, correcting bit-flip and phase-flip errors on each qubit inherently addresses more general multi-qubit error scenarios [38]. In the context of stabilizer-based QEC, this can be understood as syndrome measurements effectively projecting general errors into Pauli errors [55].

In many practical scenarios, and most of this paper, errors are assumed to act independently on each qubit, leading to a composite noise model

$$\mathcal{N}^{\otimes n} = \bigotimes_{j=1}^{n} \mathcal{N}_j, \tag{5}$$

where $\mathcal{N}_j$ is a noise channel on qubit j. Considerations and experiments on correlated noise are conducted in section 5.2.

3.2 Distance Measures for Quantum States

Quantifying the difference between quantum states is essential for the task of quantum error correction. Measures of state similarity or distinguishability help in evaluating the performance of quantum algorithms and error correction codes [76].

The fundamental metric we employ in this paper is the *trace distance*, which for two quantum states ρ and σ is defined as

$$T(\rho, \sigma) = \frac{1}{2}\|\rho - \sigma\|_1, \tag{6}$$

where $\|A\|_1 = \mathrm{Tr}\sqrt{A^t A}$ denotes the trace norm of the operator A [36]. The trace distance quantifies the distinguishability between quantum states and is bounded between 0 and 1, with 0 indicating identical states and 1 representing completely distinguishable (orthogonal) states. These bounds and operational meaning, as well as the fact that it defines a full metric, contribute to the definition of a stable loss function in section 4. The trace distance is invariant under unitary transformations, i.e.,

$$T(U\rho U^\dagger, U\sigma U^\dagger) = T(\rho, \sigma). \tag{7}$$

It furthermore satisfies the data processing inequality [103], meaning it cannot increase under CPTP maps such as noise channels:

$$T(\mathcal{N}(\rho), \mathcal{N}(\sigma)) \leq T(\rho, \sigma). \tag{8}$$

These properties make the trace distance a reliable measure when evaluating the effect of quantum operations on state distinguishability.

In this paper, we formulate the goal of a QEC code to encode information in such a way that the trace distance between different encoded states remains large, facilitating better correction operations. This approach is inspired by the *quantum relative entropy* [106], which measures the informational divergence between two states. Its theoretical connection to the *recovery map* [82] provides guarantees on the existence of successful recovery operations. However, the quantum relative entropy is not a real metric, violating symmetry and the triangle inequality. Furthermore, it is unbounded and challenging to compute, making it less practical for defining a loss function.

Another important measure is the *fidelity* [51] between quantum states ρ and σ, defined as:

$$F(\rho, \sigma) = \left(\mathrm{Tr}(\sqrt{\sqrt{\rho}\sigma\sqrt{\rho}}) \right)^2 \tag{9}$$

It quantifies the overlap between the states, with values ranging from 0 (orthogonal states) to 1 (identical states). The fidelity is invariant under unitary transformations and non-decreasing under CPTP maps; however, it is not a full metric because it violates the triangle inequality [76]. While a metric property is not strictly required for training a loss function with gradient descent, it significantly enhances both stability and interpretability [60], which is why we focus on the trace distance in our work.

3.3 Quantum Error Correction

Quantum error correction is a framework designed to protect quantum information from errors due to decoherence and imperfect quantum operations [92, 97]. By encoding quantum information into entangled states of multiple qubits, QEC allows for the detection and correction of certain types of errors without measuring and thereby collapsing the quantum information itself.

The first and crucial step of such an error correction procedure is to find an encoding operation U_{enc} that maps the k-qubit pure state into a larger composite n-qubit system, creating redundancy that can protect against errors [16]. The encoding operation produces the *encoded* state using the original state ρ and ancilla qubits initialized to $|0\rangle$:

$$\rho_L = U_{\mathrm{enc}} \left(\rho \otimes |0\rangle \langle 0|^{\otimes n-k} \right) U_{\mathrm{enc}}^\dagger \tag{10}$$

The After the state passes through some noise channel $\mathcal{N}$, the resulting state is mixed and can be described as

$$\tilde{\rho}_L = \mathcal{N}(\rho_L). \tag{11}$$

Afterwards, a recovery operation U_{rec} has to be applied to obtain the corrected state, potentially using and successively discarding an additional recovery register [38]:

$$\hat{\rho}_L = \mathrm{Tr}_r \left(U_{\mathrm{rec}} \left(\tilde{\rho}_L \otimes |0\rangle \langle 0|^{\otimes r} \right) U_{\mathrm{rec}}^\dagger \right) \tag{12}$$

Hereby, r is the number of recovery qubits, and Tr_r denotes the partial trace over all these qubits. Traditional QEC involves syndrome extraction through measurements, followed by conditional recovery operations based on the measurement outcomes [97]. However, in our approach, we combine syndrome extraction and recovery into a single coherent operation without intermediate measurements, performing what is known as coherent or measurement-free error correction [45, 76]. Once the protection should be lifted, e.g. when the state has been transmitted and should be measured, the decoding operation can be applied as

$$\hat{\rho} = \mathrm{Tr}_{n-k} \left(U_{\mathrm{enc}}^\dagger \hat{\rho}_L U_{\mathrm{enc}} \right), \tag{13}$$

where Tr_{n-k} traces out the encoding ancilla qubits.

The overall error correction procedure $\mathcal{R}$ aims to satisfy $(\mathcal{R} \circ \mathcal{N})(\rho) \propto \rho$ for all ρ whose support is in the code space $\mathcal{C}$. Alternative formulations, such as the Knill-Laflamme conditions, provide criteria for when a set of errors can be perfectly corrected by a QEC code [55]. However, our proposed routine works mostly within the framework of approximate error correction. A more intuitive formulation states the goal as getting the fidelity between the recovered state $\hat{\rho}$ and the original state ρ as close as possible to 1, i.e. quantified by the fidelity as

$$F(\rho, \hat{\rho}) \geq 1 - \delta, \tag{14}$$

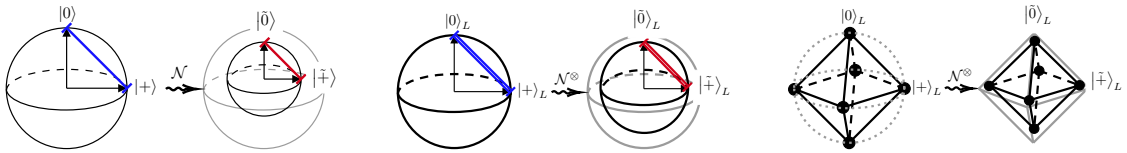

(a) Effect of a noise channel on a single physical qubit visualized on the Bloch sphere. The shrinking of the sphere and the shift of the center towards the $|0\rangle$-state can, e.g. be caused by depolarizing combined plus amplitude damping noise [42]. The blue line marks the distance of optimal $|0\rangle$ and $|+\rangle$ states, the red one marks the distance after the noise channel. For the single-qubit setup, one can equivalently use the trace or the Euclidean distance, yielding $T(|0\rangle, |+\rangle) = \frac{1}{\sqrt{2}}$.

(b) Effect of a composite noise channel on an encoded multi-qubit system. While these are not Bloch spheres, for the purpose of visualizing the trace distance, the undistorted sphere still has unit length. This follows from the invariance of the trace distance under unitary operations, consequently $T(|0\rangle_L, |1\rangle_L) = \frac{1}{\sqrt{2}}$.

(c) Effect of a composite noise channel on an encoded multi-qubit system. Instead of considering the entire sphere, we restrict ourselves to the effects on a spherical two-design. More concretely, we form a two-design of the underlying physical single-qubit state with $\mathcal{S} = \{|0\rangle, |1\rangle, |+\rangle, |-\rangle, |+i\rangle, |-i\rangle\}$.

Figure 2. Effect of noise on a physical state (a) and an encoded logical state (b). Under the assumption of a sophisticated encoding operation, we can satisfy $T(|\tilde{0}\rangle, |\tilde{1}\rangle) < T(|\tilde{0}\rangle_L, |\tilde{1}\rangle_L)$. This allows us to reduce the lost trace distance $\Delta_T(|0\rangle, |1\rangle)$. In practice, we have to minimize this measure over all possible state pairs, or alternatively over all combinations of the spherical two-design in (c).

with δ being a small positive error threshold [10]. In the experimental section, we discuss that some instances of the learned code reduce δ to practically 0, allowing for exact correction.

An arbitrary QEC code can be characterized by its code parameters

$$((n, K = 2^k, d)), \tag{15}$$

where n is the number of physical qubits to encode k logical qubits (general *non-additive* codes do not restrict $k = \log_2 K$ to a whole number, but in this work we do not consider such codes). Furthermore, d is the *code distance* [15], which gives the minimum number of qubits that need to be affected by an error operation to transform one valid codeword into another one. In other words, it is the minimum number of non-trivial single-qubit Pauli errors that break the code. A distance-d QEC code can detect up to $d-1$ errors and correct up to $\lfloor \frac{d-1}{2} \rfloor$. Therefore, a larger code distance implies a higher capability to correct errors. However, in general, a larger code distance requires a larger number of physical qubits, which is also quantified by the *code rate* $\frac{k}{n}$. When talking about codes with no provable or unknown distance, as for most VarQEC instances, we simplify the notation to

$$((n, K)). \tag{16}$$

The special case of *additive* QEC codes, usually also called *stabilizer* codes, is indicated by the modified notation

$$[[n, k, d]]. \tag{17}$$

In typical QEC procedures, multiple recovery cycles are necessary because new errors can arise again after the previous recovery step. As our work is mostly concerned with the encoding operation, and not so much the recovery, we focus on only a single recovery step in the following. By tailoring the encoding operations to specific noise channels, we aim to enhance the effectiveness of the codes and reduce complexity.

4 Learning Error Correction Codes

In this section, we introduce our method for learning QEC codes by maximizing state distinguishability. We define a loss function based on the trace distance between quantum states, realize the method as a variational quantum algorithm, discuss how to perform error correction using recovery operations, and analyze the properties of the learned codes. Supplementary details can be found in appendices B and C.

4.1 Lost Trace and Distinguishability Loss

To begin with, we define the *lost trace distance* between two pure quantum states ρ and σ under a noise channel $\mathcal{N}$ as

$$\Delta_T(\rho, \sigma; \mathcal{N}; \Theta) = T(\rho, \sigma) - T(\mathcal{N}(\rho_L), \mathcal{N}(\sigma_L)), \tag{18}$$

where ρ_L and σ_L are prepared using the potentially parameterized encoding operation $U_{\text{enc}}(\Theta)$ as described in equation (10). Due to the trace distance's invariance under both tensoring with pure states and unitary transformations, we can also express the first term as $T(\rho_L, \sigma_L)$, but the former is usually more straightforward to compute. This measure is also indicated in figure 1 and its components are explicitly marked in figure 2.

The motivation behind this definition is to find an encoding operation that minimizes the loss of distinguishability between quantum states after a noise channel. By keeping the lost trace distance as small as possible, we ensure that sufficient information is preserved for the subsequent recovery operation. Based on this, we define the *distinguishability loss*. Since we do not know in advance which states we need to encode, the encoding operation should work effectively for arbitrary pure states. We are usually concerned with the worst-case scenario, defining the *worst-case distinguishability loss* as

$$\overline{\mathcal{D}}(\mathcal{N}; \Theta) = \max_{\rho,\sigma} \Delta_T(\rho, \sigma; \mathcal{N}; \Theta). \tag{19}$$

For practical optimization, evaluating the worst-case loss is challenging because it involves a maximization over an infinite set of state pairs. In principle, it is possible to use techniques from semi-definite programming [95], but it is hard to obtain guarantees for the efficiency of finding the solution. Moreover, we empirically found that the worst-case formulation also has the drawback that employing it as a loss function leads to severe instabilities in the training procedure, which aligns with findings from classical machine learning [7, 43]. To address this, we define the *average-case distinguishability loss as*

$$\mathcal{D}(\mathcal{N}; \Theta) = \int_\rho \int_\sigma \Delta_T(\rho, \sigma; \mathcal{N}; \Theta)\, d\nu(\rho)\, d\nu(\sigma), \tag{20}$$

where $d\nu$ denotes the integration over the Haar measure of pure quantum states [96]. However, computing this integral is again impractical due to the continuous nature of the state space. Therefore, we use a two-design approximation [6] on the Hilbert space $\mathcal{H}^{\otimes k}$, where k is the number of data qubits. This approximation uses a finite set $\mathcal{S}$ of states that for a two-design [30], allowing to approximate the average-case loss as

$$\mathcal{D}_{\mathcal{S}}(\mathcal{N}; \Theta) = \frac{1}{|\mathcal{S}|^2} \sum_{\rho \in \mathcal{S}} \sum_{\sigma \in \mathcal{S}} \Delta_T(\rho, \sigma; \mathcal{N}; \Theta). \tag{21}$$

For example, for a single data qubit we can choose $\mathcal{S} = \{|0\rangle, |1\rangle, |+\rangle, |-\rangle, |+i\rangle, |-i\rangle\}$, which reduces the number of evaluations to $\frac{|\mathcal{S}|^2 - |\mathcal{S}|}{2}$, accounting for the symmetry $\Delta_T(\rho, \sigma; \mathcal{N}) = \Delta_T(\sigma, \rho; \mathcal{N})$ and $\Delta_T(\rho, \rho; \mathcal{N}) = 0$. While this approximation is not exact due to up to fourth-order moments in the loss function, it holds that $\mathcal{D}_{\mathcal{S}}(\mathcal{N}) \approx \mathcal{D}(\mathcal{N})$, which is sufficient for using the measure as a loss function. The concept of quantum t-designs is more formally introduced and analyzed regarding approximation quality in appendix B.4. In short, the two-design approximation introduces a noise-dependent bias with low variance, effectively just shifting the loss function.

Conceptually, our distinguishability loss is related to the *recoverable quantum information* introduced in Ref. [34], as both are built from the trace distance. The recoverable quantum information is defined as $\mathcal{R}_Q(t) = \frac{1}{2} \min_{\vec{n}} \|\hat{\rho}_{\vec{n}}(t) - \hat{\rho}_{-\vec{n}}(t)\|_1$, where $\hat{\rho}_{\vec{n}}$ describes the evolution under initial pure state $\vec{n}$, and $\hat{\rho}_{-\vec{n}}$ under the initially orthogonal state, respectively. For the special case of a single logical qubit under isotropic unital noise, which guarantees that the worst-case violation is caused by antipodal pairs, both measures coincide, concretely $\overline{\mathcal{D}}$ is proportional to $1 - R_Q$. However, the distinguishability loss constitutes a more general and practically different object: It naturally extends to multiple logical qubits per patch, and as shown in section 4.4 $\overline{\mathcal{D}}$ establishes analytic bounds on the fidelity after recovery, one of the standard figures of merit in QEC. Furthermore, while $\mathcal{R}_Q$ is defined as a discrete reward function only, the average-case proxy of the distinguishability loss $\mathcal{D}$ is smooth and differentiable in the encoding parameters, and can therefore be optimized directly with gradient-based techniques. Importantly, the recoverable quantum

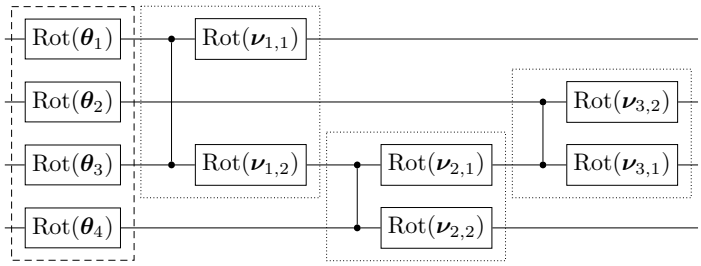

Figure 3. An instance of the REA on 4 qubits. It consists of an initial block of parameterized single-qubit rotations 3 blocks of successive entangling operations. The entangling blocks themselves consist of a CZ gate and a parameterized single-qubit rotation on the two involved qubits. The control and target for each two-qubit block are determined uniformly at random, i.e. the exact instance of an ansatz is defined by the random seed that was used for generating it. A more general version of this ansatz is detailed in figure 13.

information assumes unital noise, and the efficient evaluation of $\mathcal{R}_Q$ has been tied to either isotropic channels, or more general Pauli noise under restrictions to CHZ circuits [76]. In contrast, the distinguishability loss is defined for arbitrary CPTP maps, and its two-design approximation $\mathcal{D}_{\mathcal{S}}$ ensures efficient evaluation. In this sense, the distinguishability loss generalizes the intuition behind the recoverable quantum information, and establishes an efficiently computable objective for learning noise-tailored encodings under arbitrary noise.

4.2 Variational Quantum Error Correction

The underlying concept we propose is agnostic to the specific optimization method used. One could, for instance, employ the distinguishability loss as a reward function in a reinforcement learning framework that incrementally constructs the encoding circuit [34, 77], or encode it into the fitness function of an evolutionary algorithm [89, 99].

In this work, for a proof-of-principle demonstration of the concept, we choose to formulate the task as a variational quantum algorithm [20]. We first select a variational ansatz $U_{\text{enc}}(\Theta)$ for the encoding unitary, with trainable parameters Θ. Therefore, we utilize a newly developed REA, which features an initial single-qubit layer, followed by randomly placed two-qubit blocks. An exemplary instance of such a layout is shown in figure 3. The motivation for this ansatz is to allow searching for well-suited shallow circuit instances by iterating over layouts with varying two-qubit placements. Furthermore, a REA can easily be made hardware-efficient by restricting to two-qubit gates that allow for native realization on the hardware. The parameters can be optimized using either gradient-free or gradient-based optimization methods. We employ the quasi-Newton limited-memory BFGS (L-BFGS) algorithm [63] due to its fast convergence for medium-sized models. However, conceptually, other optimization techniques like standard gradient descent can also be used. To enhance performance, in future work, one can also focus on a more structured approach for choosing optimal circuit architectures, using e.g. differentiable architecture search [117] or incrementally growing the ansatz [40].

For training the parameterized encoding ansatz $U_{\text{enc}}(\Theta)$, we employ the distinguishability loss as a training objective. As argued above, optimizing the worst-case loss directly is difficult. Therefore, we use the approximate average-case loss as an effective and stable proxy:

$$\min_{\Theta} \mathcal{D}_{\mathcal{S}}(\mathcal{N};\Theta) \tag{22}$$

While it trivially holds that $\mathcal{D}_{\mathcal{S}}(\mathcal{N};\Theta) \approx \mathcal{D}(\mathcal{N};\Theta) \leq \overline{\mathcal{D}}(\mathcal{N};\Theta)$, in practice, we observe $\mathcal{D}_{\mathcal{S}}(\mathcal{N};\Theta) \not\propto \overline{\mathcal{D}}(\mathcal{N};\Theta)$. In all considered scenarios, this relation was sufficient to guarantee a good validation performance quantified by the worst-case loss $\overline{\mathcal{D}}(\mathcal{N};\Theta)$.

Due to its resemblance to a variational quantum algorithm, we denote this realization of the training procedure as *variational quantum error correction*. The resulting circuits are dubbed VarQEC codes, and grouped by their code parameters $((n, 2^k))$. While in section 4.4 we also derive a methodology to quantify the code distance d of VarQEC codes, in general, and by construction, the VarQEC procedure does not explicitly enforce the ability to recover information under specific error terms. Rather, the distinguishability loss is used to automatically focus on specific error terms to minimize the overall loss of information. The described training procedure is conceptually illustrated in figure 4.

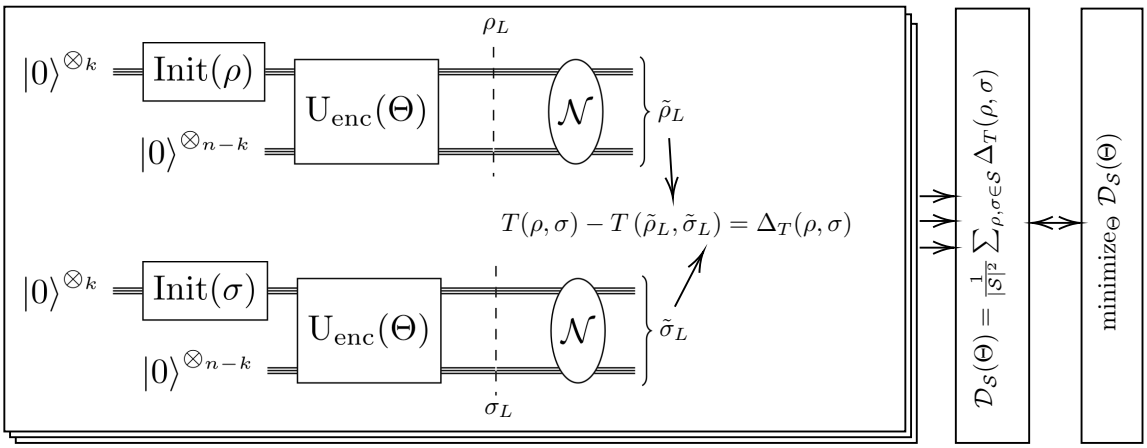

Figure 4. Pipeline of learning VarQEC encodings with the distinguishability loss (adapted and extended from [70]). Pairs of k-qubit states from a two-design $\mathcal{S}$ are prepared and encoded into an n-qubit Hilbert space with the encoding unitary $U_{\text{enc}}(\Theta)$. The resulting encoded states are subjected to the noise channel $\mathcal{N}$, before the trace distance between the disturbed states is evaluated. The difference to the baseline trace distance is computed and denoted as the *lost trace distance* $\Delta_T(\rho, \sigma; \mathcal{N}; \Theta)$. This information is averaged over all state pairs $\rho, \sigma \in \mathcal{S}$, giving the two-design approximation to the average-case distinguishability loss $\mathcal{D}_{\mathcal{S}}(\mathcal{N}; \Theta)$. This objective is minimized with a suitable technique, in this paper instantiated as a variational quantum algorithm utilizing gradient-based optimization. The converged encoding constitutes a $((n, 2^k))$ code – either for exact or approximate QEC, depending on the setup – finetuned for the noise channel $\mathcal{N}$.

4.3 Generating Recovery Operations

While the main focus of our paper is the encoding operation, it is also important to construct fitting recovery operations U_{rec} for practical error correction. Therefore, we adopt a learning-based method inspired by the QVECTOR procedure [50] to obtain optimal parameters Φ for a variational ansatz $U_{\text{rec}}(\Phi)$:

For training the recovery operation, one defines the *average-case fidelity loss* between the original state ρ and the recovered state $\hat{\rho}$ as

$$\mathcal{F}(\mathcal{N}; \Theta, \Phi) = 1 - \int_{\rho} F(\rho, \hat{\rho})\, d\nu(\rho), \tag{23}$$

where again ρ are Haar-random states. Similar to the distinguishability loss, we can also define a worst-case version

$$\overline{\mathcal{F}}(\mathcal{N}; \Theta, \Phi) = 1 - \min_{\rho} F(\rho, \hat{\rho}). \tag{24}$$

Interestingly, the two-design approximation of the average-case loss

$$\mathcal{F}_{\mathcal{S}}(\mathcal{N}; \Theta, \Phi) = 1 - \frac{1}{|\mathcal{S}|} \sum_{\rho\in\mathcal{S}} F(\rho, \hat{\rho}), \tag{25}$$

is exact, i.e. $\mathcal{F} = \mathcal{F}_{\mathcal{S}}$, as the loss function involves at most second-order moments [6]. In the original QVECTOR approach, one trains both the encoding and recovery operations with this loss, i.e. minimizes w.r.t. both parameter sets Θ and Φ. As we have already obtained an encoding operation by training for the distinguishability loss, we focus solely on training the recovery unitary:

$$\min_{\Phi} \mathcal{F}_{\mathcal{S}}(\mathcal{N}; \Theta, \Phi) \tag{26}$$

In the experimental section, we demonstrate that our proposed two-step procedure, i.e. first optimizing the encoding and then the recovery operation, is superior to the end-to-end QVECTOR method. Moreover, the distinguishability loss also allows for determining sophisticated encoding operations, completely abstracted from the recovery technique.

While our training of recovery operations in equation (26) is only slightly modified from the QVECTOR procedure [50], the overall VarQEC framework is substantially more general and should not be viewed as a merely incremental extension. In QVECTOR, encoding and recovery are optimized simultaneously with respect to an average-case fidelity loss, tightly coupling the learned

encoding to a particular recovery ansatz. In contrast, VarQEC first learns an encoding by minimizing the distinguishability loss $\overline{\mathcal{D}}$ via its average-case two-design proxy $\mathcal{D}_{\mathcal{S}}$), which both are based on the trace distance. This procedure comes with analytic guarantees relating $\overline{\mathcal{D}}$ to the worst-case fidelity after recovery, and an approximate code distance, as discussed in section 4.4. Only in a second, modular step, we train the recovery operation using a QVECTOR-like fidelity objective, so that QVECTOR effectively appears as one possible instantiation of the recovery stage on top of our novel encoding-centric objective. This separation enables using the same learned encodings with different coherent (or, in future work, potentially also measurement-based) recovery strategies, which is not supported by the original end-to-end QVECTOR formulation. Empirically, we find that this two-stage, distinguishability-driven approach yields encodings that match or surpass established codes and consistently outperform QVECTOR-style end-to-end training, where fidelity-only optimization often fails to converge to useful solutions (see section 5.3).

4.4 Properties of Learned Codes

As elaborated above, by construction, the VarQEC procedure does not explicitly enforce the ability to recover information from specific error types. Instead, the distinguishability loss naturally guides the encoding to focus on the most detrimental errors, minimizing the overall loss of information. As a result, VarQEC codes should, in general, be classified as approximate QEC codes.

However, we find that certain instances of VarQEC codes can achieve exact error correction. In particular, we verify this by evaluating the distinguishability loss of the code under all possible weight-w errors. If all of these error patterns yield zero loss, then the code is said to have code distance $d = w + 1$. The empirical method is described in more detail in appendix B.3. In particular, this analysis reveals that VarQEC codes with parameters $((n \geq 5, 2))$ trained on depolarizing noise exhibit a code distance of $d = 3$, matching the $[[5, 1, 3]]$ perfect code [57]. However, we again want to emphasize that the objective of VarQEC is not to generate codes with a certain provable code distance, but to develop low-overhead codes tailored for the specific noise channel.

As further motivation for training with the distinguishability loss, we derive a theoretical relationship to the worst-case fidelity after recovery. We state this connection informally here, with the formal proof deferred to appendix B.2.

Theorem (Upper bound on fidelity loss, informal)**.** *The worst-case distinguishability loss $\overline{\mathcal{D}}$ under a noise channel $\mathcal{N}$ guarantees the existence of a recovery operation that achieves a worst-case fidelity loss bounded by:*

$$\overline{\mathcal{F}}(\mathcal{N}) \leq 1 - \left(1 - \overline{\mathcal{D}}(\mathcal{N})\right)^2 \tag{27}$$

Consequently, a lower distinguishability loss ensures a lower fidelity loss, meaning a higher worst-case fidelity after recovery.

This theorem provides theoretical motivation for minimizing the distinguishability loss when designing encoding operations. We note that the bound of equation (27) is not tight, i.e. in practice one can achieve an even better recovery fidelity. In the experimental section, we also empirically demonstrate that a lower distinguishability loss correlates with higher fidelity after recovery.

5 Empirical Evaluations

In this section, we present empirical evaluations of the proposed VarQEC method. We, for now, focus on training and validation in simulation, which we will complement with deployment of actual quantum devices in section 6. The employed ansätze and the experimental setup are detailed in appendix D. We assess the performance of VarQEC codes under symmetric and asymmetric depolarizing noise in the following, and defer considerations of various other noise models and setups with multiple logical qubits to appendix E.

5.1 Distinguishability Loss of Encodings

We begin by evaluating the distinguishability loss of different QEC and VarQEC codes when subjected to depolarizing noise. In addition, we simulate the same noise on an unencoded qubit as a baseline (see appendix B.1 for analytical justification). Figure 5(a) illustrates the distinguishability loss for this baseline, the $[[5, 1, 3]]$ perfect code [57], and VarQEC codes with parameters $((4, 2))$, $((5, 2))$ and $((7, 2))$. For all instances, the worst-case loss $\overline{\mathcal{D}}$, as well as the average-case loss $\mathcal{D}$, is displayed. Additionally, we indicate the two-design approximation values if

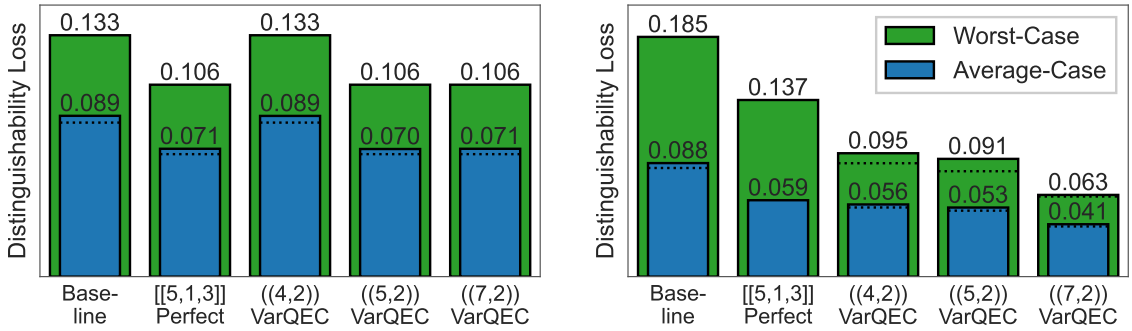

(a) Depolarizing noise with noise strength $p = 0.1$.

(b) Asymmetric depolarizing noise with noise strength $p = 0.1$ and asymmetry $c = 0.5$ following equation (45).

Figure 5. Distinguishability loss for different QEC codes on (a) depolarizing and (b) asymmetric depolarizing noise. All bars visualize the average-case loss $\mathcal{D}$ and worst-case loss $\overline{\mathcal{D}}$. Additionally, the two-design approximations $\mathcal{D}_{\mathcal{S}}, \overline{\mathcal{D}}_{\mathcal{S}}$ are visualized as dotted lines if the approximation was not exact. For both noise models, the baseline of an unencoded qubit, the $[[5, 1, 3]]$ *perfect* code [57], and VarQEC codes with $n = 4$, $n = 5$, and $n = 7$ physical qubits are compared. All VarQEC ansätze are trained for 10 epochs and contain $(n - 1) \cdot (n - 2)$ two-qubit blocks. Results on additional noise models can be found in figure 14, an extension to two data qubits is discussed in figure 16.

they deviate from the ground-truth. We note that these values are themselves estimated with 1000 Haar-random states, which is, however, sufficient for an accuracy of 10^{-4} (see appendix B.4). In this context, we have to remember that the $[[5, 1, 3]]$ perfect code is the smallest code that can correct for arbitrary single-qubit errors [57]. Therefore, it is expected that it serves as a kind of lower bound for the specific setup of symmetric depolarizing noise. Indeed, the smaller VarQEC code with only $n = 4$ physical qubits cannot improve the loss beyond the unencoded baseline of $\overline{\mathcal{D}} = 0.133$. However, if we consider VarQEC models with $n \geq 5$ qubits, these perform on par with the loss of $\overline{\mathcal{D}} = 1.106$ of the perfect QEC code. In that respect, we consider the slightly improved average-case performance of the $((5, 2))$ code with $\mathcal{D} = 0.070$ only an artifact of the evaluation procedure, and not an actual performance improvement. We empirically confirm that the $((5, 2))$ VarQEC code exhibits a code distance of $d = 3$, allowing for correcting single-qubit errors with a high fidelity (see appendix B.3). Moreover, in section 5.3 we demonstrate that these VarQEC codes allow for practically exact error correction on depolarizing noise. Overall, the learned encoding is on par with the optimal classical code for this setup.

We extend our evaluation to asymmetric depolarizing noise in figure 5(b). This noise channel represents general Pauli noise in the sense of equation (4), instantiated by a bias parameter $c = \frac{\log p_Z}{\log p_X} = \frac{\log p_Z}{\log p_Y}$ [77]. For a total noise strength of $p = 0.1$ and an asymmetry factor of $c = 0.5$, this yields the probability of an isolated phase-flip is $p_z \approx 0.085$, while the other two probabilities are $p_x = p_y \approx 0.0075$. In the presence of this asymmetry, the $[[5, 1, 3]]$ perfect code can no longer be assumed to be optimal. Indeed, already the VarQEC code with $n = 4$ qubits significantly improves the worst-case distinguishability loss. Moreover, the loss values decrease further when increasing the number of physical qubits to $n = 5$ and $n = 7$.

The results demonstrate that the VarQEC procedure can produce codes that are competitive on noise structures where optimal QEC codes are known, and develop novel codes for more complex noise models.

5.2 Stability and Fault Resilience

We further analyze the stability and resilience of the VarQEC codes and VarQEC procedure in general in figure 6. The experiments in figure 6(a) on varying asymmetry levels highlight the adaptability of the VarQEC procedure. For all setups from $c = 0.5$, i.e. mostly phase-flips, to $c = 2.0$, i.e. mostly bit-flips and combined bit- and phase-flips, all codes exhibit a distinguishability loss significantly beyond the unencoded baseline. The *static* version of the $((5, 2))$ VarQEC code (marked by $((5, 2)^*)$, i.e. the code learned on the symmetric setup $c = 1.0$ from figure 5(a), outperforms the $[[5, 1, 3]]$ perfect QEC code especially on setups with high asymmetries. Moreover, as one could expect, the improvement when training the VarQEC codes explicitly on the respective noise structure also increases with larger asymmetries. In this context, we refer to the codes noted by $((5, 2))$ as *dynamically* trained codes.

In a more realistic scenario, one has to assume that the encoding operations themselves are non-ideal, which is typically considered within the context of fault-tolerant quantum

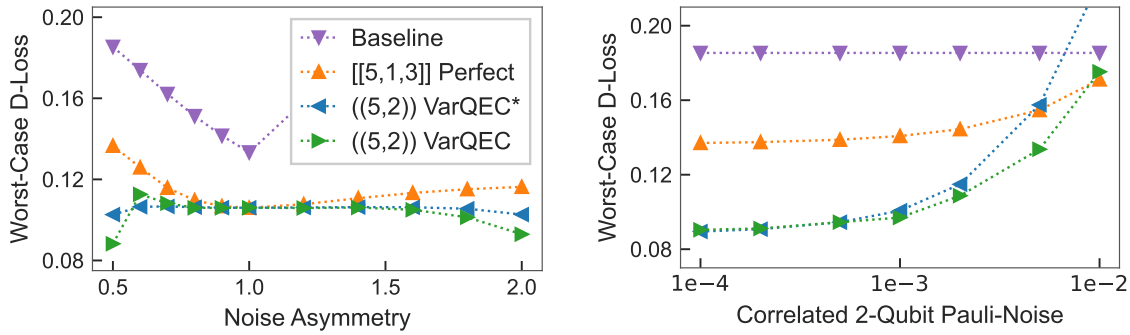

(a) Asymmetric depolarizing noise with a noise strength of $p = 0.1$ and asymmetry c as denoted on the x-axis. For $c < 1$ the noise landscape is dominated by Z errors, while for $c > 1$ mainly X and Y errors occur, compare equation (45).

(b) Performance of noisy encoding operations on asymmetric depolarizing noise with a noise strength of $p = 0.1$ and asymmetry $c = 0.5$. In contrast to the other experiments, the gates in the encoding themselves are assumed to be non-ideal. To simulate this, correlated depolarizing noise of strength as denoted on the x-axis is added after each two-qubit operation, compare equation (51).

Figure 6. Stability and resilience of standard QEC and VarQEC codes in setups of (a) varying noise asymmetry and (b) non-ideal encoding operations. All data points represent the respective worst-case distinguishability loss $\overline{\mathcal{D}}$. The $((5,2))^*$ VarQEC code is always the same *static* one trained on symmetric depolarizing noise with noise strength $p = 0.1$ and under the assumption of ideal encoding operations.

computing [93]. However, this fault-tolerance analysis typically requires some highly formalized understanding of the involved encoding circuit structures, which has not been established yet for the VarQEC codes. Therefore, we approach this topic from a more empirical perspective, and therefore dub this analysis as the *fault-resilience* of the encodings. In figure 6(b), we do this by adding correlated depolarizing noise (see equation (51)) of increasing strength after each two-qubit operation in the encoding. This is motivated by the observation that on current hardware systems, most error-prone operations are these involving multiple qubits. While single-qubit fidelity is already quantified around 99.99%, two-qubit gate fidelity is just recently approaching the infamous *three 9's* [31, 68]. We do not claim that these gate fidelities can be directly related to the noise strength in figure 6(b). However, one can see that for a two-qubit gate fidelity beyond a certain threshold, the VarQEC encodings are reasonably fault-resilient. Moreover, for a wide range of error rates, they outperform the (also not fault-tolerant) encoding of the $[[5,1,3]]$ perfect code, which only gradually catches up due to shallower circuit depth. Simulating the two-qubit errors already during the training procedure and therefore dynamically tailoring the codes further improves the results. The successful deployment of VarQEC encodings on quantum hardware we conduct in section 6 underlines these fault-resilience properties.

In appendix E.4 we analyze fault-resilience under the assumption of restricted connectivity, which further strengthens the case for the VarQEC encodings. It is left for future work to enrich the approach with guarantees on actual fault-tolerance, e.g. by sufficiently extending the learning-based approach to simultaneously learn flag-gadgets [23, 114].

5.3 Fidelity Loss with Recovery

Finally, we analyze the achievable fidelities after recovery for the noise channels and models we already considered in section 5.1. This is quantified using the worst-case and average-case fidelity loss from equations (23) and (25), which is evaluated over a two-design. In figure 7 we compare the unencoded baseline and 3 code types: First, the $[[5,1,3]]$ perfect QEC code with its static encoding and recovery operation. Second, three versions of a VarQEC code with $n = 5$ physical qubits, one denoted as $((5,2))^*$ with a randomly initialized untrained encoding, one referred to as $((5,2))^{**}$ where the distinguishability loss has converged to a local optimum, and the $((5,2))$ VarQEC code from figure 5 where the encoding produces a presumably globally optimal distinguishability loss. The recovery operation is trained successively following equation (26). Third, a code with $n = 5$ physical qubits where the encoding is not pre-trained, but encoding and recovery operations are simultaneously learned with the QVECTOR approach [50], for details refer to appendix C. We note that as we consider the single-recovery scenario, we do not employ additional recovery qubits for the variational models [50]. We list the respective distinguishability losses of the encodings and the bounds on the fidelity for the VarQEC models following Theorems 1 and 2 in table 1.

The results in figure 7(a) on symmetric depolarizing noise demonstrate that a lower

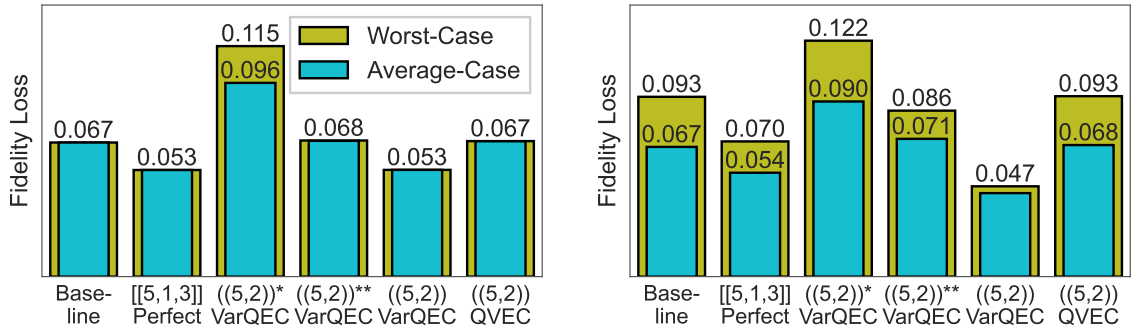

(a) Depolarizing noise with noise strength $p = 0.1$.

(b) Asymmetric depolarizing noise with noise strength $p = 0.1$ and asymmetry $c = 0.5$ following equation (45).

Figure 7. Fidelity loss for different QEC codes and respective recovery operations on (a) depolarizing and (b) asymmetric depolarizing noise. All bars visualize the average-case loss $\mathcal{F}$ and worst-case loss $\overline{\mathcal{F}}$. For both noise models, the baseline of an unencoded qubit and the $[[5, 1, 3]]$ *perfect* code are visualized. Additionally, we compare three instances of VarQEC codes, where $((5, 2))^*$ employs a random encoding, $((5, 2))^{**}$ employs an encoding that has converged to a locally optimal distinguishability loss, and the encoding of $((5, 2))$ has converged to a global optimum. The recovery operations are successively trained following equation (26). For the rightmost model, the encoding and recovery operations have been trained end-to-end with the QVECTOR approach [50] as described in appendix C. The recovery ansätze are trained using the fidelity loss for 50 epochs and contain 200 two-qubit blocks. As we consider a single-recovery scenario, no separate recovery register was used, i.e. the recovery operation acts solely on the n-qubit encoded and disturbed state [50]. The distinguishability loss for all encodings is summarized in table 1. Results on additional noise models can be found in figure 15.

		Base-line	$[[5,1,3]]$ Perfect	$[[5,1]]^*$ VarQEC	$[[5,1]]^{**}$ VarQEC	$[[5,1]]$ VarQEC	$[[5,1]]$ QVEC
symmetric depolarizing	$\overline{\mathcal{D}} =$	0.133	**0.106**	0.215	0.133	**0.106**	0.133
	$\overline{\mathcal{F}} \leq$			0.216	0.249	0.201	
	$\overline{\mathcal{F}} =$	0.067	**0.053**	0.115	0.068	**0.053**	0.067
	$\overline{\mathcal{F}} \geq$			0.013	0.018	0.011	
asymmetric depolarizing	$\overline{\mathcal{D}} =$	0.185	0.137	0.237	0.161	**0.091**	0.185
	$\overline{\mathcal{F}} \leq$			0.228	0.296	0.174	
	$\overline{\mathcal{F}} =$	0.093	0.070	0.122	0.086	**0.047**	0.093
	$\overline{\mathcal{F}} \geq$			0.015	0.026	0.008	

Table 1. Worst-case distinguishability loss $\overline{\mathcal{D}}$ exhibited by the encodings for the models in figure 7. For the baseline and $[[5, 1, 3]]$ code, this is evaluated on the unencoded baseline and static encoding operation, respectively. For the VarQEC codes, this corresponds to an untrained encoding for $((5, 2))^*$, to a local optimum for $((5, 2))^{**}$, and to a global optimum for $((5, 2))$. For the $((5, 2))$ QVECTOR code, the same ansatz with 12 two-qubit blocks as for the VarQEC codes is employed, but training was only implicitly conducted via the fidelity loss. Additionally, we again report the worst-case fidelity loss $\overline{\mathcal{F}}$ (third line) and the respective upper (second line) and lower bounds (fourth line) following Theorems 1 and 2 for the VarQEC models.

distinguishability loss of the encoding correlates with a lower fidelity loss, i.e. a higher fidelity after recovery. The results on the untrained VarQEC encoding and the one converged to a local optimum are below or just at the unencoded baseline, which further underlines the importance of the training procedure. We highlight that the optimal $((5, 2))$ VarQEC code achieves, up to numerical accuracy, an identical fidelity of $1 - 0.053 = 0.947$ as the $[[5, 1, 3]]$ perfect code, which underlines the potential code distance of $d = 3$ of this code and the interpretation as practically exact error correction. The $((5, 2))$ QVECTOR code is not successful in improving the fidelity beyond the unencoded baseline of $1 - 0.067 = 0.933$. We can observe qualitatively similar results on the asymmetric depolarizing noise channel in figure 7(b). Moreover, here the $((5, 2))$ VarQEC code guarantees a worst-case fidelity of $1 - 0.047 = 0.953$, which significantly improves upon the $[[5, 1, 3]]$ QEC code with a fidelity of only $1 - 0.070 = 0.930$. Again, the QVECTOR approach is not able to improve the fidelity beyond the unencoded baseline.

Regarding the QVECTOR results, we want to note that we employed the same ansätze as for the best VarQEC codes. Consequently, the underlying models in principle are guaranteed to be expressive enough to also produce the same competitive results. However, for the considered setups, the end-to-end training procedure based purely on the fidelity loss is unable to produce sophisticated codes. The results in table 1 indicate that this is mostly because the resulting encoding operations do not sufficiently protect the state information before application of the noise channel. This does not contradict the results from the original QVECTOR work [50], as we consider

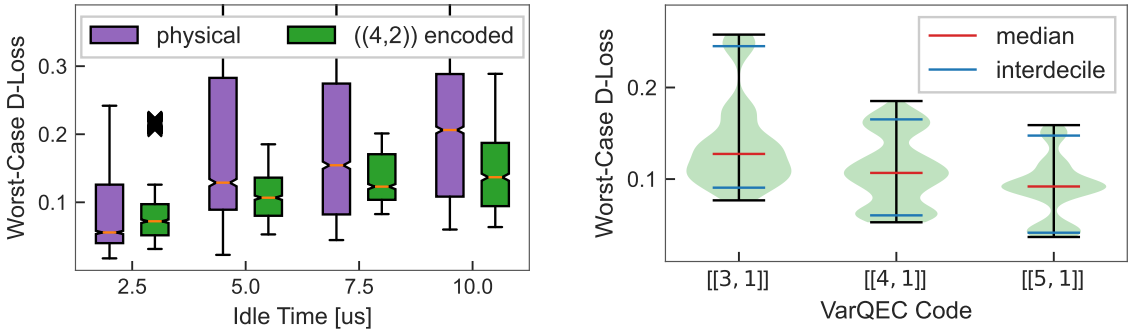

(a) The $((4,2))$ VarQEC code is trained in simulation for a noise duration of 10.0μs. We deploy the model on the QPU for delays varying from 2.5μs to 10.0μs. The bar plots visualize the distribution of the worst-case distinguishability loss over multiple logical patches, with orange lines denoting the median and outliers exceeding 1.5 times the interquartile range marked separately.

(b) VarQEC codes with increasing number of physical qubits, i.e. $((3,2))$, $((4,2))$, and $((5,2))$ are trained in simulation for a noise duration of 10.0μs. To account for additional sources of errors, like noise introduced during the encoding operation itself and measurement delays, the delay is reduced to 5.0μs for hardware deployment. The violin plots visualize the distribution of the worst-case distinguishability loss over multiple logical patches.

Figure 8. Experiment on the `ibm_marrakesh` device [85], which features a 156-qubit `Heron r2` chip. We induce thermal relaxation noise by applying a delay on all wires for a specific duration, assuming a median $T_1 = 180\mu$s and $T_2 = 120\mu$s. The VarQEC codes are trained in classical simulation assuming these noise hyperparameters. Evaluation is conducted on hardware simultaneously on 8 logical patches distributed uniformly over the QPU. We successively apply cluster re-sampling to enhance the granularity of data points [17, 73]. Additional details on the experimental procedure and the reconstruction of the worst-case distinguishability loss $\overline{\mathcal{D}}$ via mitigated state tomography can be found in the appendix. The predictions of the distinguishability loss from the simulation can be found in figure 21(a).

more complex and stronger noise channels and employ ansätze with significantly fewer parameters.

In summary, our empirical evaluations demonstrate that VarQEC codes, trained using the distinguishability loss, outperform traditional QEC codes in various noise scenarios. The codes offer stable performance across multiple noise models and are furthermore fault-resilient, assuming a sufficiently large physical operation fidelity.

6 Hardware Experiments

In this section, we extend our experiments to actual quantum hardware to validate the practical applicability of our proposed VarQEC codes. We deploy our models on the 156-qubit `ibm_marrakesh` device featuring a `Heron r2` chip provided by the IBM Quantum services [85]. The experiments involve running multiple logical patches in parallel on different regions of the chip. We compare the unencoded baseline to the logical patches, reconstructing the distinguishability loss using mitigated state tomography [52]. Details on the experimental procedure and the reconstruction method are summarized in appendix F.1. The implementation of the deployment procedure on hardware and the raw results are provided as noted in the data availability statement.

To control noise, we idle the qubits for a set duration, thereby inducing thermal relaxation noise. Mitigation techniques like dynamic decoupling were deactivated for the experiments. We identify the median properties of the `ibm_marrakesh` qubits to be $T_1 = 180\mu$s and $T_2 = 120\mu$s. We adapt our ansatz directly to the heavy-hex lattice of the device, selecting CZ gates as the two-qubit gates and parameterized $\mathrm{R_{zxz}} = R_z R_x R_z$ gates as single-qubit rotations to align with the native gate set. We train models on $n = 3$, $n = 4$, and $n = 5$ qubits in simulation with a noise duration of $t = 10.0\mu$s.

In figure 8(a), we present results for several delay values ranging from $t = 2.5\mu$s to $t = 10.0\mu$s for a $((4,2))$ VarQEC code trained at $t = 10.0\mu$s. We observe that the baseline physical distinguishability loss increases sharply with increasing delay duration, while the distinguishability loss for encoded patches increases much more slowly, demonstrating the effectiveness of our encoding in preserving quantum information over time. Since our training in simulation assumes ideal encoding operations, we reduce the noise duration to $t = 5.0\mu$s in the subsequent experiment shown in figure 8(b) to partially account for additional sources of error such as noise introduced during the encoding operations themselves and measurement delays. We also train and deploy $((3,2))$ and $((5,2))$ VarQEC codes. The most important observation is that with an increasing number of physical qubits, the distinguishability loss decreases, indicating improved error correction performance with larger codes. We did not explicitly report hardware results for the

[[5, 1, 3]], as after compilation to the restricted topology, the encoding circuit gets quite deep. Initial trials revealed that execution and successive tomography on hardware yield close-to-random measurement outcomes, due to accumulating noise.

Reliably predicting and quantifying scalability behavior from this limited data is challenging and is left for future work, as it requires extensive access to hardware platforms. In principle, these results could be improved by refining the noise model of the device, i.e. incorporating two-qubit correlated noise directly into the training procedure. We analyze the experiments and the results on the individual patches in more detail in appendix F.2. Furthermore, we extend our experiments to a 20-qubit IQM Resonance device [87] in appendix F.3, where we demonstrate similar results. While the hardware limits qubit stability to shorter durations, its uniform qubit performance is beneficial for our procedure, since our training relies on consistent noise levels across all qubits. Overall, these experiments demonstrate the practicality and adaptability of our approach across multiple existing hardware platforms.

7 Discussion of Future Extensions

Throughout this paper, we have demonstrated that the VarQEC procedure is highly flexible and adaptable to various noise channels. The resulting codes exhibit desirable properties, are stable, and are noise-resilient. This effectiveness has also been demonstrated on actual quantum hardware.

Despite these promising results, we acknowledge that there are open problems and limitations associated with our procedure. These challenges are not unique to our proposal but are present in most AI-based approaches to QEC. We focus particularly on the open tasks surrounding the encoding operations, as recovery operations are not the primary target of this work. We see the main limitations as follows:

i. The evaluation of the two-design approximation scales exponentially with the number of logical qubits as 4^k.

ii. The current formulation requires simulating the underlying quantum circuits, restricting the approach to system sizes that are classically tractable.

iii. Instantiating the method as a variational algorithm may introduce the problem of barren plateaus for increased circuit size and depth [67], making training challenging.

We now outline potential future extensions, in particular addressing, but not limited to above-stated caveats:

Code concatenation offers the possibility to compose a larger QEC code from several smaller codes, enhancing the overall code distance and error correction capability [54]. This concept has to be extended to the approximate QEC setup, focusing more on performance under specific noise models rather than on achieving a specific code distance. By using smaller, modular codes, we can mitigate the exponential scaling issue (limitation i) and reduce the computational resources required for simulation (limitation ii). Additionally, working with smaller circuits helps alleviate the barren plateau problem (limitation iii).

Patch-based logical qubits eliminate the necessity to realize a large number of logical qubits within a single code patch. This concept is especially present in surface codes [35], where single-qubit logical patches are interacted via techniques like lattice surgery [47]. Developing similar procedures for VarQEC codes, potentially by variational learning logical operations between code patches [24], ensures the overhead for evaluating the loss function to be constant (limitation i).

Training directly on quantum hardware, inspired by the QVECTOR approach [50], eliminates the necessity to simulate the involved circuits (limitation ii). However, this requires either a tractable method to estimate the involved trace distance on hardware, using e.g. variational techniques [25]. Alternatively, one might resort to an easier-to-evaluate loss proxy such as the Hilbert-Schmidt distance [36].

Barren Plateau-free Ansätze have recently been proposed in the literature [32, 79], resolving the potential trainability issues (limitation iii). While there is debate about whether the absence of barren plateaus implies classical simulability [21], this is less problematic for encoding operations in QEC. In particular, encoding operations for stabilizer codes are purely Clifford operations. Alternatively, we can modify the loss function to serve as an RL reward function and develop fast tableau-based simulators, similar to methods used with the Knill-Laflamme conditions [77]. However, finding such efficient ways to approximate the trace distance with sufficient accuracy remains an open question.

In summary, we identified several avenues to address the current challenges in the VarQEC approach, particularly concerning the distinguishability loss and scalability. While it is not yet clear which path will be the most effective, the promising preliminary results presented in this paper catalyze future research.

8 Summary and Conclusion

In this paper, we introduced a novel approach for learning quantum error correction (QEC) codes by minimizing an objective called the distinguishability loss. This procedure ensures that the distinguishability between quantum states, quantified by the trace distance, is preserved after passing through a noise channel, which is crucial for effective recovery operations. We formalized this relationship by deriving bounds and guarantees on the fidelity after recovery. Additionally, we introduced a method to evaluate the code distance of a QEC code purely based on the distinguishability loss. By minimizing the loss of trace distance over a two-design ensemble of states, we provide an efficient evaluation method suitable for incorporation into machine learning routines.

We incorporated the distinguishability loss function into a variational algorithm, termed variational quantum error correction (VarQEC). This procedure trains the parameters of a variational ansatz to tailor the encoding to the most detrimental errors of a given noise model. We also modified and integrated an established routine to construct a recovery operation, enabling a full QEC cycle. The extensive empirical evaluations highlight the flexibility and adaptability of the VarQEC procedure. The learned VarQEC codes are shown to be stable and noise-resilient, outperforming similar-sized standard QEC codes in various scenarios. The deployment of VarQEC code instances on IBM and IQM hardware demonstrates the practical feasibility of the procedure.

While we acknowledge current limitations surrounding our proposed VarQEC approach, particularly the scalability to larger code instances, we are confident that the potential for future improvements and extensions enables a sophisticated learning-based approach to QEC. Moreover, we note that the formulation as a variational algorithm is just one specific instance of a procedure based on the distinguishability loss. In principle, it can be incorporated into a wide range of AI-based techniques, including reinforcement learning and evolutionary procedures.

In conclusion, our work highlights the importance of overhead reduction and noise tailoring in advancing QEC. By leveraging the distinguishability loss, we provide a flexible framework for developing QEC codes optimized for specific noise characteristics and hardware constraints. This approach is well-suited for the era of early fault-tolerant quantum computing, where resource efficiency and adaptability are paramount. Future research can build upon this foundation to explore larger systems, implement fault-tolerant logical operations, and further integrate our approach with noise-tailored QEC strategies.

Acknowledgments

We acknowledge the use of IBM Quantum services for this work. The views expressed are those of the authors and do not reflect the official policy or position of IBM or the IBM Quantum team.

We acknowledge the use of IQM Resonance services for this work. The views expressed are those of the authors and do not reflect the official policy or position of IQM or the IQM Resonance team.

The authors gratefully acknowledges the scientific support and HPC resources provided by the Erlangen National High Performance Computing Center (NHR@FAU) of the Friedrich-Alexander-Universität Erlangen-Nürnberg (FAU). The hardware is funded by the German Research Foundation (DFG).

Some results of this study were previously reported in condensed form in [70]; here we present the complete, significantly extended version.

Funding

The research was supported by the Bavarian Ministry of Economic Affairs, Regional Development and Energy with funds from the Hightech Agenda Bayern via the project BayQS, and partially by the German Federal Ministry of Research, Technology and Space, funding program Quantum Systems, via the project Q-GeneSys, grant number 13N17389. The research is also part of the Munich Quantum Valley (MQV), which is supported by the Bavarian state government with funds from the Hightech Agenda Bayern Plus.

Data availability

The pipeline for training the proposed VarQEC codes, including the distinguishability loss function and all other required components, is available at https://github.com/nicomeyer96/varqec. The enclosed README provides setup details and instructions for reproducing the results of the paper. The scripts for employing trained codes on IBM and IQM hardware, as well as the raw results and analysis methods, are available separately at https://github.com/nicomeyer96/varqec-experiment. Further information and data are available upon reasonable request.

Appendix A: Background and Definitions

This appendix summarizes some important definitions and properties used throughout this paper that are already established in the literature. We start in appendix A.1 by providing an overview of different measures on and between quantum states. The various quantum noise channels that are considered in this paper are formally introduced in appendix A.2.

A.1 Measures on Quantum States

There exist various measures on and between quantum states, of which the *trace distance*, *fidelity*, and partially the *quantum relative entropy* are relevant to our work. In general, one can note an arbitrary pure n-qubit quantum state using the Dirac notation as

$$|\psi\rangle \in \mathcal{H}^{\otimes n}, \tag{28}$$

where $H^{\otimes n}$ is the associated 2^n-dimensional Hilbert space, and it holds $\langle\psi|\psi\rangle = 1$. Alternatively, one can use the density matrix notation, in which the same pure state can be expressed as

$$\rho = |\psi\rangle\langle\psi|\,. \tag{29}$$

For pure states, this matrix has rank 1, is idempotent, and also has trace 1. A mixed state, which e.g. results from a noise channel being applied to an initially pure state, is a statistical ensemble of pure states. Formally, it is a convex combination of pure state projectors, i.e.,

$$\rho = \sum_i p_i\,|\psi_i\rangle\langle\psi_i|\,, \tag{30}$$

where $p_i \geq 0$ and $\sum_i p_i = 1$. A density matrix representing a mixed quantum state is hermitian, positive semi-definite, has trace 1, and has a rank greater than 1 [76]. One can use different measures to quantify how different two states are, all with different properties and interpretations.

The **trace distance** between two quantum states ρ, σ represents the maximum probability of distinguishing ρ from σ in a single measurement, and is defined as

$$\begin{aligned} T(\rho,\sigma) &= \frac{1}{2}\|\rho-\sigma\|_1 && (31)\\ &= \frac{1}{2}\mathrm{Tr}\left[\sqrt{(\rho-\sigma)^\dagger(\rho-\sigma)}\right] && (32)\\ &= \frac{1}{2}\sum_{i=1}^{r}|\lambda_i|\,, && (33) \end{aligned}$$

where λ_i are the eigenvalues of $\rho - \sigma$, and r it the rank. The trace distance satisfies the properties of a metric, and is bounded by $0 \leq T(\rho,\sigma) \leq 1$. A value of 0 thereby indicates that both states are identical, while a value of 1 implies that the states are orthogonal [36]. The trace distance is invariant under unitary operations U, i.e. $T(U\rho U^\dagger, U\sigma U^\dagger) = T(\rho,\sigma)$. Furthermore, it is contractive for CPTP maps Φ, such as quantum noise channels, following the data processing inequality [103], i.e. $T(\Phi(\rho),\Phi(\sigma)) \leq T(\rho,\sigma)$.

An alternate distance measure is the **fidelity** [51], which quantifies the closeness or overlap between quantum states ρ and σ. For arbitrary quantum states, it is defined as

$$\begin{aligned} F(\rho,\sigma) &= \left(\mathrm{Tr}\left(\sqrt{\sqrt{\rho}\sigma\sqrt{\rho}}\right)\right)^2 && (34)\\ &= \sum_i \sqrt{\lambda_i}, && (35) \end{aligned}$$

where λ_i are the eigenvalues of the positive semi-definite matrix $\sqrt{\rho}\sigma\sqrt{\rho}$. For pure states $\rho = |\psi\rangle\langle\psi|$ and $\sigma = |\phi\rangle\langle\phi|$ it simplifies to

$$F(\rho, \sigma) = |\langle\psi|\phi\rangle|^2 . \tag{36}$$

It is not a full metric, as it violates the triangle inequality, but can be extended to the *Bures distance*, which is a proper metric on the space of density matrices [14]. The fidelity is bounded by $0 \leq F(\rho, \sigma) \leq 1$, where a value of 1 implies equivalence of both states. The fidelity is also invariant under unitary operations and non-decreasing under completely positive trace preserving (CPTP) maps [76]. The trace distance and the fidelity are in some ways contrasting with each other, as typically a high trace distance implies a low fidelity, and vice versa. More formally, they can be related via the *Fuchs-van de Graaf inequalities* [36] as

$$1 - \sqrt{F(\rho, \sigma)} \leq T(\rho, \sigma) \leq \sqrt{1 - F(\rho, \sigma)}, \tag{37}$$

where the upper bound becomes tight if at least one of the states is pure.

Lastly, there is also the **quantum relative entropy**, which measures the informational divergence of two quantum states as

$$S(\rho\|\sigma) = \mathrm{Tr}(\rho(\log\rho - \log\sigma)). \tag{38}$$

The value range of this measure is unbounded, i.e. $0 \leq S(\rho\|\sigma) \leq \infty$, with again $S(\rho\|\sigma) = 0$ if both states are identical [106]. In general, the quantum relative entropy is not symmetric and also does not satisfy the triangle inequality. Similar to the trace distance, the quantum relative entropy is also invariant under unitary operations and satisfies an equivalent version of the data processing inequality [62]. We do not explicitly use it in this paper, but mainly took its connections to the *Petz recovery map* [82] as inspiration for deriving explicit relations to the fidelity after (optimal) recovery. We argue in the main part of this paper why we can not directly employ this measure as a loss function, but instead base our objective on the trace distance. For completeness, one can relate the quantum relative entropy to the trace distance via *Pinker's inequality* [28] by

$$S(\rho\|\sigma) \geq 2 \cdot D(\rho, \sigma)^2, \tag{39}$$

and to the fidelity by [46]

$$S(\rho\|\sigma) \geq -\ln F(\rho, \sigma). \tag{40}$$

A.2 Overview of Considered Noise Channels

Most of the noise channels we consider are well-known from the literature; we just provide this summary for convenience. Additionally, we formally define an asymmetric depolarizing channel that was introduced in [77]. To begin with, we need to recall that a noise channel can be described using the *Kraus representation*

$$\mathcal{N}(\rho) = \sum_i K_i \rho K_i^\dagger, \tag{41}$$

where the K_i are the so-called *Kraus matrices* with $\sum_i K_i^\dagger K_i = \mathbb{I}$. With that notion, in the following, we define the respective noise channels by the involved Kraus matrices. For that, let us first define the standard Pauli matrices for convenience:

$$I = \begin{bmatrix} 1 & 0 \\ 0 & 1 \end{bmatrix}, \; X = \begin{bmatrix} 0 & 1 \\ 1 & 0 \end{bmatrix}, \; Y = \begin{bmatrix} 0 & -i \\ i & 0 \end{bmatrix}, \; Z = \begin{bmatrix} 1 & 0 \\ 0 & -1 \end{bmatrix} \tag{42}$$

The arguably simplest noise channel we consider, which is inspired by classical noise, is the **bit-flip channel** $\mathcal{N}_{\mathrm{bit}}$. With a probability of p a bit-flip, i.e. an X-error occurs, while with a probability of $1 - p$ the state remains unchanged. On the Bloch sphere of a single qubit, this can be visualized as shrinking along the y and z axes. The associated Kraus matrices are as follows:

$$K_0 = \sqrt{1-p} \cdot I, \; K_1 = \sqrt{p} \cdot X \tag{43}$$

Extending this to also allow for phase-flips and combinations of bit-flip and phase-flip, we arrive at the **depolarizing channel** $\mathcal{N}_{\mathrm{dep}}$. In the standard notion, it is assumed that for an overall noise strength of p, a bit-flip, a phase-flip, and the combination thereof each happen with probability of

$\frac{p}{3}$. This induces a uniform shrinking of the Bloch sphere along all axes. Again, we explicitly state the Kraus matrices:

$$K_0 = \sqrt{1-p} \cdot I,\ K_1 = \sqrt{\frac{p}{3}} \cdot X,\ K_2 = \sqrt{\frac{p}{3}} \cdot Y,\ K_3 = \sqrt{\frac{p}{3}} \cdot Z \tag{44}$$

In addition to the uniform version, in this paper we also consider an **asymmetric depolarizing channel** $\mathcal{N}_{\text{adep}}$. While there is no unambiguous definition in literature, we resort to the instance defined in [77]. It introduces a bias parameter c, for which it holds

$$c = \frac{\log p_Z}{\log p_X} = \frac{\log p_Z}{\log p_Y}, \tag{45}$$

where p_X, p_Y, p_Z denote the probability of X, Y, Z errors, respectively. Overall, it still holds $p_x + p_y + p_z = p$, where for given p and c we can determine p_X by solving

$$2p_X + p_X^c - p = 0, \tag{46}$$

and consecutively determine $p_Y = p_X$ and $p_Z = p - 2p_X$. For $c = 1$, we get a uniform depolarizing channel, for $c < 1$, Z errors are more likely than X and Y errors, and for $c > 1$, it is the other way around. For these cases, non-uniform shrinking of the Bloch sphere is induced, with the following Kraus matrices:

$$K_0 = \sqrt{1-p} \cdot I,\ K_1 = \sqrt{p_X} \cdot X,\ K_2 = \sqrt{p_Y} \cdot Y,\ K_3 = \sqrt{p_Z} \cdot Z \tag{47}$$

Another noise type we consider is described by the **amplitude damping channel** $\mathcal{N}_{\text{ad}}$, which captures the irreversible loss of energy from a quantum system to its environment, leading to spontaneous transitions from high-energy to low-energy states. Concretely, the damping probability $0 \leq \gamma \leq 1$ describes the likelihood of losing energy from the $|1\rangle$ state towards the $|0\rangle$ state, which itself remains stable under this noise model. This channel is *non-unital*, i.e. the center of the Bloch sphere is moved from its origin. The Kraus matrices are:

$$K_0 = \begin{bmatrix} 1 & 0 \\ 0 & \sqrt{1-\gamma} \end{bmatrix},\ K_1 = \begin{bmatrix} 0 & 0 \\ 0 & \sqrt{\gamma} \end{bmatrix} \tag{48}$$

The somewhat complementary **phase damping channel** $\mathcal{N}_{\text{pd}}$ describes the loss of quantum coherence without energy dissipation. It affects the relative phase between quantum states, but leaves the probability of being in $|0\rangle$ and $|1\rangle$ states unchanged. The strength of the noise is similarly captured by a damping probability $0 \leq \gamma \leq 1$. It induces a shrinking of the Bloch sphere along the x and y axes, and is described by:

$$K_0 = \begin{bmatrix} 1 & 0 \\ 0 & \sqrt{1-\gamma} \end{bmatrix},\ K_1 = \begin{bmatrix} 0 & \sqrt{\gamma} \\ 0 & 0 \end{bmatrix} \tag{49}$$

We also frequently consider a **consecutive amplitude and phase damping channel** $\mathcal{N}_{\text{apd}}$. We realize this trivially by first applying an amplitude damping channel and afterwards a phase damping channel. While in principle one can use different noise strengths, in this work we employ the same damping parameter γ for both channels. Additionally, in particular with regards to the conducted hardware experiments, we consider the **thermal relaxation channel** $\mathcal{N}_{\text{thr}}$, which describes how a qubit relaxes towards the thermal equilibrium due to interaction with the environment. In principle, it can also be modeled by a combination of amplitude and phase damping. However, it simplifies directly incorporating properties of the hardware device, in particular the T_1 and T_2 relaxation times, and the noise duration t.

In large parts of this paper, we assume that the respective noise channels independently act on the involved qubits. More formally, we use single-qubit noise channels $\mathcal{N}_j$ acting on qubit j. This allows the full noise channel on the n-qubit system to be expressed as

$$\mathcal{N} = \otimes_j^n \mathcal{N}_j, \tag{50}$$

where typically N_j is the same for all qubits. However, we additionally analyze the resilience of the encoding operations to multi-qubit correlated noise. As the employed VarQEC encoding ansätze consist of at most two-qubit interactions, we also restrict experiments to two-qubit correlated errors. In particular, we model a **correlated two-qubit depolarizing channel**, with strength p and the following $4^2 = 16$ Kraus matrices:

$$K_0 = \sqrt{1-p} \cdot II,\ K_{1-15} = \sqrt{\frac{1}{15}} \cdot P \ \text{ with } P \in \{IX, IY, IZ, XI, \cdots, ZZ\} \tag{51}$$

All noise channels represent CPTP maps, which implies that the trace distance underlies the data processing inequality as introduced in appendix A.1, i.e.

$$T(\mathcal{N}(\rho), \mathcal{N}(\sigma)) \leq T(\rho, \sigma) \tag{52}$$

for arbitrary states ρ and σ.

Appendix B: Properties of Distinguishability Loss

In this appendix, we analyze the properties of the introduced distinguishability loss from a more theoretical perspective. An empirical evaluation with the loss integrated in the introduced VarQEC pipeline can be found in the main part and in appendix E. For convenience, we re-state the definition of the distinguishability loss for a noise channel $\mathcal{N}$, both in the average-case formulation $\mathcal{D}$ and worst-case formulation $\overline{\mathcal{D}}$:

$$\mathcal{D}(\mathcal{N}; \Theta) = \int_\rho \int_\sigma T(\rho, \sigma) - T(\mathcal{N}(\rho_L), \mathcal{N}(\sigma_L))\, d\nu(\rho)\, d\nu(\sigma) \tag{53}$$

$$\overline{\mathcal{D}}(\mathcal{N}; \Theta) = \max_{\rho,\sigma} \left(T(\rho, \sigma) - T(\mathcal{N}(\rho_L), \mathcal{N}(\sigma_L))\right) \tag{54}$$

Hereby, T denotes the trace distance, and ρ_L, σ_L are the encoded states corresponding to the pure initial states ρ, σ, respectively. These are produced by applying an encoding operation U_{enc} to the k-qubit state and additional $n-k$ ancilla qubits, initialized in state $|0\rangle$:

$$\rho_L = U_{\text{enc}}(\Theta) \left(\rho \otimes |0\rangle \langle 0|^{n-k}\right) U_{\text{enc}}^\dagger(\Theta) \tag{55}$$

Optionally, to allow for training, the encoding operation can depend on adjustable parameters $U_{\text{enc}}(\Theta)$, e.g. variational rotation angles. To allow for a practically tractable evaluation, we define approximations based on a two-design $\mathcal{S}$ (see appendix B.4 for details) which reads as:

$$\mathcal{D}_{\mathcal{S}}(\mathcal{N}; \Theta) = \frac{1}{|\mathcal{S}|^2} \sum_{\rho,\sigma \in \mathcal{S}} T(\rho, \sigma) - T(\mathcal{N}(\rho_L), \mathcal{N}(\sigma_L)) \tag{56}$$

$$\overline{\mathcal{D}}_{\mathcal{S}}(\mathcal{N}; \Theta) = \max_{\rho,\sigma \in \mathcal{S}} \left(T(\rho, \sigma) - T(\mathcal{N}(\rho_L), \mathcal{N}(\sigma_L))\right) \tag{57}$$

When using these loss functions as objectives for learning quantum error correction codes, which we dub as VarQEC codes, the actual target should be to optimize the worst-case behavior. Throughout this paper, we employ the average-case formulation as a proxy for this objective, as it allows for faster and more stable training. Both, the worst-case and average-case formulation trivially are lower bounded by 0 for the case that $T(\rho, \sigma) = T(\mathcal{N}(\rho), \mathcal{N}(\sigma))$ for all state pairs ρ, σ, i.e. there is no loss of information under noise channel $\mathcal{N}$.

In the following, we analyze different properties of this distinguishability loss. We start by analytically calculating the baseline for a single physical qubit under depolarizing noise in appendix B.1. One of the central statements of this paper, the connection between the distinguishability loss and the existence of high-fidelity recovery operations, is derived in appendix B.2. In appendix B.3 we establish a direct connection between the value of the loss function and the distance of the respective code, and discuss the distinction between exact and approximate QEC. Finally, in appendix B.4 we analyze the accuracy of the two-design approximations of the loss function.

B.1 Baseline for Depolarizing Noise

We now derive the unencoded baseline for the distinguishability loss, i.e. the value of the measure for a physical state without an encoding operation. As an instance, we choose the depolarizing channel $\mathcal{N}_{\text{dep}}$, but in principle this analysis can also be extended to other noise models. Throughout most of the paper, we determine the unencoded baseline empirically, i.e. either by evaluation of two-designs or averaging over Haar-random states. The analytic findings in this section coincide with the empirical evaluations and therefore reinforce the correct functionality of our framework.

Let us start with an equivalent re-formulation of the depolarizing channel in equation (44), which interprets the noise as driving towards a maximally mixed state:

$$\mathcal{N}_{\text{dep}}(\rho) = (1-\gamma)\rho + \frac{\gamma}{2}\mathbb{I} \tag{58}$$

Hereby, p and γ are related by $\gamma = \frac{4}{3}p$. Using this formulation on pure states ρ, σ yields:

$$\mathcal{N}_{\text{dep}}(\rho) = (1 - \frac{4}{3}p)\rho + \frac{2}{3}p \cdot \mathbb{I} \tag{59}$$

$$\mathcal{N}_{\text{dep}}(\sigma) = (1 - \frac{4}{3}p)\sigma + \frac{2}{3}p \cdot \mathbb{I} \tag{60}$$

With the definition of the trace distance and the property that the trace is a linear map, the relation between the two resulting noisy states reads as

$$T(\mathcal{N}_{\text{dep}}(\rho), \mathcal{N}_{\text{dep}}(\sigma)) = \frac{1}{2}\text{Tr}\,\|\mathcal{N}_{\text{dep}}(\rho) - \mathcal{N}_{\text{dep}}(\sigma)| \tag{61}$$

$$= \left|1 - \frac{4}{3}p\right| \cdot \frac{1}{2}\text{Tr}\,|\rho - \sigma\| \tag{62}$$

$$= (1 - \frac{4}{3}p) \cdot T(\rho, \sigma), \tag{63}$$

assuming that $p \leq \frac{3}{4}$. Plugging this into the definition of the lost trace distance from equation (18) yields

$$\Delta_T(\rho, \sigma; \mathcal{N}_{\text{dep}}) = T(\rho, \sigma) - (1 - \frac{4}{3}p) \cdot T(\rho, \sigma) \tag{64}$$

$$= \frac{4}{3}p \cdot T(\rho, \sigma). \tag{65}$$

This already allows us to derive the worst-case distinguishability loss for this setup. Using equation (19) and the fact that the trace distance takes its maximum value of 1 for orthogonal pure states, we get

$$\overline{\mathcal{D}}(\mathcal{N}_{\text{dep}}) = \max_{\sigma,\rho} \Delta_T(\rho, \sigma; \mathcal{N}_{\text{dep}}) \tag{66}$$

$$= \frac{4}{3}p \cdot \max_{\rho,\sigma} T(\rho, \sigma) \tag{67}$$

$$= \frac{4}{3}p, \tag{68}$$

where ρ, σ are Haar-random states. For a noise strength of $p = 0.1$, this yields $\overline{\mathcal{D}}(\mathcal{N}_{\text{dep}}) \approx 0.133$, which coincides with the experimental predictions in figure 5(a).

Things are a bit more difficult for the average-case formulation. Here we first state and prove the following lemma that relates the average-case trace distance between pure Haar-random states solely to the dimension of the Hilbert space:

Lemma 1. *Let T be the trace distance and let $|\psi\rangle, |\phi\rangle$ be Haar-random states in a Hilbert space of dimension d. The average of trace distances between pairs of these states depends on d as*

$$\int_{|\psi\rangle} \int_{|\phi\rangle} T(|\psi\rangle, |\phi\rangle)\, d\nu(|\psi\rangle)\, d\nu(|\phi\rangle) = \frac{d-1}{d-\frac{1}{2}}. \tag{69}$$

Proof. We use the relation of the trace distance to the fidelity, which for pure quantum states reads

$$T(|\psi\rangle, |\phi\rangle) = \sqrt{1 - |\langle\psi|\phi\rangle|^2} \tag{70}$$

For independent Haar-random states, the squared overlap $F := |\langle\psi|\phi\rangle|^2$ follows a Beta distribution $B(1, d-1)$ [119], i.e. we have the probability density function

$$P(F) = (d-1)(1-F)^{d-2}. \tag{71}$$

Using this property, we finally get

$$\int_{|\psi\rangle} \int_{|\phi\rangle} T(|\psi\rangle, |\phi\rangle)\, d\nu(|\psi\rangle)\, d\nu(|\phi\rangle) = \int_0^1 \sqrt{1-F} \cdot P(F)\, dF \tag{72}$$

$$= (d-1) \int_0^1 (1-F)^{d-\frac{3}{2}}\, dF \tag{73}$$

$$= (d-1) \cdot B(1, d - \frac{1}{2}) \tag{74}$$

$$= \frac{d-1}{d-\frac{1}{2}}. \tag{75}$$

□

With the use of equations (64) and (65) and Lemma 1 for the single-qubit case, i.e. a Hilbert space of dimension $d = 2$, we can now continue:

$$\mathcal{D}(\Theta; \mathcal{N}_{\text{dep}}) = \int_\rho \int_\sigma \Delta_T(\rho, \sigma; \mathcal{N}_{\text{dep}})\, d\nu(\rho)\, d\nu(\sigma) \tag{76}$$

$$= \frac{4}{3}p \cdot \int_\rho \int_\sigma T(\rho, \sigma)\, d\nu(\rho)\, d\nu(\sigma) \tag{77}$$

$$= \frac{4}{3}p \cdot \frac{2}{3} \tag{78}$$

$$= \frac{8}{9}p \tag{79}$$

For a noise strength of $p = 0.1$, we get an average-case distinguishability loss of $\mathcal{D}(\mathcal{N}_{\text{dep}}) \approx 0.089$, which also matches the empirical result in figure 5(a).

B.2 Connection to Fidelity after Recovery

The central goal of our paper is to learn resource-efficient encoding operations $U_{\text{enc}}(\Theta)$ that protect quantum information against given noise channels $\mathcal{N}$. This ability is quantified by the worst-case distinguishability loss $\overline{\mathcal{D}}(\mathcal{N}; \Theta)$. However, to perform successful quantum error correction, one also has to construct and perform a recovery operation $U_{\text{rec}}(\Phi)$. How to learn a recovery operation we elaborate superficially in the main part of this paper, and discuss in more detail in appendix C. In the end, the measure of interest is how well the recovered (and decoded) state aligns with the original state, which we quantify by the worst-case fidelity loss $\overline{\mathcal{F}}(\mathcal{N}; \Theta, \Phi)$. In the empirical sections of this paper, we demonstrate for various noise models and setups that an encoding with lower distinguishability loss allows for a recovery operation with higher fidelity, i.e. lower fidelity loss. While it is not essential for the main statements of our paper, we think it is still valuable to derive a rigorous relation between these two quantities. Therefore, we state and prove the following theorem, which was also informally stated in the main part:

Theorem 1 (Upper bound on fidelity loss)**.** *Let $\mathcal{N}$ be a noise channel, for which $T(|\psi\rangle, \mathcal{N}(|\psi\rangle)) \leq \max_{|\phi\rangle} \{T(|\psi\rangle, |\phi\rangle) - T(\mathcal{N}(|\psi\rangle), \mathcal{N}(|\phi\rangle))\}$ holds for arbitrary pure states $|\psi\rangle$ (with $|\phi\rangle = |\psi\rangle_\perp$ one can see that this holds e.g. for arbitrary depolarizing and phase damping noise, or bit/phase-flip noise with strength $p \leq \frac{2}{3}$). Let furthermore U_{enc} be an encoding operation, and let ρ, σ be arbitrary pure quantum states. Then there always exists an recovery operation U_{rec}, for which the worst-case fidelity loss $\overline{\mathcal{F}}$ is upper-bounded by the worst-case distinguishability loss $\overline{\mathcal{D}}$ as:*

$$\overbrace{1 - \min_\rho F(\rho, U_{\text{enc}}^\dagger \circ U_{\text{rec}} \circ \mathcal{N} \circ U_{\text{enc}}(\rho))}^{\overline{\mathcal{F}}(\mathcal{N})} \leq 1 - (1 - \overbrace{\max_{\rho,\sigma}(T(\rho, \sigma) - T(\mathcal{N} \circ U_{\text{enc}}(\rho), \mathcal{N} \circ U_{\text{enc}}(\sigma)))}^{\overline{\mathcal{D}}(\mathcal{N})})^2 \tag{80}$$

To maintain clarity in the notation, we do not explicitly denote partial traces. Operations involving the tracing out of certain subsystems (e.g. the recovery qubits) are understood implicitly.

Proof. We start with a lower bound on the fidelity given by the Fuchs-van de Graaf inequality [36] for arbitrary states ρ, σ:

$$1 - \sqrt{F(\rho, U_{\text{enc}}^\dagger \circ U_{\text{rec}} \circ \mathcal{N} \circ U_{\text{enc}}(\rho))} \leq T(\rho, U_{\text{enc}}^\dagger \circ U_{\text{rec}} \circ \mathcal{N} \circ U_{\text{enc}}(\rho)) \tag{81}$$

We now rearrange the terms and use the invariance of the trace distance w.r.t. unitary operations:

$$\sqrt{F(\rho, U_{\text{enc}}^\dagger \circ U_{\text{rec}} \circ \mathcal{N} \circ U_{\text{enc}}(\rho))} \geq 1 - T(\rho, U_{\text{enc}}^\dagger \circ U_{\text{rec}} \circ \mathcal{N} \circ U_{\text{enc}}(\rho)) \tag{82}$$

$$= 1 - T(U_{\text{enc}}(\rho), U_{\text{enc}} \circ U_{\text{enc}}^\dagger \circ U_{\text{rec}} \circ \mathcal{N} \circ U_{\text{enc}}(\rho)) \tag{83}$$

$$= 1 - T(U_{\text{enc}}(\rho), U_{\text{rec}} \circ \mathcal{N} \circ U_{\text{enc}}(\rho)) \tag{84}$$

With the existence of a trivial recovery operation $U_{\text{rec}} = \mathbb{I}$, we can further simplify, use the above assumption on the error channel $\mathcal{N}$, and again employ the invariance of the trace distance:

$$\sqrt{F(\rho, U_{\text{enc}}^\dagger \circ U_{\text{rec}} \circ \mathcal{N} \circ U_{\text{enc}}(\rho))} \geq 1 - T(U_{\text{enc}}(\rho), \mathcal{N} \circ U_{\text{enc}}(\rho)) \tag{85}$$

$$\geq 1 - \max_\sigma \left(T(U_{\text{enc}}(\rho), U_{\text{enc}}(\sigma)) - T(\mathcal{N} \circ U_{\text{enc}}(\rho), \mathcal{N} \circ U_{\text{enc}}(\sigma)\right) \tag{86}$$

$$= 1 - \max_\sigma \left(T(\rho, \sigma) - T(\mathcal{N} \circ U_{\text{enc}}(\rho), \mathcal{N} \circ U_{\text{enc}}(\sigma)\right) \tag{87}$$

Finally, as this statement holds for arbitrary pure ρ, we can also state it in the worst-case formulation and rearrange terms:

$$\min_{\rho} \sqrt{F(\rho, U_{\text{enc}}^{\dagger} \circ U_{\text{rec}} \circ \mathcal{N} \circ U_{\text{enc}}(\rho))} \geq \min_{\rho} \left(1 - \max_{\sigma} \left(T(\rho, \sigma) - T(\mathcal{N} \circ U_{\text{enc}}(\rho), \mathcal{N} \circ U_{\text{enc}}(\sigma))\right)\right) \tag{88}$$

$$= 1 - \max_{\rho,\sigma} \left(T(\rho, \sigma) - T(\mathcal{N} \circ U_{\text{enc}}(\rho), \mathcal{N} \circ U_{\text{enc}}(\sigma))\right) \tag{89}$$

Utilizing that both left and right sides of the equation can only take values in $[0, 1]$, we just need to take the square and subtract both sides from one (which inverts the inequality) to arrive at the desired outcome. □

In simpler words, Theorem 1 states that decreasing the distinguishability loss for an encoding operation guarantees a lower fidelity loss, i.e. an improved fidelity after recovery. In practice, this bound is rarely tight, as this relation holds already purely due to the existence of a trivial recovery operation $U_{\text{rec}} = \mathbb{I}$, as used in the proof. Therefore, usually it should be possible to find much better recovery operations than guaranteed by this Theorem 1. The experimental results in this paper, generated with the procedure for learning recovery operations described in appendix C, confirm this assumption. However, we also empirically observe that a lower distinguishability loss allows for a higher-fidelity recovery operation.

Under the same requirements and using a similar proof strategy, one can also derive a lower bound on the fidelity, loss depending on the distinguishability loss, which informally reads as:

Theorem 2 (Lower bound on fidelity loss, informal)**.** *The worst-case distinguishability loss $\overline{\mathcal{D}}$ under a well-behaved noise channel $\mathcal{N}$ bounds any recovery operation to achieve a worst-case fidelity loss of at least*

$$\overline{\mathcal{F}}(\mathcal{N}) \geq \overline{\mathcal{D}}(\mathcal{N})^2. \tag{90}$$

Consequently, a lower distinguishability loss allows for a lower fidelity loss, meaning a higher-fidelity recovery operation.

Complementary to the above, Theorem 2 states that it is not only sufficient but also necessary to achieve a low distinguishability loss, to allow for a high-fidelity recovery operation. However, especially for small $\overline{\mathcal{D}}$, this bound is close to 1, i.e. almost trivial.

Overall, both theorems establish an interesting analytic connection between the objective of minimizing the distinguishability loss, and minimizing the fidelity loss, i.e. achieving a high fidelity after recovery. Combined with the empirical evaluations and correlations we highlight throughout the paper, we are confident that our proposed procedure has its merits for quantum error correction.

B.3 Code Distance and Approximate Error Correction

We recall from the literature [39] that an error on an n-qubit system can be expressed as a tensor product of single-qubit Pauli operators

$$E = E_1 \otimes E_2 \otimes \cdots \otimes E_n, \tag{91}$$

where each E_j is from $\{I, X, Y, Z\}$. The weight of an error operator $wt(E)$ is defined as the number of qubits on which E acts non-trivially, i.e.

$$wt(E) = |\{j \mid E_j \neq I\}|. \tag{92}$$

It is easy to see that the number of errors of weight w is given by

$$N_w = \binom{n}{w} \cdot 3^w, \tag{93}$$

where the first factor represents the number of unique configurations of w qubits on which errors occur, and the second factor expresses the fact that 3 non-identity Pauli errors can occur on each of these qubits. The distance d of a code can be defined as the minimum weight of a non-trivial error term that transforms one valid codeword into another one. More formally, assume that a code can

detect all weight-w errors, but can not detect all errors with $wt(E) = w + 1$. Then this code has a code distance of

$$d = w + 1, \tag{94}$$

which by definition allows it to detect $d - 1 = w$ errors and correct for

$$t = \lfloor \frac{d-1}{2} \rfloor = \lfloor \frac{w}{2} \rfloor \tag{95}$$

errors. With the number of encoded logical qubits k and the underlying number of physical qubits n, one typically uses the description

$$((n, 2^k, d)), \tag{96}$$

or $[[n, k, d]]$ for stabilizer codes, to classify the error correction capabilities of a code. In this work, we consider QEC codes with $n \leq 10$, $k \leq 2$, and $d \leq 4$, but in the main part, we also sketch potential improvements that could allow scaling to larger code parameters.

For some QEC codes, in particular stabilizer codes, there exist analytic but also numerical techniques to determine the code distance d for a given encoding [18, 84, 100]. However, these results can not be directly utilized to determine the distance of VarQEC codes. Therefore, we introduce the notion of the *potential code distance* d^*, which can be determined purely based on the distinguishability loss:

Definition 1 (Potential code distance)**.** *Let $\mathcal{C}$ be a QEC code that encodes a k-qubit logical state into n physical qubits. Assume that the distinguishability loss of this code satisfies*

$$\overline{\mathcal{D}}_{\mathcal{S}}(\mathcal{N}_p) = 0 \tag{97}$$

for all noise strengths $0 \leq p \leq 1$ and all Pauli noise channels

$$\mathcal{N}_p(\rho) = (1-p) \cdot \rho + p \cdot E\rho E^\dagger, \tag{98}$$

where $wt(E) \leq w$. Furthermore, assume there is at least one noise channel $\mathcal{N}_p$ with $wt(E) = w + 1$ for which $\overline{\mathcal{D}}_{\mathcal{S}}(\mathcal{N}_p) > 0$. Then we say that $\mathcal{C}$ has a potential code distance of $d^* := w + 1$, which lets us describe the code with the parameters

$$((n, 2^k, d^*)). \tag{99}$$

In the case of Definition 1, it would also be possible to alternatively use the average-case code distinguishability loss $\mathcal{D}_{\mathcal{S}}$ instead of the worst-case formulation $\overline{\mathcal{D}}_{\mathcal{S}}$. We observed that in all cases the *strongest signal* $\overline{\mathcal{D}}_{\mathcal{S}}(\mathcal{N}_p)$ is exhibited for $p = 0.5$, i.e. for empirical evaluations we focus on this setup.

Especially given the VarQEC codes, we also define a relaxed version of the potential code distance, which we dub the *potential approximate code distance* d^*_ε:

Definition 2 (Potential approximate code distance)**.** *Let $\mathcal{C}$ be an approximate quantum error correction code encoding a k-qubit logical state into n physical qubits. Assume that the distinguishability loss of this code satisfies*

$$\overline{\mathcal{D}}_{\mathcal{S}}(\mathcal{N}_p) \leq \varepsilon \tag{100}$$

for a small positive value of ε, all noise strengths $0 \leq p \leq 1$ and all Pauli noise channels

$$\mathcal{N}_p(\rho) = (1-p) \cdot \rho + p \cdot E\rho E^\dagger, \tag{101}$$

where $wt(E) \leq w$. Furthermore, assume there is at least one noise channel $\mathcal{N}_p$ with $wt(E) = w + 1$ for which $\overline{\mathcal{D}}_{\mathcal{S}}(\mathcal{N}_p) > \varepsilon$. Then we say that $\mathcal{C}$ has a potential approximate code distance of $d^*_\varepsilon := w + 1$, which lets us describe the code with the parameters

$$((n, 2^k, d^*_\varepsilon)). \tag{102}$$

Based on these definitions, we report empirical evaluations of several standard QEC codes, and two instances of VarQEC codes in table 2. In particular, we determine the potential code distance following Definition 1 for standard (non-approximative) codes with known code distance, and the

	1 fault		2 faults		3 faults		4 faults	
	number	detect	number	detect	number	detect	number	detect
$[[3,1,1]]$	9	✗						
$[[4,1,2]]$	12	✓	54	✗				
$((4,2))^a$		(✓)		✗				
$[[5,1,3]]$	15	✓	90	✓	270	✗		
$((5,2))^b$		(✓)		(✓)		✗		
$[[7,1,3]]$	21	✓	189	✓	945	✗		
$((7,2))^b$		(✓)		(✓)		✗		
$[[9,1,3]]$	27	✓	324	✓	2268	✗		
$[[10,1,4]]$	30	✓	405	✓	3240	✓	17010	✗

^{a} trained on amplitude damping noise with $\gamma = 0.1$; ^{b} trained on depolarizing noise with $p = 0.1$;

Table 2. Evaluation of potential (approximative) code distance following Definitions 1 and 2 for different QEC and VarQEC codes. We perform evaluations for 1 to 4 faults, corresponding to the respective error weights in equation (92). The *number* column denotes the according count of possible error configurations from equation (93) that are evaluated. A checkmark ✓ for *detect* indicates that equation (97) is satisfied for this code and error weight, for (✓) at least the weaker equation (100) holds with $\varepsilon = 0.002$. For ✗ neither holds, which also indicates the potential (approximative) code distance of the respective code.

potential approximate code distance for codes learned on depolarizing and amplitude damping noise.

For all codes with known code distance d, this value perfectly aligns with the evaluated potential code distance d^*. Therefore, we conjecture but do not formally prove in this work that the potential code distance is equivalent to the actual code distance, i.e.

$$((n, 2^k, d^*)) = ((n, 2^k, d)). \tag{103}$$

Based on this, it directly follows that the respective code can perfectly correct for $\lfloor \frac{d^*-1}{2} \rfloor$ errors, i.e. it exits a recovery operation for which

$$\overline{\mathcal{F}}(\mathcal{N}_p) = 1 \tag{104}$$

for all noise channels $\mathcal{N}_p(\rho) = (1-p) \cdot \rho + p \cdot E\rho E^\dagger$ where E has a weight of $w \leq \lfloor \frac{d^*-1}{2} \rfloor$. We note that the results from Theorems 1 and 2 are not applicable here, as these noise channels do not satisfy the stated requirements.

Alternatively to this framework of *perfect* error correction, there is also the notion of *approximate* error correction [10, 90], which relaxes equation (104) to

$$\overline{\mathcal{F}}(\mathcal{N}_p) \geq 1 - \delta \tag{105}$$

for some small positive value δ. For completeness, we notice that both perfect and approximate error correction conditions can also be stated in terms of the *Knill-Laflamme* conditions [55], but the notion using the fidelity is easier to interpret for our work. By construction, the proposed VarQEC procedure does not explicitly enforce the ability to recover information under specific error terms. Rather, the distinguishability loss is used to automatically focus on specific error terms, to minimize the overall loss of information. Consequently, approximate error correction is the more fitting framework to analyze these codes. Similar to above, we hypothesize that a VarQEC code with parameters $((n, 2^k, d^*_\varepsilon))$ allows for the correction of up to $\lfloor \frac{d^*_\varepsilon-1}{2} \rfloor$ with a high fidelity following equation (105), where δ correlates with ε. Interestingly, the $((5,2))$ VarQEC code that is analyzed in figure 7(a) practically performs equivalent to the $[[5,1,3]]$ QEC code, i.e. we can assume δ being very close to 0, or at least below numerical accuracy of the evaluation procedure. Consequently, it is reasonable to interpret this instance of a VarQEC-code as being capable of performing practically exact error correction.

B.4 Approximation with Two-Designs

To allow for an efficient evaluation of both the average-case distinguishability loss $\mathcal{D}$ and worst-case distinguishability loss $\overline{\mathcal{D}}$, we introduced two-design approximations $\mathcal{D}_\mathcal{S}$ and $\overline{\mathcal{D}}_\mathcal{S}$, respectively. For the exact definitions, please refer to the main part or equations (53), (54), (56) and (57) in the appendix. The non-approximative instances are based on integrating or maximizing over pairs of Haar-random pure k-qubit states [96], respectively. Empirically, these operations have to be mimicked by averaging or maximizing over a finite set of H states following a Haar-random distribution.

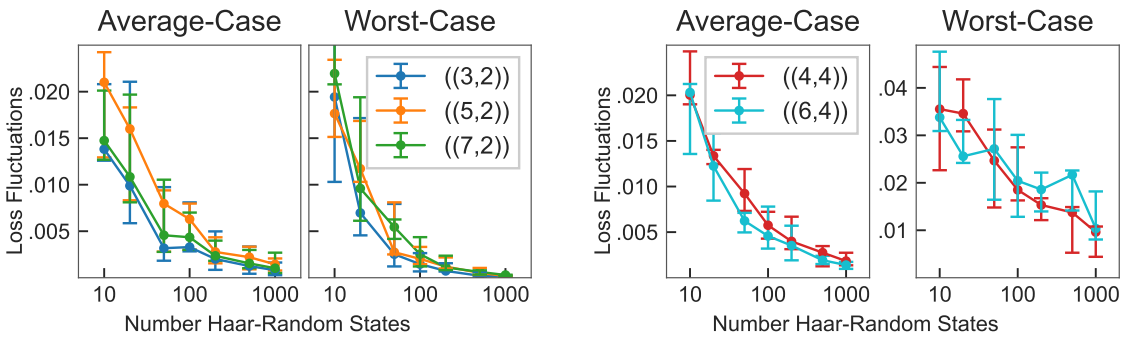

(a) Analysis for a single data qubit, i.e. $k = 1$.

(b) Analysis for two data qubits, i.e. $k = 2$.

Figure 9. Empirical analysis of how many Haar-random states are necessary to get a stable approximation of the ground-truth loss, which integrates or maximizes over an infinite number of states. The loss fluctuations denote the maximal difference between distinguishability loss values over 10 instances of the same encoding, with different random seeds for generating the Haar-random states. The data points denote the median, while the error bars show the smallest/largest fluctuation over 5 different encoding circuits. The plots refer to depolarizing noise with $p = 0.1$, but similar results can be obtained for other noise models.

In figure 9, we analyze how many such states are actually necessary for $k = 1$ and $k = 2$ to get a stable approximation to the ground-truth. In the main parts of this paper, we base our evaluations on $H = 1000$ Haar-random states, which should guarantee a deviation from the ground truth of at most 0.001 in the $k = 1$ case and 0.01 for $k = 2$. To save computational resources, in the appendix we reduce this to $H = 200$, which still should limit the deviations to about 0.005.

Formally, one defines that $\mathcal{X}$ forms a quantum t-design, if the following equation holds for any polynomial P_t of a most degree t in the entries of ρ, as well as most degree t in the complex conjugate of these entries [6]:

$$\frac{1}{S} \sum_{\rho_k \in \mathcal{X}} P_t(\rho_k) = \int_{\rho} P_t(\rho)\, d\nu(\rho) \tag{106}$$

On the right side of equation (106), ρ are Haar-random quantum states. In principle, the distinguishability loss contains degrees of up to order 4, i.e. one would require a 4-design to guarantee this equivalence. However, we evaluate below that in practice, using a two-design, which is much easier to construct and evaluate, allows for a sufficiently accurate approximation.

In general, the minimum size of a two-design for a k-qubit system is $\dim(\mathcal{H}^{\otimes k})^2 = 4^k$. One trivial two-design, which is, however, vastly exceeding this bound, is given by the Clifford group [30]. For a single-qubit system, this would allow for a two-design with four elements, i.e., the *tetrahedron states*. However, for easier preparation of the initial states, we resort to the more common six-element spherical two-design

$$\mathcal{S} = \{|0\rangle, |1\rangle, |+\rangle, |-\rangle, |+i\rangle, |-i\rangle\}. \tag{107}$$

This spherical two-design originating from a single qubit is also visualized in figure 2(c). For two data qubit, i.e. $k = 2$, we use a formulation with 12 product states and 4 entangled states, reading as

$$\begin{aligned}
\mathcal{S} = \{&|00\rangle, |01\rangle, |10\rangle, |11\rangle, && (108)\\
&|++\rangle, |+-\rangle, |-+\rangle, |--\rangle, && (109)\\
&|+i+i\rangle, |+i-i\rangle, |-i+i\rangle, |-i-i\rangle, && (110)\\
&|00\rangle + |11\rangle, |00\rangle - |11\rangle, |01\rangle + |10\rangle, |01\rangle - |10\rangle\}, && (111)
\end{aligned}$$

where the normalization factors for the entangled states are understood implicitly. We acknowledge that this approximation still is untractable for large k, especially as we evaluate trace distance between all states in $\mathcal{S}$, which consequently scales as $(4^k)^2 = 8^k$. However, we want to emphasize that, in general, it is not desirable to encode an arbitrary number of logical qubits in a single code patch. We envision a modular realization, where several code patches, each implementing a limited number of logical qubits k, interact. An extreme example of this from existing QEC literature would be the use of lattice surgery [47] on logical surface code patches [35], each encoding only a single logical qubit.

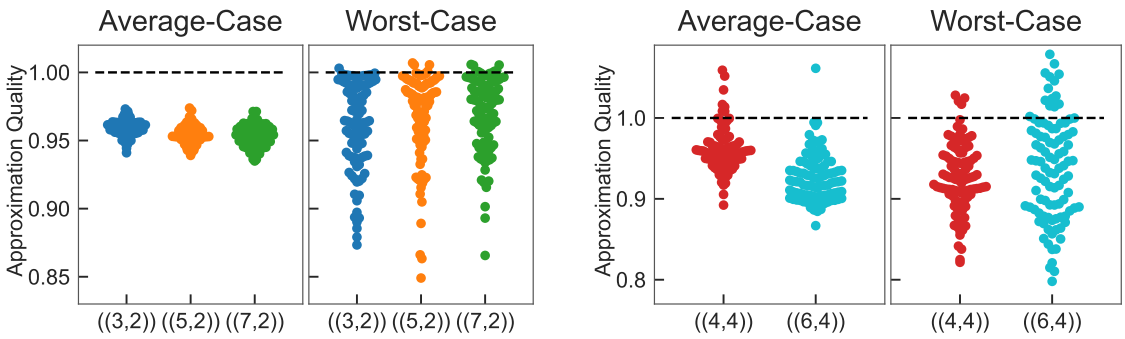

(a) Analysis for a single data qubit, i.e. $k = 1$.

(b) Analysis for two data qubits, i.e. $k = 2$.

Figure 10. Empirical analysis on how well the two-design formulations approximate the groundtruth of the distinguishability loss, which we quantify by $\mathcal{D}/\mathcal{D}_{\mathcal{S}}$ and $\overline{\mathcal{D}}/\overline{\mathcal{D}}_{\mathcal{S}}$, respectively. Hereby, we evaluate 100 random encoding circuit instances for each setup, and estimate the ground truth with $H = 200$ Haar-random states. The plots refer to a depolarizing noise channel with $p = 0.1$.

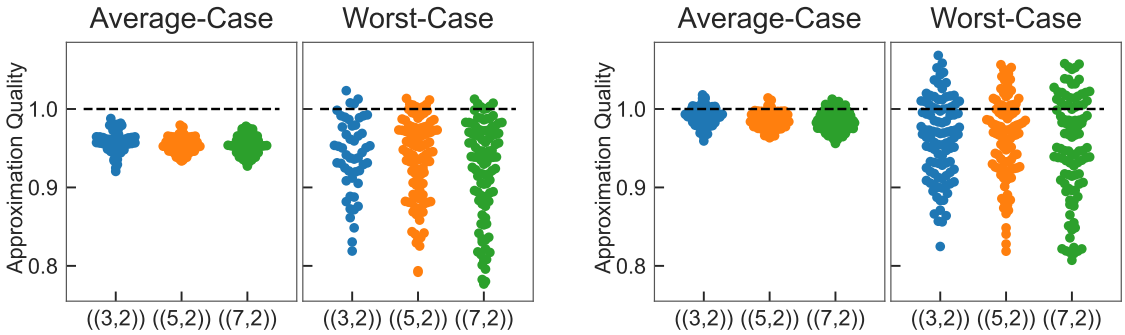

(a) Approximation with standard 2-design.

(b) Approximation with weighted 2-design.

Figure 11. Empirical analysis on how a weighted two-design can reduce the approximation bias, compared to a standard two-design on an amplitude damping channel with $\gamma = 0.1$. Hereby, we evaluate 100 random encoding circuit instances for each setup, and estimate the ground truth with $H = 200$ Haar-random states. the weights are set as summarized in equation (115).

In figure 10, we analyze how well we can approximate the ground-truth distinguishability loss with the respective two-design formulations. By the definitions, it must, in principle, hold

$$\overline{\mathcal{D}} \geq \overline{\mathcal{D}}_{\mathcal{S}}. \tag{112}$$

This is because the state pair creating the largest loss of trace distance within the two-design must trivially be reflected in the consideration of all state pairs. For the average-case formulation, no such direct relation exists. Empirically, we quantify the approximation quality as $\mathcal{D}/\mathcal{D}_{\mathcal{S}}$ and $\overline{\mathcal{D}}/\overline{\mathcal{D}}_{\mathcal{S}}$, respectively. For both the $k = 1$ setup in figure 10(a) and the $k = 2$ setup in figure 10(b), we can see that while there is some bias in average-case approximation, the variance of results is not too large. In contrast, for the worst-case approximation, the bias is smaller, but the variance is larger. The points above 1.0, which in principle violate equation (112), can be explained by the fact that the baseline is only estimated with a finite number of Haar-random states. Moreover, we do not need to care too much about the worst-case approximation quality, as for evaluating this loss we usually directly resort to $\overline{\mathcal{D}}$ instead of $\overline{\mathcal{D}}_{\mathcal{S}}$. For training, we employ the average-case approximation $\mathcal{D}_{\mathcal{S}}$, but as it is used as a trainable loss function, the approximate proportionality to the ground truth $\mathcal{D}$ is sufficient.

While not strictly necessary, there are also ways to reduce the bias, especially of the average-case formulation, without significantly reducing the variance. One possibility we briefly consider here is the use of a *weighted two-design* [88], which incorporates prior information about the noise channel. For this, we can extend the definitions of the distinguishability loss as

$$\mathcal{D}_{\mathcal{S}_w}(\mathcal{N};\Theta) = \frac{1}{\sum_{\rho,\sigma\in\mathcal{S}_w} w_\rho \cdot w_\sigma} \sum_{\rho,\sigma\in\mathcal{S}} w_\rho \cdot w_\sigma \cdot (T(\rho,\sigma) - T(\mathcal{N}(\rho_L),\mathcal{N}(\sigma_L))) \tag{113}$$

$$\overline{\mathcal{D}}_{\mathcal{S}_w}(\mathcal{N};\Theta) = \max_{\rho,\sigma\in\mathcal{S}} w_\rho \cdot w_\sigma \cdot (T(\rho,\sigma) - T(\mathcal{N}(\rho_L),\mathcal{N}(\sigma_L)))\,, \tag{114}$$

where the w's are weights associated with the respective elements of the two-design. It is natural but not necessary to ensure that it holds $w_\rho \geq 0$ for all elements ρ and $\sum_{\rho\in\mathcal{S}} w_\rho = |\mathcal{S}|$. With setting all $w_\rho = 1$ the equations simplify to the original definitions,

In figure 11 we exemplarily consider an amplitude damping channel with damping parameter $\gamma = 0.1$. With this channel, low-energy states like $|0\rangle$ are less or not affected at all, while high-energy states like $|1\rangle$ are disproportionally strongly affected. We reflect this in setting the weights as

$$w_{|0\rangle} = 0.95,\ w_{|1\rangle} = 1.05,\ w_{|+\rangle} = 1.0,\ w_{|-\rangle} = 1.0,\ w_{|+i\rangle} = 1.0,\ w_{|-i\rangle} = 1.0. \tag{115}$$

The comparison between the pure two-design and the weighted two-design formulation underlines that this reduces the bias of the average-case distinguishability loss, without increasing the variance.

Appendix C: Learning Recovery Operations with Fidelity Loss

In this appendix, we sketch a procedure with which one can learn a recovery operation, given a VarQEC-encoding already trained with the distinguishability loss. We emphasize that deriving such a recovery operation is not the primary scope of this work, but acknowledge that it is still helpful to consider and evaluate our technique within the scope of error correction. Therefore, the technique we describe in the following is to a large extent based on the work by Johnson et al. [50]. There, the authors establish the QVECTOR approach, which can be used to train encoding and recovery operations for a given noise channel simultaneously from scratch, based on evaluations of the fidelity. We neither claim that this is the only method that could be modified to learn recovery operations given fixed encodings, nor do we claim that it is the most sophisticated technique for this task. Still, empirically, we get convincing results, and we outperform the original QVECTOR approach in a variety of setups.

To set the state, let us start with the definition of an encoded state ρ_L encoded with the potentially parameterized encoding operation $U_{\text{enc}}(\Theta)$ as described in equation (55). After a noise channel $\mathcal{N}$ acts on this state, the task is now to find a recovery operation $U_{\text{rec}}(\Phi)$, which reverts the effect of $\mathcal{N}$ as much as possible. Especially for the multi-recovery setting, i.e. multiple consecutive recovery operations, this requires the use of additional *recovery* qubits initialized to a known state, usually $|0\rangle^{\otimes r}$. Most established QEC procedures use this register for measuring stabilizers and extracting syndromes [38]. Subsequently, classically controlled correction operations are applied to the encoded states. While it should be possible to adapt the presented VarQEC routine within this framework, it more naturally aligns with the concept of *measurement-free* or *autonomous* QEC [45, 58, 116]. After applying the recovery operation, the register is traced out, which in practice could be done by re-initializing to $|0\rangle^{\otimes r}$ or supplying new qubits for the next recovery cycle. Considering the single-recovery setup, the resulting state $\hat{\rho}_L$ reads as

$$\hat{\rho}_L = \text{Tr}_r \left(U_{\text{rec}}(\Phi) \left(\mathcal{N}(\rho_L) \otimes |0\rangle \langle 0|^{\otimes r} \right) U^\dagger_{\text{rec}}(\Phi) \right) \tag{116}$$

Consecutively, one can decode the state using the inverse of the encoding operation $U^\dagger_{\text{enc}}(\Theta)$ and trace out the ancilla encoding qubits to get the final decodes state $\hat{\rho}$ as

$$\hat{\rho} = \text{Tr}_{n-k} \left(U^\dagger_{\text{enc}}(\Theta) \hat{\rho}_L U_{\text{enc}}(\Theta) \right), \tag{117}$$

where ρ should be close to $\hat{\rho}$ for a successful QEC cycle. This closeness can be quantified by the fidelity $F(\rho, \hat{\rho})$. This is the underlying idea of the QVECTOR approach, which uses variational ansätze for both the encoding and recovery operation, and defines the average-case *fidelity loss* as

$$\mathcal{F}(\mathcal{N}; \Theta, \Phi) = 1 - \int_\rho F(\rho, \hat{\rho})\, d\nu(\rho), \tag{118}$$

where the states ρ follow a Haar-random distribution. Similarly to the distinguishability loss, one can also define a worst-case version, which reads as

$$\overline{\mathcal{F}}(\mathcal{N}; \Theta, \Phi) = 1 - \min_\rho F(\rho, \hat{\rho}). \tag{119}$$

We note that the original paper [50] defines a slightly different formulation, in which the encoding qubits are not traced out, i.e. the underlying fidelity is

$$F(p \otimes |0\rangle^{n-k}, U^\dagger_{\text{enc}}(\Theta) \hat{\rho}_L U_{\text{enc}}(\Theta)). \tag{120}$$

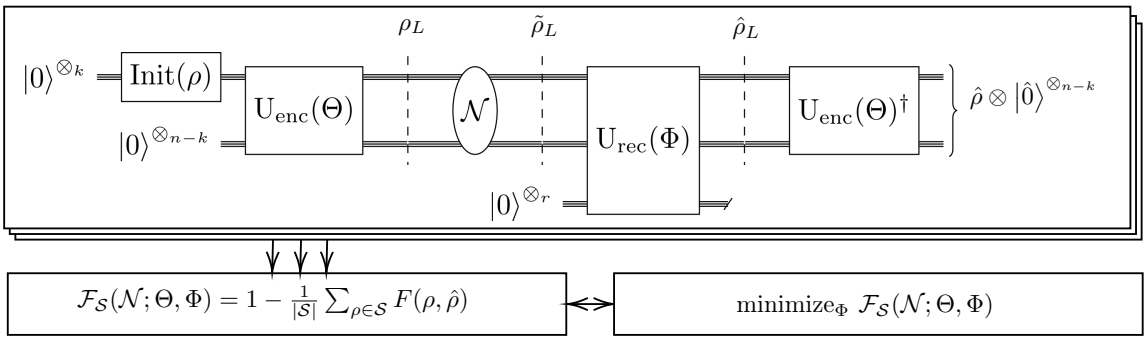

Figure 12. The adapted QVECTOR pipeline [50] for training recovery operations $U_{\mathrm{rec}}(\Phi)$, under the premise that the encoding operations $U_{\mathrm{enc}}(\Theta)$ have already been trained with the distinguishability loss. The average-case fidelity loss $\mathcal{F}_{\mathcal{S}}$ is evaluated on states from a two-design $\mathcal{S}$ and is minimized w.r.t. the free parameters of the recovery operation. We note that at the end of the circuits it is not guaranteed that the state $\hat{\rho}$ on the k data qubits is completely disentangled from the $n-k$ ancilla qubits, but for the single-recovery scenario, this can be neglected.

However, this formulation is mainly motivated by the multi-recovery scenario, which we, for now, do not focus on in our work. Indeed, we experimented with both loss functions and did not observe a significant difference in performance for our setup. As the fidelity distance contains moments of at most order two, the two design formulations of the average-case loss are exact in this case:

$$\mathcal{F}_{\mathcal{S}}(\mathcal{N};\Theta,\Phi) = 1 - \frac{1}{|\mathcal{S}|}\sum_{\rho\in\mathcal{S}} F(\rho,\hat{\rho}) = \mathcal{F}(\mathcal{N};\Theta,\Phi) \tag{121}$$

The fidelity loss trivially converges to 0 if the fidelity between original and recovered state is close to 1, i.e. one can formulate and optimize the QVECTOR objective as

$$\min_{\Theta,\Phi} \mathcal{F}_{\mathcal{S}}(\mathcal{N};\Theta,\Phi), \tag{122}$$

which is used to simultaneously train encoding $U_{\mathrm{enc}}(\Theta)$ and recovery $U_{\mathrm{rec}}(\Phi)$. We slightly modify this setup, as initially we use our VarQEC procedure based on the distinguishability loss to produce sophisticated encodings. The respective encoding ansätze are fixed after that, and we only train the recovery operation with the fidelity loss, which simplifies the second step to

$$\min_{\Phi} \mathcal{F}_{\mathcal{S}}(\Theta,\Phi). \tag{123}$$

This procedure is also sketched in figure 12. The end-to-end QVECTOR approach proves sophisticated enough for noise models like phase and amplitude damping with small damping parameters [50]. However, it struggles with more complex noise models and larger noise rates. In the experimental section of this paper, we demonstrate that our two-step procedure succeeds on a variety of noise models and does so with a much shallower circuit, which is beneficial for fault-resilience and fault-tolerance.

Appendix D: Implementation Details and Setup

In this appendix, we summarize details regarding the actual experimental realization and implementation. We introduce a new type of ansatz we used for both the encoding and recovery operations in appendix D.1. In appendix D.2 we highlight some implementation details and also discuss some algorithmic hyperparameters.

D.1 Randomized Entangling Ansätze

In principle, the introduced VarQEC procedure also allows for generating circuit ansätze from scratch. This could, e.g. be done by using the distinguishability loss as the reward function of a reinforcement learning agent [34, 77], or encoding it into the fitness function of an evolutionary algorithm [89, 99]. However, for the proof-of-concept considerations of this paper, for simplicity we decided to formulate it as a variational quantum algorithm [20] by fixing the structure U_{enc} and U_{rec} as a variational quantum circuit and purely training variational parameters which corresponds to rotation angles. To still have some flexibility and adaptability of the respective ansätze, we define

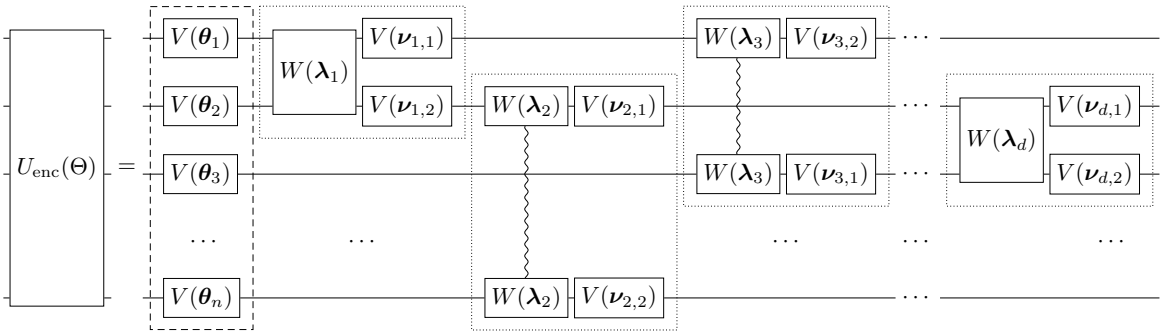

Figure 13. An instance of the REA on n qubits. It consists of an initial block of parameterized single-qubit gates V and d blocks of successive entangling operations. The entangling blocks themselves consist of an optionally parametrized two-qubit gate W, and parameterized single-qubit operations V on the two involved qubits. The control and target for each two-qubit block are determined uniformly at random, i.e. the exact instance of an ansatz is defined by the random seed that was used for generating it.

the randomized entangling ansatz (REA). It is inspired by the simplified two-design ansatz [22], which incorporates single-qubit rotations and two-qubit control gates, but offers more flexibility.

In figure 13 we show an instance of such a REA ansatz for the encoding operation. We note that the same ansatz can also be used for the recovery operations, potentially incorporating the additional recovery register. The general outline is defined by a parameterized single-qubit operation V and an optionally also parameterized two-qubit operation W. Throughout this paper, we default to

$$V(\boldsymbol{\theta_j}) = R_z(\theta_{j,3})R_y(\theta_{j,2})R_z(\theta_{j,1}) \tag{124}$$

$$W(\boldsymbol{\lambda}_j) = \text{Controlled}-V(\boldsymbol{\lambda}_j) \tag{125}$$

to stay as general as possible. However, to adapt to the native gate sets of the systems, we deviate from this in the hardware experiments. The details are laid out in the respective sections. The construction itself first places single-qubit operations parameterized by $\boldsymbol{\theta}$ on each contributing qubit. Subsequently, d two-qubit blocks are placed, where control and target are each selected uniformly at random, but disjunct. These gates do not necessarily have to be parameterized, but in case they are, we refer to the parameters as $\boldsymbol{\lambda}$. After each of these blocks, we place two single-qubit operations parametrized by $\boldsymbol{\nu}$ on the involved qubits.

As the placement of two-qubit blocks is determined at random, the actual instance is determined by the random seed that was used for generating the placement. To generate a sophisticated ansatz, in particular a shallow one, throughout this paper, we use 100 different seeds, train the respective VarQEC circuit, and select the best performing one. We acknowledge that this procedure can not be expected to scale beyond a certain system size, as the number of ansätze one has to iterate over might increase proportionally to the problem complexity. However, we think it suffices as a proof-of-concept procedure to demonstrate that effective and shallow-depth encoding circuits can be found with the VarQEC procedure. In particular, the parameter count is given as

$$|\boldsymbol{\theta}| = n \cdot N_V \tag{126}$$

$$|\boldsymbol{\lambda}| = d \cdot N_W \tag{127}$$

$$|\boldsymbol{\nu}| = 2 \cdot d \cdot N_V \tag{128}$$

where N_V and N_W are the number of parameters per single-qubit and two-qubit operation, respectively. Alternative ways to perform architecture search in future work have already been outlined above, but one can also employ additional techniques from the literature, like e.g. differentiable architecture search [117] or incremental growing the ansatz [40].

D.2 Hyperparameters and Python Module

First, we want to note that all details on the used hyperparameters and settings can be extracted from the provided implementation and respective Readme file; links are provided in the data availability statement. In this section, we therefore only focus on the high-level functionalities and highlight the most important implementation details.

We implemented the `VarQEC` pipeline in `python v3.12`, but it should also be backward compatible with `python v3.10`. The underlying framework consists of about 4000 lines of code and

$\|0\rangle$	$\|1\rangle$	$\|+\rangle$	$\|-\rangle$	$\|+i\rangle$	$\|-i\rangle$
$U_3(0.0, 0.0, 0.0)$	$U_3(\pi, 0.0, \pi)$	$U_3(\frac{\pi}{2}, 0.0, \pi)$	$U_3(\frac{\pi}{2}, -\pi, -\pi)$	$U_3(\frac{\pi}{2}, \frac{\pi}{2}, -\pi)$	$U_3(\frac{\pi}{2}, -\frac{\pi}{2}, -\pi)$

Table 3. How to perform parameterized initialization on single-qubit two-design states. We place an arbitrary rotation gate $U_3(\theta, \phi, \delta)$ on the date qubit, which with the denoted parameters prepares the respective states. This procedure allows for batch-processing of all states involved in the computation of the loss function, which significantly speeds up the training procedure.

is embedded into the `PyTorch` cosmos [81] for training machine learning models. To realize the quantum computing parts, for initial proof-of-concept realizations and hyperparameter tuning, we resorted to the `qiskittorchmodule` [71]. For later experiments and the polished version, we switched to `PennyLane` [11], due to the more extensive support of simulating mixed states and quantum channels. The `VarQEC` module itself consists of 7 main components, which we will briefly describe in the following:

Training and testing script. This is the central component of the `VarQEC` pipeline and integrates all other components. It imports the respective models, circuit ansätze, error channels, and loss functions. It currently makes use of the L-BFGS optimizer [63] with a history size of 100 and 10 iterations per training epoch, but can easily be adapted to support other optimizer instances. The training script allows for the isolated training of encoding operations with the distinguishability loss, but also supports the successive training of recovery operations with the fidelity loss. The testing script allows to perform a detailed analysis of the trained models, but also implements several known error correction codes as a baseline. Furthermore, it also allows to evaluate the potential code distance introduced in appendix B.3.

Loss functions. These are one of the main contributions of this paper, and are therefore implemented in a modular function, to enable usage also in other setups. For the fidelity loss, we only provide a simplified implementation based on the QVECTOR approach, as described in appendix C. For the distinguishability loss, we provide two separately finetuned versions, one to reduce memory overhead on the expense of additional time, and one that is adapted the other way around.

Variational Models. These machine learning models represent either pure encoding circuits or also contain consecutive recovery operations. The implementation offers flexibility regarding model width, i.e. the use of data, ancilla, and recovery qubits, but also model depth, i.e. the number of involved trainable parameters. It imports the three components of state encoding, trainable circuit ansatz, and error channels. All computations are implemented in a fully differentiable way utilizing the `autograd` [81] method, which allows for straightforward training with gradient-based optimizers.

State Encoding. We provide two different methods to prepare the initial states, corresponding to the exact and approximate formulation of the respective loss functions. The first one initializes an adjustable number of Haar-random states. This is done by sampling the respective number of unitaries of size $2^k \times 2^k$ randomly from the unitary group $\mathcal{U}(2^k)$ [74], which conceptually is supported for an arbitrary number of data qubits k. The second method prepares states from a two-design. To enhance the experimental efficiency, which is crucial as the loss function is trained on the two-design approximations, we implement the respective state initializations in a parameterized way to allow for batch processing. One single qubit, i.e. $k = 1$, we place an arbitrary single-qubit rotation U_3, which is initialized with the values denoted in table 3 produces the desired states. We implement the same methodology also for $k = 2$ qubits, but we sketched in appendix B.4 how this also could be extended to larger systems.

Circuit Ansatz. The circuit ansatz determines the layout and allocation of trainable parameters that are trained to be the encoding or, respectively, recovery operation. In the `VarQEC` module, we implement the REA detailed in appendix D.1, but it is also readily extensible to other custom ansätze. The module enables setting a restricted connectivity as in appendix E.4, which selects target and control pairs only for qubits that are physically connected.

Noise channels. The noise channels are implemented and simulated using the `default.mixed` simulator of `PennyLane`. This includes all the noise channels that were detailed in appendix A.2. It

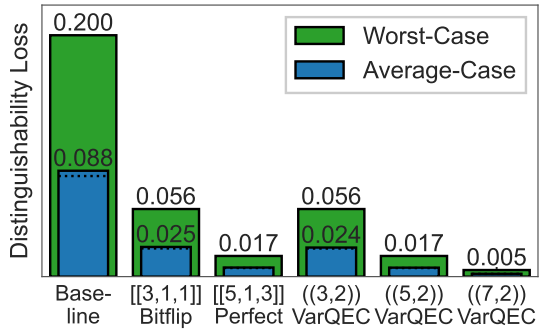

(a) Bit-flip noise with noise strength $p = 0.1$.

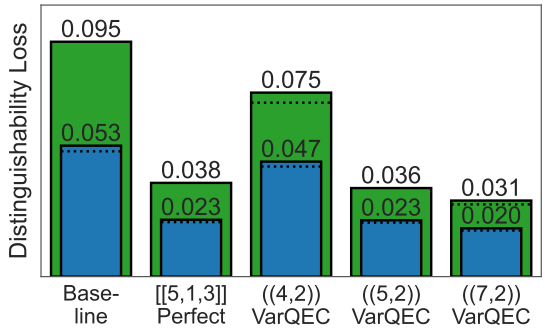

(b) Thermal relaxation noise of duration $t = 10.0$us with $T_1 = 200$us and $T_2 = 100$us.

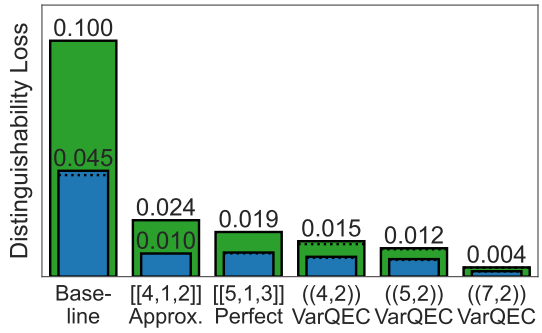

(c) Amplitude damping noise with damping parameter $\gamma = 0.1$.

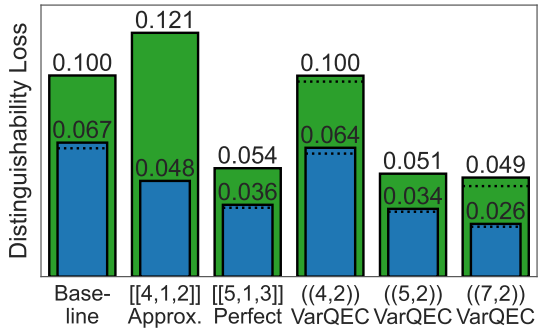

(d) Amplitude and Phase damping noise with damping parameter $\gamma = 0.1$.

Figure 14. Distinguishability loss for different QEC codes on (a) bit-flip, (b) thermal relaxation, (c) amplitude damping, and (d) consecutive amplitude and phase damping noise. All bars visualize the average-case loss $\mathcal{D}$ and worst-case loss $\overline{\mathcal{D}}$. Additionally, the two-design approximations $\mathcal{D}_{\mathcal{S}}, \overline{\mathcal{D}}_{\mathcal{S}}$ are visualized as dotted lines if the approximation was not exact. For the noise models, the unencoded baseline, the $[[5, 1, 3]]$ *perfect* code [57], optionally the $[[3, 1, 1]]$ *bit-flip* [92] and $[[4, 1, 2]]$ *approximate* QEC code [59], and VarQEC codes with $n = 3$ to $n = 7$ physical qubit are compared. All VarQEC ansätze are trained for 10 epochs and contain $(n - 1) \cdot (n - 2)$ two-qubit blocks. Results on symmetric and asymmetric depolarizing noise can be found in figure 5.

is also straightforward to extend the module with custom noise channels, or directly load hardware properties like T_1 and T_2 times.

Helper Functions. In addition to the main components detailed above, the `VarQEC` module also implements several supplementary functionalities. This includes the logging of training progress, different plotting functionalities, and the possibility to configure hyperparameters and the entire setup via the command line and configuration files.

Apart from this, we also provide a separate module that allows for the deployment of the trained models on quantum hardware. This experimental module is also available as described in the data availability statement. It implements methods to directly connect to the IBM Quantum experience [85], out also the IQM Resonance services [87].

Appendix E: Extended Empirical Results

In this appendix, we provide additional empirical evaluations to further substantiate the findings presented in section 5. We explore the performance of the proposed VarQEC method under various noise channels, assess its scalability to multiple logical qubits, further examine its stability, and analyze the resilience under restricted connectivity.

E.1 Additional Noise Channels

We first extend our analysis to learning encoding operations for additional noise models. The results for bit-flip, thermal relaxation, amplitude damping, and consecutive amplitude and phase damping channels are given in figure 14. For the bit-flip noise in figure 14(a) additional to the $[[5, 1, 3]]$ perfect code we also consider the $[[3, 1, 1]]$ bit-flip code [92]. Confirming our observations from the main part, the $((3, 2))$ VarQEC code performs on par with the bit-flip code, and the

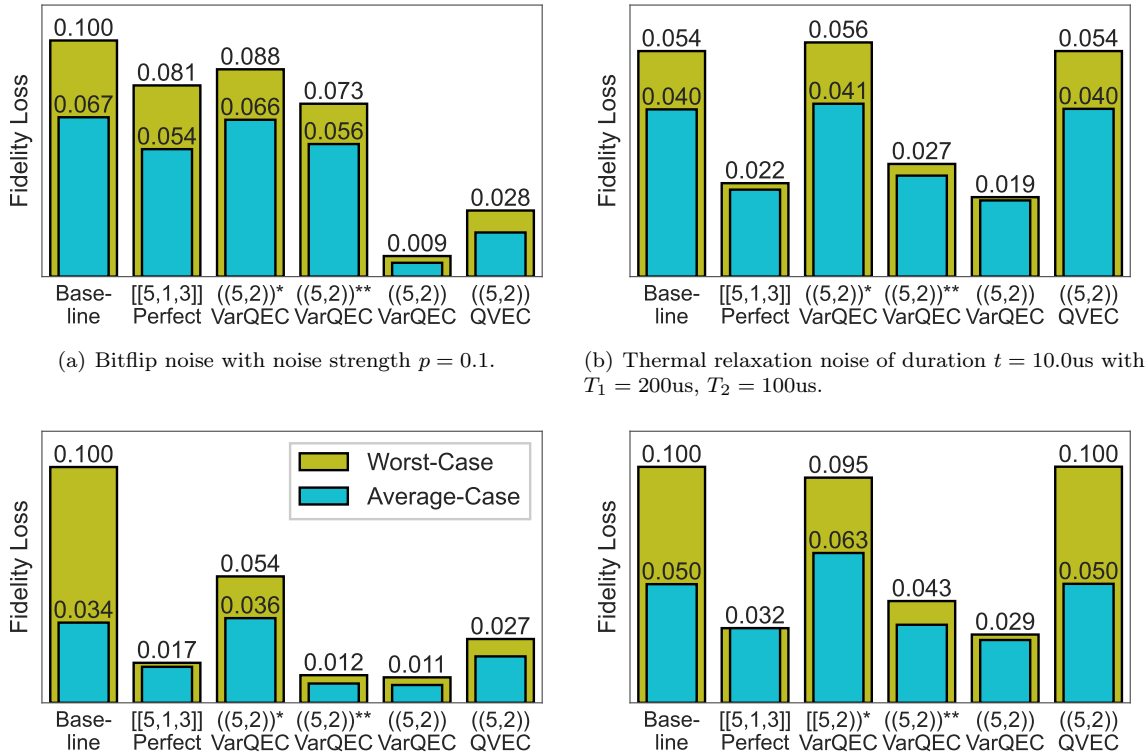

(a) Bitflip noise with noise strength $p = 0.1$.

(b) Thermal relaxation noise of duration $t = 10.0$us with $T_1 = 200$us, $T_2 = 100$us.

(c) Amplitude damping noise with damping parameter $\gamma = 0.1$.

(d) Amplitude and Phase damping noise with damping parameter $\gamma = 0.1$.

Figure 15. Fidelity loss for different QEC codes and respective recovery operations on (a) bit-flip, (b) thermal relaxation, (c) amplitude damping, and (d) consecutive amplitude and phase damping noise. All bars visualize the average-case loss $\mathcal{F}$ and worst-case loss $\overline{\mathcal{F}}$. For the noise models, the unencoded baseline, and the $[[5, 1, 3]]$ *perfect* code is visualized, optionally extended by the $[[3, 1, 1]]$ *bit-flip* and $[[4, 1, 2]]$ *approximate* QEC code. Additionally, we compare three instances of VarQEC codes, where $((5, 2))^*$ employs a random encoding, $((5, 2))^{**}$ employs a encoding that has converged to a locally optimal distinguishability loss, and the encoding of $((5, 2))$ has converged to a global optimum. The recovery operations are successively trained following *equation* (26). For the rightmost model, the encoding and recovery operations have been trained end-to-end with the QVECTOR approach [50] as described in appendix C. The recovery ansätze are trained using the fidelity loss for 50 epochs and contain 200 two-qubit blocks. As we consider a single-recovery scenario, no separate recovery register was used, i.e. the recovery operation acts solely on the n-qubit encoded and disturbed state [50]. The distinguishability loss for all encodings is summarized in table 4. Results on symmetric and asymmetric depolarizing noise can be found in figure 7.

$((5, 2))$ VarQEC code performs on par with the perfect code. Moreover, increasing the number of physical qubits to $n = 7$ allows for further reduction of the distinguishability loss. For the thermal relaxation channel in figure 14(b), results are similar to those in depolarizing noise in figure 5(a), but the VarQEC codes manage to have a small edge over the perfect code. A similar connection can be observed for the amplitude and phase damping noise in figure 14(d). for isolated amplitude damping noise in figure 14(c) we additionally compare the $[[4, 1, 2]]$ *approximate* QEC code [59]. Also, here increasing the number of physical qubits in the VarQEC codes significantly reduces the achieved distinguishability loss further.

Building upon this, we train respective recovery operations and evaluate the fidelity losses in figure 7. The distinguishability losses of the underlying encoding circuits and the implied bounds are summarized in table 4. In agreement with the results from the main part, we can observe that a lower distinguishability loss allows for a higher-fidelity recovery operation. On all considered instances, we can observe that the optimal VarQEC codes outperform the unencoded baseline, the $[[5, 1, 3]]$ perfect code, and also the $((5, 2))$ code trained with the QVECTOR approach. In appendix B.3 we determine the $((5, 2))$ VarQEC code trained on amplitude damping noise to exhibit a potential approximate code distance of $d = 2$. This aligns with the code distance of the $[[4, 1, 2]]$ approximate QEC code, which is known to be especially suited for the amplitude damping channel [59]. We again want to emphasize that the QVECTOR approach employs the same circuit ansätze as the VarQEC codes. For bit-flip and amplitude damping noise, the $((5, 2))$ QVECTOR codes also significantly improve upon the unencoded baseline performance, which is in agreement with the results from Ref. [50]. However, already on these and especially on the more complex

		Base-line	$[[5,1,3]]$ Perfect	$((5,2))^*$ VarQEC	$((5,2))^{**}$ VarQEC	$((5,2))$ VarQEC	$((5,2))$ QVEC
bitflip	$\overline{\mathcal{D}} =$	0.200	**0.017**	0.171	0.142	**0.017**	0.056
	$\overline{\mathcal{F}} \leq$			0.168	0.263	0.034	
	$\overline{\mathcal{F}} =$	0.100	0.081	0.088	0.083	**0.009**	0.028
	$\overline{\mathcal{F}} \geq$			0.008	0.020	0.001	
thermal relaxation	$\overline{\mathcal{D}} =$	0.095	0.038	0.095	0.050	**0.036**	0.095
	$\overline{\mathcal{F}} \leq$			0.109	0.098	0.071	
	$\overline{\mathcal{F}} =$	0.054	0.022	0.056	0.027	**0.019**	0.054
	$\overline{\mathcal{F}} \geq$			0.003	0.003	0.001	
amplitude damping	$\overline{\mathcal{D}} =$	0.100	0.019	0.080	0.020	**0.012**	0.043
	$\overline{\mathcal{F}} \leq$			0.104	0.040	0.024	
	$\overline{\mathcal{F}} =$	0.100	0.017	0.054	0.012	**0.011**	0.027
	$\overline{\mathcal{F}} \geq$			0.003	0.001	0.001	
amplitude-phase damping	$\overline{\mathcal{D}} =$	0.100	0.054	0.154	0.084	**0.051**	0.100
	$\overline{\mathcal{F}} \leq$			0.182	0.161	0.100	
	$\overline{\mathcal{F}} =$	0.100	0.032	0.095	0.043	**0.029**	0.100
	$\overline{\mathcal{F}} \geq$			0.009	0.007	0.003	

Table 4. Worst-case distinguishability loss $\overline{\mathcal{D}}$ exhibited by the encodings for the models in figure 15. For the baseline and $[[5,1,3]]$ code, this is evaluated on the unencoded baseline and static encoding operation, respectively. For the VarQEC codes, this corresponds to an untrained encoding for $((5,2))^*$, to an local optimum for $((5,2))^{**}$, and to a global optimum for $((5,2))$. For the $((5,2))$ QVECTOR code, the same ansatz with 12 two-qubit blocks as for the VarQEC codes is employed, but training was only implicitly conducted via the fidelity loss. Additionally, we again report the worst-case fidelity loss $\overline{\mathcal{F}}$ (third line) and the respective upper (second) and upper bounds (fourth line) following Theorems 1 and 2 for the VarQEC models.

thermal relaxation noise channel, this end-to-end ansatz produces results that are inferior to the VarQEC procedure.

E.2 Multiple Data Qubits

We now assess the extension of the previous experiments to the setup with multi-qubit logical states, in particular $k = 2$. For this two-qubit setup, we enumerate elements of a two-design in appendix B.4. In figure 16, we report the distinguishability loss for a variety of such setups on both symmetric and asymmetric depolarizing noise. We include the unencoded baseline, which in this context corresponds to a two-qubit state. We additionally compare to the $[[4,2,2]]$ QEC code [105] and the $[[8,2,3]]$ QEC code [77]. Using our VarQEC routine, we train codes with sizes from $n = 4$ to $n = 8$ physical qubits.

The results in on the symmetric depolarizing channel in figure 16(a) indicate that for this setup, the $((8,4))$ VarQEC are not fully competitive with the $[[8,2,3]]$ QEC code, which, similar to the perfect code on a single logical qubit, is the smallest code with distance $d = 3$ on two logical qubits. However, we assume this gap could be eliminated by resorting to a more sophisticated ansatz construction. On the contrary, the results on asymmetric depolarizing noise in figure 16(b) demonstrate that the VarQEC codes reduce the distinguishability loss compared to the *standard* QEC codes.

We recall that in QEC it is standard to encode only a few logical qubits in a single code patch. Surface codes typically store one logical qubit per patch [35], while modern Q-LDPC codes can encode around a dozen logical qubits [13]. Fault-tolerant interactions between such patches are implemented using protocols like lattice surgery [47]. Developing analogous protocols and operations for the VarQEC procedure is left for future work.

E.3 Extended Stability Analysis

We now analyze the stability of the VarQEC codes and the adaptability of the VarQEC procedure. Therefore, for both symmetric and asymmetric noise, we vary the noise strength from $p = 0.05$ to $p = 0.25$. Similar to the main part, we compare the unencoded baseline, the $[[5,1,3]]$ perfect code, a static VarQEC code trained on noise strength of $p = 0.1$, and VarQEC codes dynamically trained on the respective noise strengths. For the depolarizing noise in figure 17(a), we observe that all QEC codes perform equally well up to the physical noise threshold of about $p = 0.15$. After that, both the $[[5,1,3]]$ code and static VarQEC code perform worse than just a physical qubit without encoding. The dynamically trained VarQEC code at least performs on par with the purely physical setup, but also can not improve upon it. For the asymmetric depolarizing noise in figure 17(b), the $[[5,1,3]]$ code requires a physical threshold of again approximately $p = 0.15$. However, both VarQEC codes can significantly improve upon this and still work for $p = 0.25$. While dynamically

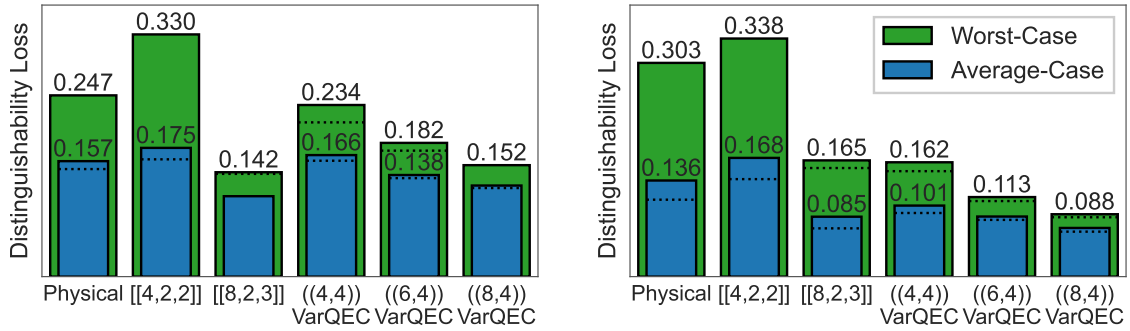

(a) Depolarizing noise with noise strength $p = 0.1$.

(b) Asymmetric depolarizing noise with noise strength $p = 0.1$ and asymmetry $c = 0.5$ following equation (45).

Figure 16. Distinguishability loss for different QEC codes with two logical qubits, i.e. $k = 2$, on (a) depolarizing and (b) asymmetric depolarizing noise. All bars visualize the average-case loss $\mathcal{D}$ and worst-case loss $\overline{\mathcal{D}}$. Additionally, the two-design approximations $\mathcal{D}_{\mathcal{S}}, \overline{\mathcal{D}}_{\mathcal{S}}$ are visualized as dotted lines if the approximation was not exact. For both noise models, the unencoded baseline, the $[[4, 2, 2]]$ QEC code [105], the $[[8, 2, 3]]$ QEC code [77], and VarQEC codes with $n = 4$, $n = 6$, and $n = 8$ physical qubits are compared. All VarQEC ansätze are trained for 10 epochs and contain $n \cdot (n - 1)$ two-qubit blocks. Results on only a single data qubit can be found in figure 5.

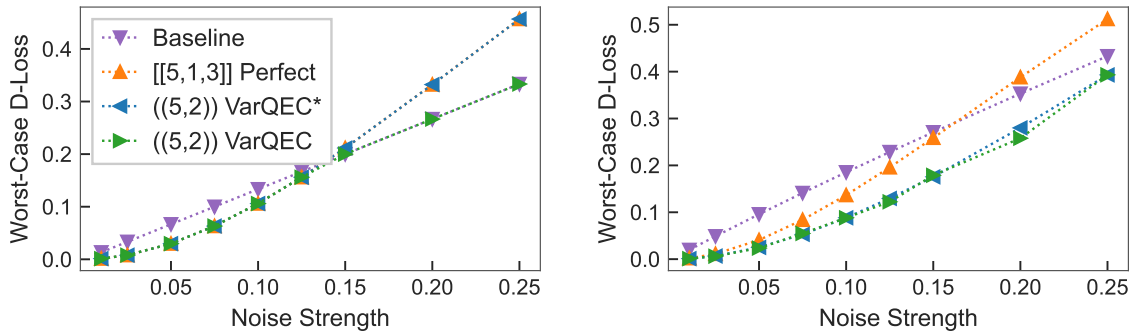

(a) Depolarizing noise with noise strength $p = 0.1$.

(b) Asymmetric depolarizing noise with noise strength $p = 0.1$ and asymmetry $c = 0.5$ following equation (45).

Figure 17. Stability of standard QEC and VarQEC codes with increasing noise strength for (a) symmetric and (b) asymmetric depolarizing noise. All data points represent the respective worst-case distinguishability loss $\overline{\mathcal{D}}$. The $((5, 2))^*$ VarQEC code is always the same *static* one trained on a noise strength $p = 0.1$. The other $((5, 2))$ VarQEC code is *dynamically* trained on the respective denoted noise configuration.

tailoring the VarQEC code brings slight advantages for some configurations, the differences are not significant.

We extend this analysis by evaluating the scenario of non-uniform noise strength between the involved qubits in figure 18(a), which is typically resembled in actual hardware due to manufacturing quality [83]. More concretely, we vary the strength of depolarizing noise on the qubit corresponding to the initial data wire from values $p = 0.05$ to $p = 0.2$. All other involved ancilla qubits exhibit a depolarizing noise of $p = 0.1$. To compare to a harder baseline, for the case of a single physical qubit, we select the lower noise strength. As expected, the $[[5, 1, 3]]$ perfect code outperforms the purely physical setup up until a threshold noise strength of approximately 0.175. The *static* version of the $((5, 2))$ VarQEC code performs on par for all setups. The $((5, 2))$ VarQEC *dynamically* trained on the respective noise configurations does not drop beyond the baseline, even above the physical threshold.

In figure 18(b) we perform some transferability analysis of the $((5, 2))$ VarQEC code that was trained on depolarizing noise of strength $p = 0.1$. As evaluated in appendix B.3, this code exhibits a potential code distance of $d = 3$, and therefore also should apply to other noise channels. Indeed, the transferred code exhibits distinguishability losses that are significantly beyond the unencoded baselines (compare figure 14). Moreover, for amplitude damping and combined amplitude and phase damping noise, the results are again competitive with the $[[5, 1, 3]]$ perfect code. We have to highlight that one can further improve upon this by tailoring the codes explicitly to the respective noise channels. However, these results still demonstrate that the learned VarQEC codes partially generalize to other noise models. This might allow for some warm-start parameter initialization

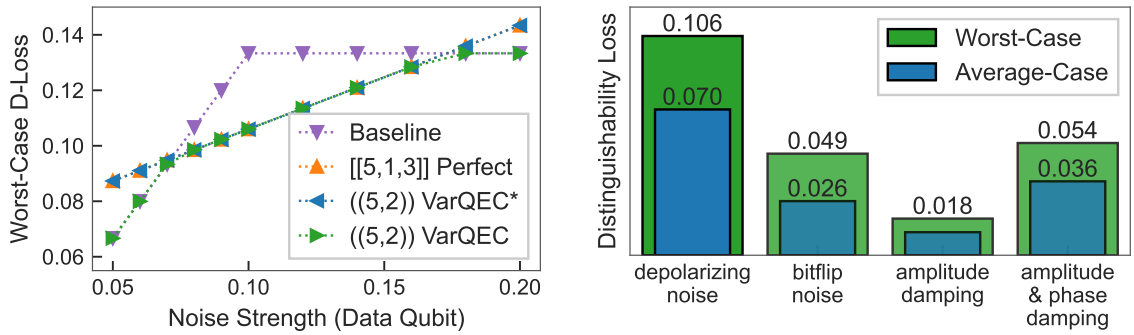

(a) Depolarizing noise with noise strength $p = 0.1$ on $n-1$ of the qubits, and with a noise strength as denoted on the x-axis on the remaining qubit. For the QEC codes, the deviating qubit is associated with the original data qubit, while the unencoded baseline employs the best available wire.

(b) Transfer of VarQEC code with $n = 5$ physical qubits trained on depolarizing noise with strength $p = 0.1$ to other noise types. The bitflip noise also features a noise strength of $p = 0.1$, while phase and amplitude damping both have a damping parameter of $\gamma = 0.1$.

Figure 18. Stability of standard QEC and VarQEC codes in setups of varying (a) noise strength on different qubits and (b) noise channels. All data points represent the respective worst-case distinguishability loss $\overline{\mathcal{D}}$ and optionally average-case loss $\mathcal{D}$. The $((5,2))^*$ VarQEC code is always the same static one trained on depolarizing noise with noise strength $p = 0.1$ on all qubits. The other $((5,2))$ VarQEC code is dynamically trained on the respective noise configuration.

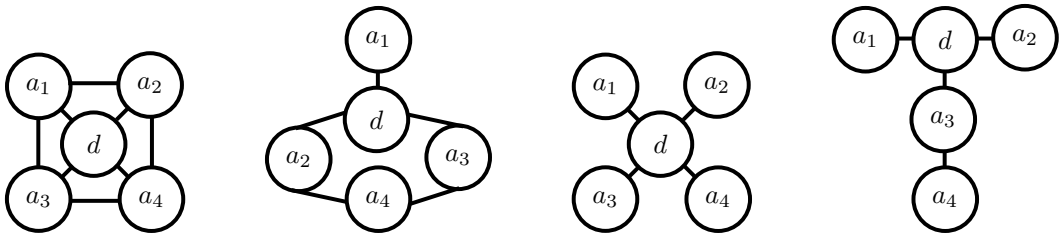

(a) "dense" layout (b) "square" layout (c) "star" layout (d) "hexagonal" layout

Figure 19. Different layouts for $n = 5$ physical qubits satisfying the connectivity restrictions of some potential underlying hardware. Throughout most of this paper, we assumed a "full" connectivity, which is not available on most hardware systems. Similarly, the "dense" layout might be hard to realize with on most platforms. The "square" as well as the "star" layout aligns e.g. with the grid-based topology of the Google Quantum AI chips [3]. The "hexagonal" layout is adapted to the *heavy-hex* topology of IBM Quantum devices [85].

approaches [69], indicating that models do not always need to be trained from scratch but rather only finetuned.

E.4 Restricting Connectivity Structure and Fault Resilience

Most quantum hardware platforms do not support all-to-all connectivity, but rather assume some restricted topology. In principle, it is possible to compile a quantum circuit to the respective layout, which, however, typically requires routing with e.g. swap gates. We can entirely avoid this for the VarQEC procedure by initially selecting a variational ansatz that is adapted to the hardware connectivity restrictions. Therefore, we now consider the four different layouts in figure 19, i.e., "dense", "square", "star", and "hexagonal". The randomized entangling ansätze are configured to inherently apply to these restrictions.

For the results in table 5, we trained $((5,2))$ VarQEC codes with 6 to 20 two-qubit blocks on depolarizing noise. For each layout, we report the respective smallest code instance that produces the optimal distinguishability loss of $\overline{\mathcal{D}} \approx 0.106$. In addition to that, we compile the $[[5,1,3]]$ perfect encoding circuit [111] for the respective layout, using the `qiskit.transpile` method [49], and report the respective number of two-qubit gates. This significantly increases the circuit depth, while for the VarQEC codes, the circuit complexity only needs to increase slightly with lower connectivity density.

For realistically modeling idle qubits, one typically resorts to the thermal relaxation noise channel. Therefore, we repeat the above analysis on the VarQEC circuits for this setup with $T_1 = 200\mu s$, $T_2 = 100\mu s$, $t = 10.0\mu s$, and report results in table 6. The results underline that the VarQEC can easily adapt to sparse connectivity, with just a slight increase in circuit depth.

	layout				
	"full"	"dense"	"square"	"star"	"hexagonal"
$[[5,1,3]]$ Perfect	6	9	15	12	18
$((5,2))$ VarQEC	12	10	10	12	16

Table 5. Number of two-qubit gates for $[[5,1,3]]$ perfect code compiled to the different layouts in figure 19 and smallest number of two-qubit blocks for which a $((5,2))$ VarQEC code achieves the optimal worst-case distinguishability loss of $\overline{\mathcal{D}} \approx 0.106$ for depolarizing noise with $p = 0.1$.

	number of blocks							
	6	8	10	12	14	16	18	20
"Full" layout	0.0615	0.0459	0.0366	**0.0349**	**0.0348**	**0.0347**	**0.0347**	**0.0348**
"Dense" layout	0.0573	0.0363	0.0352	0.0359	0.0358	**0.0348**	**0.0347**	**0.0348**
"Square" layout	0.0619	0.0502	0.0359	**0.0347**	0.0366	**0.0348**	**0.0350**	**0.0348**
"Star" layout	0.0611	0.0453	0.0359	0.0359	0.0359	**0.0348**	**0.0347**	**0.0348**
"Hexagonal" layout	0.0502	0.0502	0.0367	0.0383	0.0359	0.0367	0.0354	**0.0347**

Table 6. Worst-case distinguishability loss $\overline{\mathcal{D}}$ for thermal relaxation noise with duration $t = 10.0\mu s$ with $T_1 = 200\mu s$ and $T_2 = 100\mu s$ using an increasing number of two-qubit blocks in $((5,2))$ VarQEC encoding circuits.

Last but not least, we consider the noise-resilience of the encodings under the assumption of restricted connectivity figure 20. Similar to the main part, we evaluate this by adding correlated depolarizing noise of increasing strength after each two-qubit gate. We consider symmetric depolarizing noise, i.e. under the assumption of ideal encoding operations, the $[[5,1,3]]$ code is optimal. For "full", "dense", and "'square' connectivity layouts, the compiled codes are more resilient than the VarQEC codes, mainly due to the circuits being shallower. However, the VarQEC codes shine under sparse connectivity structures like especially "hexagonal", where this trend reverses. We want to emphasize that, e.g. for asymmetric depolarizing noise, the VarQEC codes would exhibit superior noise-resilience on all layouts, as already under full-connectivity assumptions, there was quite some performance gap as analyzed in figure 6(b).

This extended analysis of the VarQEC procedure reinforces the conclusion from the main part, in particular that the VarQEC codes are adaptable to a wide range of noise models. The codes themselves, furthermore, are stable over a wide range of noise fluctuations. Moreover, the approach itself is perfectly suited for developing codes under restricted connectivity.

Appendix F: Closer Look at the Hardware Experiments

In this appendix, we provide additional details on the hardware experiments conducted to validate the practical applicability of our proposed VarQEC codes. By deploying our models on different quantum computing platforms, we aim to demonstrate the adaptability and resilience of our approach under realistic conditions.

F.1 General Experimental Setup

We utilized the VarQEC framework for training the codes in simulation. We provide a separate implementation for submitting the results to IBM and IQM hardware, as well as for retrieving and analyzing the results, as indicated in the data availability statement. Our implementation builds upon the `qiskit-experiments` module [52], which we modified to support cluster re-sampling [17, 73] of the data. The quantum states were reconstructed using mitigated state tomography, offering a proof-of-concept demonstration of our approach despite the scalability limitations of state tomography.

For the IBM Quantum device, we simulated idling by adding `qiskit.delay` operations of specific durations to the involved qubits. On the IQM device, which does not natively support delay operations, we approximated idling by adding several identity gates equivalent to the desired delay, assuming that each single-gate execution takes approximately $30.0ns$ [2]. To efficiently utilize hardware resources and reduce access costs, we executed multiple logical patches in parallel. Specifically, we deployed 8 logical patches on the 156-qubit IBM device and 3 logical patches on the 20-qubit IQM device. State tomography was also executed in parallel, and we verified that this parallel execution did not significantly degrade the quality of the results compared to sequential execution.

We compared the hardware results to the training predictions on the distinguishability loss, as depicted in figure 21. While the hardware measurements reported in figures 22 and 24 exhibit quantitatively higher distinguishability loss than the simulation predictions, they still demonstrate

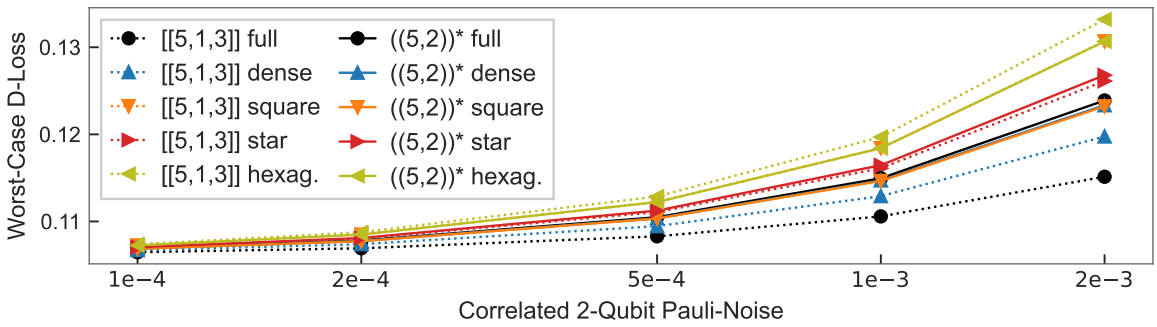

Figure 20. Resilience of standard QEC and VarQEC codes in setups of non-ideal encoding operations under symmetric depolarizing noise of strength $p = 0.1$. All data points represent the respective worst-case distinguishability loss $\overline{\mathcal{D}}$. The solid lines represent static VarQEC codes trained under the assumption of ideal encoding operations, adapted to the respective layouts. The dashed lines correspond to the $[[5, 1, 3]]$ QEC code, compiled for the respective connectivity structure. The unencoded baseline, which does not include any two-qubit operations, is at approximately 0.133. The encoding circuit depths of the respective codes are summarized in table 5.

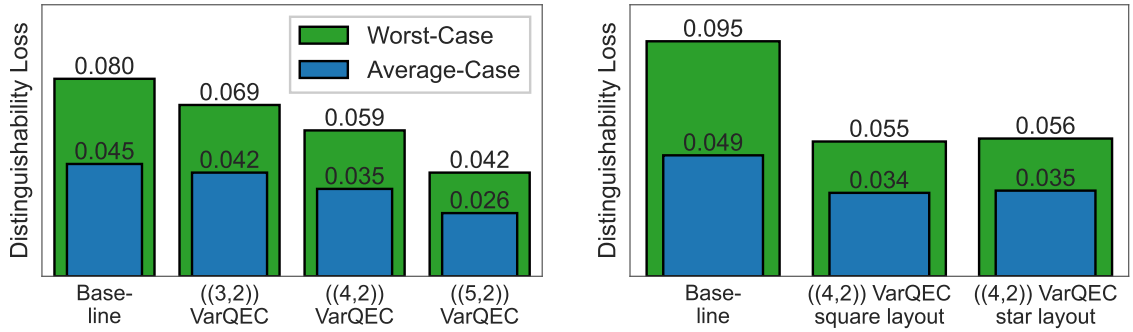

(a) Thermal relaxation noise with $T_1 = 180\mu s$ and $T_2 = 120\mu s$ for $t = 10.0\mu s$ as encountered in the median on the `ibmq_marrakesh` device.

(b) Thermal relaxation noise with $T_1 = 48\mu s$ and $T_2 = 20\mu s$ for $t = 2.0\mu s$ as encountered in the median on the `IQM Garnet` device.

Figure 21. Distinguishability loss for different QEC codes on thermal relaxation noise modeling the median error properties for (a) an IBMQ device and (b) an IQM device. All bars visualize the average-case loss $\mathcal{D}$ and worst-case loss $\overline{\mathcal{D}}$. For the IBMQ noise model, we compare the unencoded baseline and VarQEC codes with $n = 3$ to $n - 5$ physical qubits. The $((4, 2))$ VarQEC code for this setup is plotted in figure 23. For the IQM noise model, we compare the unencoded baseline to the results of $((4, 2))$ VarQEC codes with different layout alignments. The codes are trained in classical simulation and afterwards deployed on quantum hardware, as denoted by the experiments in this section.

beyond break-even performance as we discuss in the following, corroborating the observations from the main text in section 6.

F.2 Extended Results on IBMQ Decides

We conducted experiments on the `ibm_marrakesh` device [85], which features a 156-qubit `Heron r2` chip. The median properties of the qubits were identified as $T_1 = 180\mu s$ and $T_1 = 120\mu s$. Due to additional sources of error, such as noise introduced during the encoding operations and measurement delays, we trained the encoding with a noise duration of $t = 10.0\mu s$ and deployed it on the hardware for $t = 5.0\mu s$ (compare also section 6).

We trained and deployed VarQEC codes with $n = 3$ to $n = 5$ physical qubits. The experiments required approximately 12 QPU minutes for the 3-qubit code, 25 QPU minutes for the 4-qubit code, and 72 QPU minutes for the 5-qubit code, accessed via the IBM Quantum premium plan. The logical qubit allocations for the $((3, 2))$, $((4, 2))$ and $((5, 2))$ VarQEC codes are summarized in table 7. The gates used in our ansätze were aligned with the native gate set of the device, employing CZ gates for two-qubit operations and parameterized single-qubit rotations implemented as $R_{zxz}(\theta, \phi, \xi) = R_z(\xi)R_x(\phi)R_z(\theta)$. The results, depicted in figure 8(b) of the main text, indicate a decrease in the distinguishability loss with an increasing number of physical qubits, thus demonstrating improved error correction performance with larger codes.

Detailed results for the 8 individual patches of the $((4, 2))$ VarQEC code are provided in figure 22. We note both worst-case and average-case distinguishability losses, with error bars

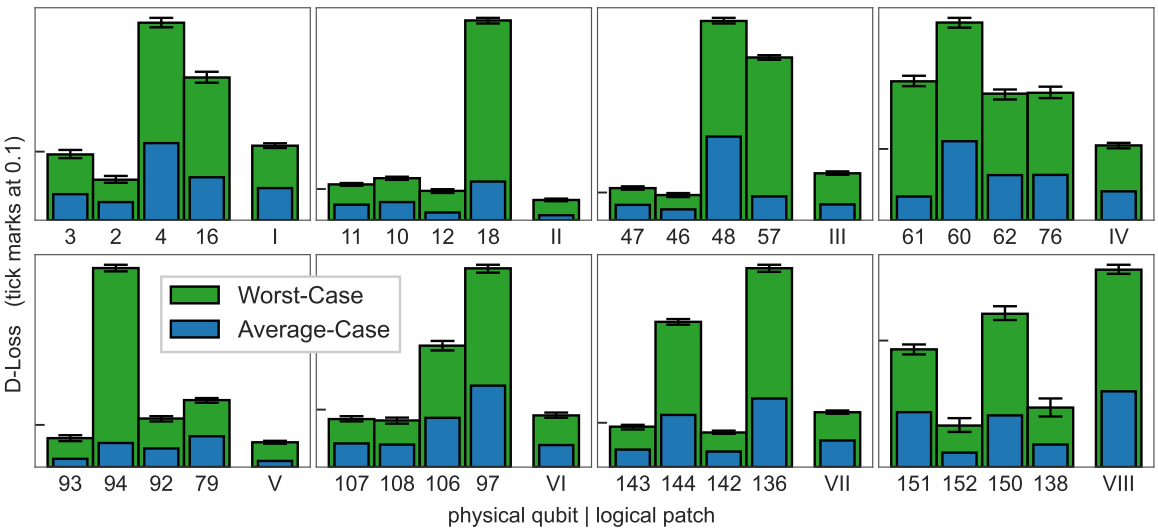

Figure 22. Reconstructed distinguishability loss for the 8 patches of the experiment with the $((4, 2))$ VarQEC code on the `ibm_marrakesh` device. The qubits have been idled for $5.0\mu s$ for this experiment. For each patch, the first four bars indicate the unencoded baseline losses for the respective physical qubits, while the fifth one denotes the loss for the entire encoded patch. The losses were estimated with mitigated state tomography using 10000 shots per circuit execution, and the error bars denote 5th and 95th percentile ranges estimated by cluster re-sampling. The alignment and layout of physical wires to logical patch is also summarized in table 7, and the circuit realizing the encoding is given in figure 23.

		logical patch							
		I	II	III	IV	V	VI	VII	VIII
	d	3	12	47	61	93	107	143	151
	a_1	2	10	46	60	94	108	144	152
wire	a_2	4	12	48	62	92	106	142	150
	a_3	16	18	57	76	79	97	136	138
	a_4	23	31	67	81	73	87	123	131

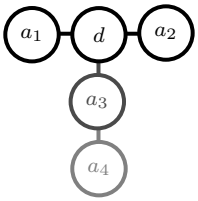

Table 7. Physical wire allocation of the encoding patches for the experiment on the IBMQ device `ibm_marrakesh` depicted in figure 22. The device uses a `Heron r2` chip with 156 qubits, the physical wire indices refer to the numbering in the IBMQ documentation [85]. The connectivity is adapted to the hexagonal connectivity structure, each single 5-qubit encoding patch is allocated as depicted on the right. Hereby, d denotes the initial physical data qubit to be protected, and a_1, a_2, a_3, and a_4 are ancilla qubits. For the experiments with encodings on 4 and 3 wires, the ancilla qubits a_4 and a_3 are dropped, respectively.

indicating the 5th and 95th percentile ranges evaluated by cluster re-sampling. The experiments were conducted with 10000 shots for each circuit in the mitigated state tomography process. The concrete ansatz for the $((4, 2))$ VarQEC code, consisting of four two-qubit blocks, is illustrated in figure 23. We observed that while the VarQEC code does not outperform the best physical qubit in every individual patch, especially in patches with significant qubit quality fluctuations, the overall results indicate a reduction in the distinguishability loss on average. This is particularly pronounced in patches where the qubit quality is more uniform (e.g., patch IV). In some patches, the logical results did not outperform the best physical qubit, which we attribute to variances in qubit quality and, in one case, a defective two-qubit connection (patch VIII).

F.3 Results on IQM Devices

We also deployed our VarQEC codes on the 20-qubit `IQM Garnet` device with a crystal topology, accessed via the IQM Resonance services [87]. The median coherence times were $T_1 = 180\mu s$ and $T_1 = 120\mu s$ [2]. Given these limited coherence times, we reduced the idling time to $t = 2.0\mu s$ during training and further to $t = 1.0\mu s$ for hardware deployment. Due to access constraints, we limited the number of shots per circuit to 1000. The ansatz gates were adapted to the native gate set of the device, utilizing CZ gates for two-qubit operations and parameterized single-qubit gates implemented as $PR_x(\theta, \phi) = R_z(\phi)R_x(\theta)R_z(-\phi)$.

The denser grid connectivity of the IQM device allowed us to experiment with different ansatz topologies, specifically the "star" and "square" layouts. However, the results do not show a significant difference between the two layouts, which we expect to change for larger codes, as analyzed in appendix E.4. The increased span of the error bars can be attributed to the reduction

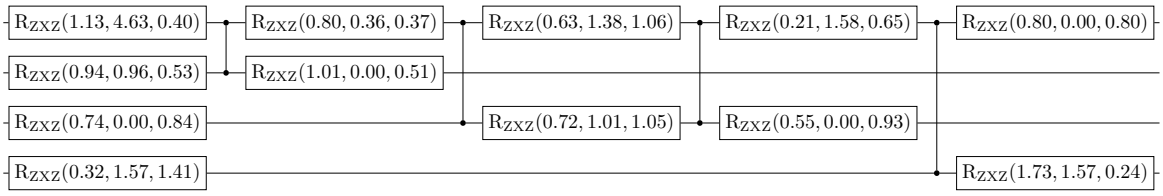

Figure 23. Circuit ansatz implementing the $((4, 2))$ VarQEC code. The parameters were trained on the noise setup for the `iqm_marrakesh` experiment that is analyzed in figure 22. The circuit is an instance of a randomized entangling ansatz (RAG, see appendix D.1) restricted to the "hexagonal" four-qubit layout with the basis gate set of the IBM devices. It contains four two-qubit blocks, with overall 36 parameters. The uppermost wire corresponds to the initial data qubit.

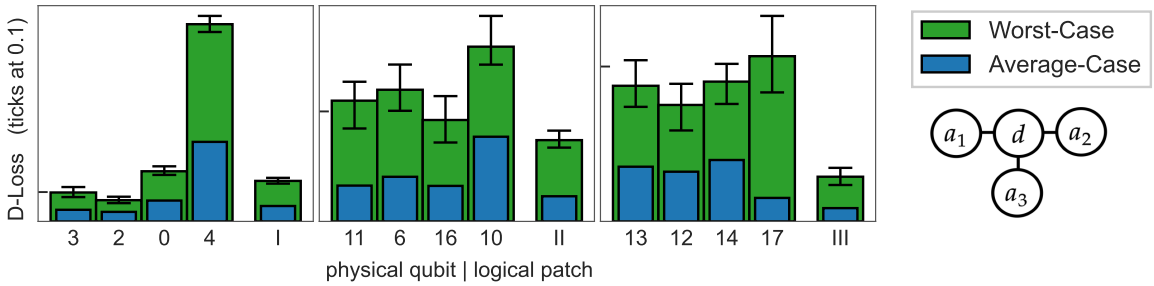

(a) Alignment of physical qubits to logical patches following the "star" shape. For the four-qubit setup, this is also compatible with the "hexagonal" layout.

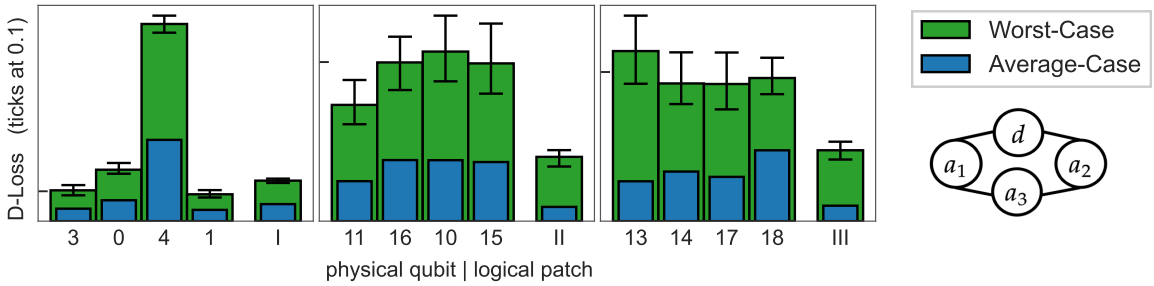

(b) Alignment of physical qubits to logical patches following the "square" shape.

Figure 24. Reconstructed distinguishability loss for the 3 patches of the experiment with the $((4, 2))$ VarQEC code on the `IQM Garnet` device. The qubits have been idled for $1.0\mu s$ for this experiment. We consider two different physical qubit to logical patch alignment strategies, in particular (a) "star" and (b) "square" alignment. For each patch, the first four bars indicate the unencoded baseline losses for the respective physical qubits, while the fifth one denotes the loss for the entire encoded patch. The losses were estimated with mitigated state tomography using 1000 shots per circuit execution, and the error bars denote 5th and 95th percentile ranges estimated by cluster re-sampling.

of the shot count by a factor of 10. We observed that in both layouts, qubit 4 was defective during our experiments, leading to outlier results in patch I. In patches II and III, we achieved a clear net gain in performance, as the logical distinguishability loss was significantly lower than that of the best physical qubit. The smaller variance in qubit quality on the IQM device facilitated better evaluation of our code's functionality, given that our training assumed uniform noise levels across qubits.

The hardware experiments conducted on both IBM Quantum and IQM devices demonstrate the practical viability and adaptability of our VarQEC approach under realistic conditions. Despite the inherent limitations of current quantum hardware, such as qubit decoherence and gate imperfections, our codes showed improved performance in preserving quantum information. Our results underline the effectiveness of tailoring error correction codes to specific hardware platforms and noise characteristics. The VarQEC procedure's adaptability allows for optimizing encodings that are robust against the particular noise profiles and connectivity constraints of different quantum devices. Future work could further enhance performance by incorporating more sophisticated device-specific noise models directly into the training process.

References

[1] Amira Abbas, Andris Ambainis, Brandon Augustino, Andreas Bärtschi, Harry Buhrman, Carleton Coffrin, Giorgio Cortiana, Vedran Dunjko, Daniel J Egger, Bruce G Elmegreen, et al. Challenges and opportunities in quantum optimization. *Nat. Rev. Phys.*, pages 1–18, 2024.

[2] Leonid Abdurakhimov, Janos Adam, Hasnain Ahmad, Olli Ahonen, Manuel Algaba, Guillermo Alonso, Ville Bergholm, Rohit Beriwal, Matthias Beuerle, Clinton Bockstiegel, et al. Technology and performance benchmarks of iqm's 20-qubit quantum computer. *arXiv:2408.12433*, 2024.

[3] Rajeev Acharya, Laleh Aghababaie-Beni, Igor Aleiner, Trond I Andersen, Markus Ansmann, Frank Arute, Kunal Arya, Abraham Asfaw, Nikita Astrakhantsev, Juan Atalaya, et al. Quantum error correction below the surface code threshold. *Nature*, 638:920–926, 2025.

[4] Yuri Alexeev, Marwa H Farag, Taylor L Patti, Mark E Wolf, Natalia Ares, Alán Aspuru-Guzik, Simon C Benjamin, Zhenyu Cai, Zohim Chandani, Federico Fedele, et al. Artificial intelligence for quantum computing. *arXiv:2411.09131*, 2024.

[5] Panos Aliferis and John Preskill. Fault-tolerant quantum computation against biased noise. *Phys. Rev. A*, 78(5):052331, 2008.

[6] Andris Ambainis and Joseph Emerson. Quantum t-designs: t-wise independence in the quantum world. In *Twenty-Second Annual IEEE Conference on Computational Complexity (CCC'07)*, pages 129–140, 2007.

[7] Raef Bassily, Vitaly Feldman, Cristóbal Guzmán, and Kunal Talwar. Stability of stochastic gradient descent on nonsmooth convex losses. In *Advances in Neural Information Processing Systems (NeurIPS)*, volume 33, pages 4381–4391, 2020.

[8] Johannes Bausch and Felix Leditzky. Quantum codes from neural networks. *New J. Phys.*, 22(2):023005, 2020.

[9] Johannes Bausch, Andrew W Senior, Francisco JH Heras, Thomas Edlich, Alex Davies, Michael Newman, Cody Jones, Kevin Satzinger, Murphy Yuezhen Niu, Sam Blackwell, et al. Learning high-accuracy error decoding for quantum processors. *Nature*, 635:834–840, 2024.

[10] Cédric Bény and Ognyan Oreshkov. General conditions for approximate quantum error correction and near-optimal recovery channels. *Phys. Rev. Lett.*, 104(12):120501, 2010.

[11] Ville Bergholm, Josh Izaac, Maria Schuld, Christian Gogolin, Shahnawaz Ahmed, Vishnu Ajith, M Sohaib Alam, Guillermo Alonso-Linaje, B AkashNarayanan, Ali Asadi, et al. Pennylane: Automatic differentiation of hybrid quantum-classical computations. *arXiv:1811.04968*, 2018.

[12] Jacob Biamonte, Peter Wittek, Nicola Pancotti, Patrick Rebentrost, Nathan Wiebe, and Seth Lloyd. Quantum machine learning. *Nature*, 549(7671):195–202, 2017.

[13] Sergey Bravyi, Andrew W Cross, Jay M Gambetta, Dmitri Maslov, Patrick Rall, and Theodore J Yoder. High-threshold and low-overhead fault-tolerant quantum memory. *Nature*, 627(8005):778–782, 2024.

[14] Donald Bures. An extension of kakutani's theorem on infinite product measures to the tensor product of semifinite w*-algebras. *Trans. Am. Math. Soc.*, 135:199–212, 1969.

[15] A Robert Calderbank, Eric M Rains, Peter W Shor, and Neil JA Sloane. Quantum error correction and orthogonal geometry. *Phys. Rev. Lett.*, 78(3):405, 1997.

[16] A Robert Calderbank and Peter W Shor. Good quantum error-correcting codes exist. *Phys. Rev. A*, 54(2):1098, 1996.

[17] A Colin Cameron, Jonah B Gelbach, and Douglas L Miller. Bootstrap-based improvements for inference with clustered errors. *Rev. Econ. Stat.*, 90(3):414–427, 2008.

[18] Earl T Campbell, Barbara M Terhal, and Christophe Vuillot. Roads towards fault-tolerant universal quantum computation. *Nature*, 549(7671):172–179, 2017.

[19] Chenfeng Cao, Chao Zhang, Zipeng Wu, Markus Grassl, and Bei Zeng. Quantum variational learning for quantum error-correcting codes. *Quantum*, 6:828, 2022.

[20] Marco Cerezo, Andrew Arrasmith, Ryan Babbush, Simon C Benjamin, Suguru Endo, Keisuke Fujii, Jarrod R McClean, Kosuke Mitarai, Xiao Yuan, Lukasz Cincio, et al. Variational quantum algorithms. *Nature Rev. Phys.*, 3(9):625–644, 2021.

[21] Marco Cerezo, Martin Larocca, Diego García-Martín, Nelson L Diaz, Paolo Braccia, Enrico Fontana, Manuel S Rudolph, Pablo Bermejo, Aroosa Ijaz, Supanut Thanasilp, et al. Does provable absence of barren plateaus imply classical simulability? *arXiv:2312.09121*, 2023.

[22] Marco Cerezo, Akira Sone, Tyler Volkoff, Lukasz Cincio, and Patrick J Coles. Cost function dependent barren plateaus in shallow parametrized quantum circuits. *Nature Commun.*, 12(1):1791, 2021.

[23] Christopher Chamberland and Michael E Beverland. Flag fault-tolerant error correction with arbitrary distance codes. *Quantum*, 2:53, 2018.

[24] Hongxiang Chen, Michael Vasmer, Nikolas P Breuckmann, and Edward Grant. Automated discovery of logical gates for quantum error correction. *Quantum Inf. Comput.*, 22(11-12):947–964, 2022.

[25] Ranyiliu Chen, Zhixin Song, Xuanqiang Zhao, and Xin Wang. Variational quantum algorithms for trace distance and fidelity estimation. *Quantum Sci. Technol.*, 7(1):015019, 2021.

[26] Yihua Chengyu, Richard Meister, Conor Carty, Sheng-Ku Lin, and Roberto Bondesan. Bayesian optimization for quantum error-correcting code discovery. *arXiv:2601.18562*, 2026.

[27] Iris Cong, Soonwon Choi, and Mikhail D Lukin. Quantum convolutional neural networks. *Nat. Phys.*, 15(12):1273–1278, 2019.

[28] Imre Csiszár and János Körner. *Information theory: coding theorems for discrete memoryless systems*. Cambridge University Press, 2011.

[29] Andrew J Daley, Immanuel Bloch, Christian Kokail, Stuart Flannigan, Natalie Pearson, Matthias Troyer, and Peter Zoller. Practical quantum advantage in quantum simulation. *Nature*, 607(7920):667–676, 2022.

[30] Christoph Dankert, Richard Cleve, Joseph Emerson, and Etera Livine. Exact and approximate unitary 2-designs and their application to fidelity estimation. *Phys. Rev. A*, 80(1):012304, 2009.

[31] Matthew DeCross, Reza Haghshenas, Minzhao Liu, Enrico Rinaldi, Johnnie Gray, Yuri Alexeev, Charles H Baldwin, John P Bartolotta, Matthew Bohn, Eli Chertkov, et al. The computational power of random quantum circuits in arbitrary geometries. *arXiv:2406.02501*, 2024.

[32] Abhinav Deshpande, Marcel Hinsche, Sona Najafi, Kunal Sharma, Ryan Sweke, and Christa Zoufal. Dynamic parameterized quantum circuits: expressive and barren-plateau free. *arXiv:2411.05760*, 2024.

[33] Michael Doherty, Matteo Puviani, Jasmine Brewer, Gabriel Matos, David Amaro, Ben Criger, and David T

Stephen. Fast stabilizer state preparation via ai-optimized graph decimation. *arXiv:2603.17743*, 2026.
[34] Thomas Fösel, Petru Tighineanu, Talitha Weiss, and Florian Marquardt. Reinforcement learning with neural networks for quantum feedback. *Phys. Rev. X*, 8(3):031084, 2018.
[35] Austin G Fowler, Matteo Mariantoni, John M Martinis, and Andrew N Cleland. Surface codes: Towards practical large-scale quantum computation. *Phys. Rev. A*, 86(3):032324, 2012.
[36] Christopher A Fuchs and Jeroen Van De Graaf. Cryptographic distinguishability measures for quantum-mechanical states. *IEEE Trans. Inf. Theory*, 45(4):1216–1227, 1999.
[37] Iulia M Georgescu, Sahel Ashhab, and Franco Nori. Quantum simulation. *Rev. Mod. Phys.*, 86(1):153–185, 2014.
[38] Daniel Gottesman. *Stabilizer codes and quantum error correction*. PhD thesis, California Institute of Technology, 1997.
[39] Daniel Gottesman. An introduction to quantum error correction. In *Proc. Sym. Appl. Math.*, volume 58, pages 221–236, 2002.
[40] Harper R Grimsley, Sophia E Economou, Edwin Barnes, and Nicholas J Mayhall. An adaptive variational algorithm for exact molecular simulations on a quantum computer. *Nature Commun.*, 10(1):3007, 2019.
[41] Rubén Darío Guerrero. Game-theoretic discovery of quantum error-correcting codes through nash equilibria. *arXiv:2510.15223*, 2025.
[42] Laszlo Gyongyosi and Sandor Imre. Properties of the quantum channel. *arXiv:1208.1270*, 2012.
[43] Trevor Hastie. *The elements of statistical learning: data mining, inference, and prediction*. Springer, 2009.
[44] Austin Yubo He and Zi-Wen Liu. Discovering highly efficient low-weight quantum error-correcting codes with reinforcement learning. *arXiv:2502.14372*, 2025.
[45] Sascha Heußen, David F Locher, and Markus Müller. Measurement-free fault-tolerant quantum error correction in near-term devices. *PRX Quantum*, 5(1):010333, 2024.
[46] Fumio Hiai and Dénes Petz. The proper formula for relative entropy and its asymptotics in quantum probability. *Comm. Math. Phys.*, 143:99–114, 1991.
[47] Dominic Horsman, Austin G Fowler, Simon Devitt, and Rodney Van Meter. Surface code quantum computing by lattice surgery. *New J. Phys.*, 14(12):123011, 2012.
[48] Violeta N Ivanova-Rohling, Niklas Rohling, and Guido Burkard. Discovery of an exchange-only gate sequence for cnot with record-low gate time using reinforcement learning. *arXiv:2402.10559*, 2024.
[49] Ali Javadi-Abhari, Matthew Treinish, Kevin Krsulich, Christopher J Wood, Jake Lishman, Julien Gacon, Simon Martiel, Paul D Nation, Lev S Bishop, Andrew W Cross, et al. Quantum computing with Qiskit. *arXiv:2405.08810*, 2024.
[50] Peter D Johnson, Jonathan Romero, Jonathan Olson, Yudong Cao, and Alán Aspuru-Guzik. Qvector: an algorithm for device-tailored quantum error correction. *arXiv:1711.02249*, 2017.
[51] Richard Jozsa. Fidelity for mixed quantum states. *J. Mod. Opt.*, 41(12):2315–2323, 1994.
[52] Naoki Kanazawa, Daniel J Egger, Yael Ben-Haim, Helena Zhang, William E Shanks, Gadi Aleksandrowicz, and Christopher J Wood. Qiskit experiments: A python package to characterize and calibrate quantum computers. *J. Open Source Softw.*, 8(84):5329, 2023.
[53] Amara Katabarwa, Katerina Gratsea, Athena Caesura, and Peter D Johnson. Early fault-tolerant quantum computing. *PRX Quantum*, 5(2):020101, 2024.
[54] Emanuel Knill and Raymond Laflamme. Concatenated quantum codes. *arXiv:quant-ph/9608012*, 1996.
[55] Emanuel Knill and Raymond Laflamme. Theory of quantum error-correcting codes. *Phys. Rev. A*, 55(2):900, 1997.
[56] Karl Kraus. General state changes in quantum theory. *Ann. Phys.*, 64(2):311–335, 1971.
[57] Raymond Laflamme, Cesar Miquel, Juan Pablo Paz, and Wojciech Hubert Zurek. Perfect quantum error correcting code. *Phys. Rev. Lett.*, 77(1):198, 1996.
[58] José Lebreuilly, Kyungjoo Noh, Chiao-Hsuan Wang, Steven M Girvin, and Liang Jiang. Autonomous quantum error correction and quantum computation. *arXiv:2103.05007*, 2021.
[59] Debbie W Leung, Michael A Nielsen, Isaac L Chuang, and Yoshihisa Yamamoto. Approximate quantum error correction can lead to better codes. *Phys. Rev. A*, 56(4):2567, 1997.
[60] Paul Pu Liang, Amir Zadeh, and Louis-Philippe Morency. Foundations and trends in multimodal machine learning: Principles, challenges, and open questions. *ACM Comput. Surv.*, 56(10):1–42, 2024.
[61] Chen Lin, Rucong Xu, and Yun Li. Design of efficient fault-tolerant quantum-computing circuits using a noise-adaptive dissipative quantum neural network. *Eng. Appl. Artif. Intell.*, 153:110808, 2025.
[62] Göran Lindblad. Completely positive maps and entropy inequalities. *Comm. Math. Phys.*, 40:147–151, 1975.
[63] Dong C Liu and Jorge Nocedal. On the limited memory bfgs method for large scale optimization. *Math. Program.*, 45(1):503–528, 1989.
[64] Shuwei Liu, Shiyu Zhou, Zi-Wen Liu, and Jinmin Yi. Noise-strength-adapted approximate quantum codes inspired by machine learning. *arXiv:2503.11783*, 2025.
[65] David F Locher, Lorenzo Cardarelli, and Markus Müller. Quantum error correction with quantum autoencoders. *Quantum*, 7:942, 2023.
[66] Caroline Mauron, Terry Farrelly, and Thomas M Stace. Optimization of tensor network codes with reinforcement learning. *New J. Phys.*, 26(2):023024, 2024.
[67] Jarrod R McClean, Sergio Boixo, Vadim N Smelyanskiy, Ryan Babbush, and Hartmut Neven. Barren plateaus in quantum neural network training landscapes. *Nat. Commun.*, 9(1):4812, 2018.
[68] David C McKay, Ian Hincks, Emily J Pritchett, Malcolm Carroll, Luke CG Govia, and Seth T Merkel. Benchmarking quantum processor performance at scale. *arXiv:2311.05933*, 2023.
[69] Nico Meyer, Jakob Murauer, Alexander Popov, Christian Ufrecht, Axel Plinge, Christopher Mutschler, and Daniel D Scherer. Warm-start variational quantum policy iteration. In *IEEE International Conference on Quantum Computing and Engineering (QCE)*, volume 1, pages 1458–1466, 2024.
[70] Nico Meyer, Christopher Mutschler, Andreas Maier, and Daniel D Scherer. Variational Quantum Error Correction. In *IEEE International Conference on Quantum Computing and Engineering (QCE)*, volume 2, pages 456–457, 2025.
[71] Nico Meyer, Christian Ufrecht, Maniraman Periyasamy, Axel Plinge, Christopher Mutschler, Daniel D Scherer, and Andreas Maier. Qiskit-torch-module: Fast prototyping of quantum neural networks. In *IEEE International Conference on Quantum Computing and Engineering (QCE)*, volume 1, pages 817–823, 2024.

[72] Nico Meyer, Christian Ufrecht, Maniraman Periyasamy, Daniel D Scherer, Axel Plinge, and Christopher Mutschler. A survey on quantum reinforcement learning. *arXiv:2211.03464*, 2022.
[73] Nico Meyer, Christian Ufrecht, George Yammine, Georgios Kontes, Christopher Mutschler, and Daniel D Scherer. Benchmarking quantum reinforcement learning. *arXiv:2501.15893*, 2025.
[74] Francesco Mezzadri. How to generate random matrices from the classical compact groups. *Not. Am. Math. Soc.*, 54(5):592–604, 2006.
[75] Hendrik Poulsen Nautrup, Nicolas Delfosse, Vedran Dunjko, Hans J Briegel, and Nicolai Friis. Optimizing quantum error correction codes with reinforcement learning. *Quantum*, 3:215, 2019.
[76] Michael A Nielsen and Isaac L Chuang. *Quantum Computation and Quantum Information*. Cambridge University Press, 2010.
[77] Jan Olle, Remmy Zen, Matteo Puviani, and Florian Marquardt. Simultaneous discovery of quantum error correction codes and encoders with a noise-aware reinforcement learning agent. *npj Quantum Inf.*, 10(126):1–17, 2024.
[78] Jan Ollé Aguilera, Oleg M Yevtushenko, and Florian Marquardt. Scaling the automated discovery of quantum circuits via reinforcement learning with gadgets. *arXiv:2503.11638*, 2025.
[79] Chae-Yeun Park and Nathan Killoran. Hamiltonian variational ansatz without barren plateaus. *Quantum*, 8:1239, 2024.
[80] Mincheol Park, Nishad Maskara, Marcin Kalinowski, and Mikhail D Lukin. Enhancing quantum memory lifetime with measurement-free local error correction and reinforcement learning. *Phys. Rev. A*, 111(1):012419, 2025.
[81] Adam Paszke, Sam Gross, Francisco Massa, Adam Lerer, James Bradbury, Gregory Chanan, Trevor Killeen, Zeming Lin, Natalia Gimelshein, Luca Antiga, Alban Desmaison, Andreas Kopf, Edward Yang, Zachary DeVito, Martin Raison, Alykhan Tejani, Sasank Chilamkurthy, Benoit Steiner, Lu Fang, Junjie Bai, and Soumith Chintala. Pytorch: An imperative style, high-performance deep learning library. In *Advances in Neural Information Processing Systems (NeurIPS)*, pages 8024–8035. Curran Associates, Inc., 2019.
[82] Dénes Petz. Sufficient subalgebras and the relative entropy of states of a von neumann algebra. *Commun. Math. Phys.*, 105:123–131, 1986.
[83] Alexander PM Place, Lila VH Rodgers, Pranav Mundada, Basil M Smitham, Mattias Fitzpatrick, Zhaoqi Leng, Anjali Premkumar, Jacob Bryon, Andrei Vrajitoarea, Sara Sussman, et al. New material platform for superconducting transmon qubits with coherence times exceeding 0.3 milliseconds. *Nature Commun.*, 12(1):1779, 2021.
[84] Leonid P Pryadko, Vadim A Shabashov, and Valerii K Kozin. Qdistrnd: A gap package for computing the distance of quantum error-correcting codes. *J. Open Source Softw.*, 7(71):4120, 2022.
[85] IBM Quantum, 2025.
[86] Lakshika Rathi, Stephen DiAdamo, and Alireza Shabani. Quantum autoencoders for learning quantum channel codes. In *16th International Conference on COMmunication Systems & NETworkS (COMSNETS)*, pages 988–993, 2024.
[87] IQM Resonance, 2025.
[88] Aidan Roy and AJ Scott. Weighted complex projective 2-designs from bases: optimal state determination by orthogonal measurements. *J. Math. Phys.*, 48(7), 2007.
[89] Benjamin IP Rubinstein. Evolving quantum circuits using genetic programming. In *IEEE Congress on Evolutionary Computation (CEC)*, volume 1, pages 144–151. IEEE, 2001.
[90] Benjamin Schumacher and Michael D Westmoreland. Approximate quantum error correction. *Quantum Inf. Process.*, 1:5–12, 2002.
[91] Manav Seksaria and Anil Prabhakar. Correcting quantum errors one gradient step at a time. *arXiv:2512.18061*, 2025.
[92] Peter W Shor. Scheme for reducing decoherence in quantum computer memory. *Phys. Rev. A*, 52(4):R2493, 1995.
[93] Peter W Shor. Fault-tolerant quantum computation. In *Proceedings of 37th Conference on Foundations of Computer Science (FOCS)*, pages 56–65, 1996.
[94] Peter W Shor. Polynomial-time algorithms for prime factorization and discrete logarithms on a quantum computer. *SIAM Rev.*, 41(2):303–332, 1999.
[95] Paul Skrzypczyk and Daniel Cavalcanti. *Semidefinite programming in quantum information science*. IOP Publishing, 2023.
[96] Hans-Jürgen Sommers and Karol Życzkowski. Statistical properties of random density matrices. *J. Phys. A*, 37(35):8457, 2004.
[97] Andrew M Steane. Error correcting codes in quantum theory. *Phys. Rev. Lett.*, 77(5):793, 1996.
[98] Vincent Paul Su, ChunJun Cao, Hong-Ye Hu, Yariv Yanay, Charles Tahan, and Brian Swingle. Discovery of optimal quantum error correcting codes via reinforcement learning. *Phys. Rev. Appl.*, 23:034048, 2025.
[99] Daniel Tandeitnik and Thiago Guerreiro. Evolving quantum circuits. *Quantum Inf. Process.*, 23(3):109, 2024.
[100] Barbara M Terhal. Quantum error correction for quantum memories. *Rev. Mod. Phys.*, 87(2):307–346, 2015.
[101] Giacomo Torlai and Roger G Melko. Neural decoder for topological codes. *Phys. Rev. Lett.*, 119(3):030501, 2017.
[102] David K Tuckett, Stephen D Bartlett, and Steven T Flammia. Ultrahigh error threshold for surface codes with biased noise. *Phys. Rev. Lett.*, 120(5):050505, 2018.
[103] Armin Uhlmann. Relative entropy and the wigner-yanase-dyson-lieb concavity in an interpolation theory. *Comm. Math. Phys.*, 54:21–32, 1977.
[104] William G Unruh. Maintaining coherence in quantum computers. *Phys. Rev. A*, 51(2):992, 1995.
[105] Lev Vaidman, Lior Goldenberg, and Stephen Wiesner. Error prevention scheme with four particles. *Phys. Rev. A*, 54(3):R1745, 1996.
[106] Vlatko Vedral. The role of relative entropy in quantum information theory. *Rev. Mod. Phys.*, 74(1):197, 2002.
[107] Peiyong Wang, Muhammad Usman, Udaya Parampalli, Lloyd CL Hollenberg, and Casey R Myers. Automated quantum circuit design with nested monte carlo tree search. *IEEE Trans. Quantum Eng.*, 4(3100620):1–20, 2023.
[108] Zhaoyou Wang, Taha Rajabzadeh, Nathan Lee, and Amir H Safavi-Naeini. Automated discovery of autonomous quantum error correction schemes. *PRX Quantum*, 3(2):020302, 2022.

[109] Zihao Wang and Hao Tang. Artificial intelligence for quantum error correction: A comprehensive review. *arXiv:2412.20380*, 2024.
[110] Mark A Webster and Dan E Browne. Engineering quantum error correction codes using evolutionary algorithms. *IEEE Trans. Quantum Eng.*, 5(3100514):1–14, 2025.
[111] Xiaosi Xu, Simon C Benjamin, and Xiao Yuan. Variational circuit compiler for quantum error correction. *Phys. Rev. Appl.*, 15(3):034068, 2021.
[112] Yariv Yanay. Learning better error correction codes with hybrid quantum-assisted machine learning. *arXiv:2601.08014*, 2026.
[113] Yue Yin, Tailong Xiao, Xiaoyang Deng, Ming He, Jianping Fan, and Guihua Zeng. Discovering autonomous quantum error correction via deep reinforcement learning. *arXiv:2511.12482*, 2025.
[114] Remmy Zen, Jan Olle, Luis Colmenarez, Matteo Puviani, Markus Müller, and Florian Marquardt. Quantum circuit discovery for fault-tolerant logical state preparation with reinforcement learning. *arXiv:2402.17761*, 2024.
[115] Yexiong Zeng, Wei Qin, Ye-Hong Chen, Clemens Gneiting, and Franco Nori. Neural-network-based design of approximate gottesman-kitaev-preskill code. *Phys. Rev. Lett.*, 134(6):060601, 2025.
[116] Yexiong Zeng, Zheng-Yang Zhou, Enrico Rinaldi, Clemens Gneiting, and Franco Nori. Approximate autonomous quantum error correction with reinforcement learning. *Phys. Rev. Lett.*, 131(5):050601, 2023.
[117] Shi-Xin Zhang, Chang-Yu Hsieh, Shengyu Zhang, and Hong Yao. Differentiable quantum architecture search. *Quantum Sci. Technol.*, 7(4):045023, 2022.
[118] Fabio Zoratti, Giacomo De Palma, Bobak Kiani, Quynh T Nguyen, Milad Marvian, Seth Lloyd, and Vittorio Giovannetti. Improving the speed of variational quantum algorithms for quantum error correction. *Phys. Rev. A*, 108(2):022611, 2023.
[119] Karol Życzkowski and Hans-Jürgen Sommers. Average fidelity between random quantum states. *Phys. Rev. A*, 71(3):032313, 2005.